MAGNETICS AND CONTROL IN POWER ELECTRONICS:

I: Modeling of Coupled Inductors

II: One-Cycle Control of Switching Converters

Thesis by

Enrico Santi

In Partial Fulfillment of the Requirements

for the Degree of

Doctor of Philosophy

California Institute of Technology

Pasadena, California

1994

(Submitted September 9, 1993)

ai miei genitori

Acknowledgements

I wish to thank my advisor, Professor S. Ćuk, for the freedom to choose and develop independently research topics and for his steady encouragement, and my co-advisor, Professor R. D. Middlebrook, for his support and guidance.

I gratefully acknowledge the financial support of Apple Computer Inc., Day-Ray Products, General Dynamics, GEC Ferranti Defense Systems Ltd., General Electric Co., Italtel, MagneTek, Rockwell International Inc., and Southern California Edison. The finite element program GE2D was provided by General Electric.

Every graduate of the Power Electronics Group owes a debt to his predecessors, who have left behind a well-organized laboratory, useful computer programs, and helpful hints on many procedures necessary for completing papers and theses. I also wish to thank the members of the Power Electronics Group for helpful discussions, suggestions, and of course friendships.

Abstract

Part I:

For coupled-inductor and integrated-magnetics design it is of paramount importance to accurately model leakages. Air gap position has a dramatic effect on coupled-inductor characteristics. Improved reluctance models that capture this effect are proposed.

For the most common coupled-inductor structures, i.e., UU and UI cores with windings on different legs, a simple model valid for *any* gap arrangement is proposed. The model has a single leakage reluctance that is constant for a given core geometry and can be determined from a single set of measurements.

A method to *estimate* this reluctance from core geometry is also suggested.

A new coupled-inductor structure that achieves quasi-zero current ripple without need for turns ratio adjustment is introduced.

Closed-form design equations for coupled-inductors are given.

Part 2:

The concept of One-Cycle control has recently been proposed. The generality of this control technique is demonstrated through description of its implementation for different DC-DC switching converters. It is a nonlinear control technique with significant advantages in terms of rejection of line perturbation, speed of response and insensitivity to circuit parameters. Until now, no stability analysis was available and, under certain conditions, instability was observed. In this paper a stability analysis of a One-Cycle controlled Ćuk converter (a fourth order system) is performed, which shows that stability depends on the value of parasitic elements. A modification of the control to eliminate steady-state output voltage error is proposed. Finally, a modification of the control that ensures stability independently of the value of parasitic elements is suggested. All

theoretical results are experimentally verified.

Contents

Part I

Modeling of Coupled Inductors

Chapter 1

Introduction

Electrical power conversion is the process of transforming electrical power from a given input form to a desired output form. The power source provides a certain voltage or current waveform that the power converter transforms into a different voltage or current waveform.

The main requirements on power converters are high efficiency (which ideally should be 100%), small weight and volume. In some sense, it could be said that power converters should be as "invisible" as possible, both electrically (high efficiency) and physically (small size and weight).

In order to achieve these goals, the preferred approach in recent years has been switched-mode power conversion, in which semiconductor devices are used as switches. A first advantage over conventional linear power converters is that semiconductor devices operate in an (ideally) lossless way. Another advantage is that these converters can operate at frequencies much higher than the 60 *Hz* line frequency, with dramatic reductions in reactive component sizes. Much smaller inductors, transformers and capacitors can be used.

Advances in power semiconductor technology have led to higher and higher switching frequencies in the quest for reduced size and weight. Eventually, magnetic components turn out to be the bottle-neck, and in modern switching converters they can constitute as much as 50% of the overall converter size and weight.

An approach to further reduce magnetic component size and weight is to further increase the switching frequency, but eventually a point of diminished returns is reached, because increased core losses at high frequency force the designer to reduce AC flux swing in the magnetic components.

Another approach to magnetic component size reduction is to magnetically couple

together inductors and transformers in what are called *coupled-inductor* and *integrated-magnetics* structures. The literature reports several applications of this approach to DC-DC converters [14], [15], [16] and to AC-DC rectifiers [8]. The size and weight reduction of coupled magnetic circuits is discussed in [5] pp. 27–29 and in [4].

Another advantage of coupled inductors is that if a certain *zero ripple condition* is met, current ripple in one of the inductors can be eliminated. As a result, ripple filtering requirements can be satisfied using smaller reactive components.

In order to meet this zero ripple condition, accurate models for the *leakage* in coupled-inductor structures are needed. The goal of this work is to improve understanding of coupled magnetic structures and leakages. The immediate objective is the analysis and the design of coupled-inductor structures, and for this purpose improved leakage models and methods to estimate leakages in these structures are presented, but the gained understanding proves useful in the analysis of interesting magnetic structures like the one presented in Appendix A.

In chapter 2, the different tools available for the analysis of magnetic circuits are reviewed.

In chapter 3, the zero ripple condition is derived in different ways, in an effort to improve understanding of the zero ripple phenomenon.

In chapter 4, it is shown that sensitivity of the zero ripple condition to errors in turns ratio, in leakage estimation and other factors is decreased by increasing the total leakage of the structure.

In chapter 5, it is shown that air gap position has a dramatic effect on coupling and on effective inductances of the coupled-inductor structure. Reluctance models used in the past were unable to model this behavior. A new reluctance model that captures this effect is proposed. This model is very simple and it has a single leakage reluctance, constant for a given core geometry. The success of the new model is attributed to the fact that it is a *physical model* and it faithfully represents physical leakage fluxes in the magnetic structure.

In chapter 6, a general procedure to find the *physical model* of a magnetic structure starting from core geometry is given and applied to various examples of two-winding

structures.

In chapter 7, the zero ripple condition is generalized to multiple-winding structures. In order to use these structures, reluctance models are needed. Therefore, the procedure to find physical reluctance model presented in the previous chapter is applied to various three-winding structures of practical interest.

In chapter 8, a new magnetic structure for coupled inductors is presented. This structure achieves quasi-zero current ripple without the need for turns ratio adjustement, is easier to design and gives a one order of magnitude reduction of radiated noise. Reduction of radiated noise is an important issue in switching converter applications due to the sensitivity to noise exhibited by electronic equipment.

In chapter 9, design procedures for coupled inductors are presented for various gap arrangements of practical interest.

In chapter 10, a method to estimate the leakage of a given coupled inductor structure from its core geometry is presented. Derivations of the approximate formulas used are given in Appendix C.

In Appendix A, an interesting problem in magnetic circuits is presented. It is felt that this problem has a good educational value and puts to a test one's understanding of magnetic circuits and transformers.

Chapter 2

Models for Magnetic Circuits

In order to understand coupled-inductor and integrated-magnetics circuits, it is necessary to have a thorough understanding of magnetic circuit models.

There are three different types of models for magnetic circuits:

1. Coupled inductor models
2. Circuit models
3. Reluctance models

None of these models is intrinsically better than the other ones. Depending on the application one model may be more convenient and easier to use. These models are equivalent and there are standard techniques to go from one model to the other.

In this chapter these three models are briefly reviewed.

2.1 Coupled Inductor Model

2.1.1 Single Coil

In a single coil with N turns (Fig. 2.1), current i generates a flux ϕ. The relationship between voltage and flux is given by Faraday's law

$$v = N\frac{d\phi}{dt} \tag{2.1}$$

Flux is proportional to the current that generates it, so that we can define the *inductance* as flux linkage per unit current

$$L \triangleq \frac{N\phi}{i} \tag{2.2}$$

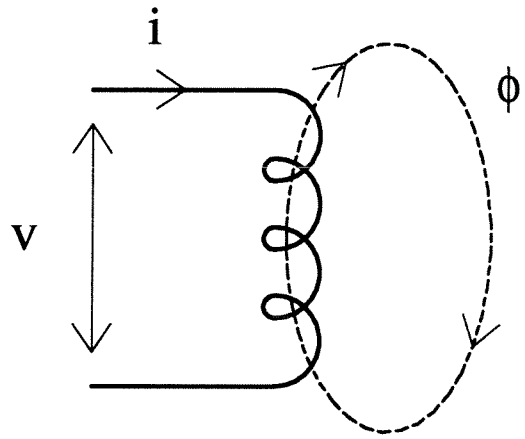

Figure 2.1: Single-coil inductor.

Equations (2.1) and (2.2) can be combined to give the usual circuit equation describing an inductor

$$v = L \frac{di}{dt}$$

2.1.2 Coupled Inductors: Current in One Coil Only

Let us consider now two coils, which will be called coil 1 (or primary coil) and coil 2 (or secondary coil). Their number of turns is N_1 and N_2 respectively. Different flux components can then be identified. Since the general case of currents on both coils is rather complicated, we start considering two special cases: current in the first coil only and current in the second coil only, as shown in Fig. 2.2a-b. In each case, two flux components can be identified: flux that couples with the other coil and flux that does not. We can write

Current i_1	*Current* i_2
$\phi_{11} = \phi_{l1} + \phi_{21}$	$\phi_{22} = \phi_{l2} + \phi_{12}$

The two indices have the following meaning: the first index indicates whether the flux links the other coil or not and the second index indicates which current generates the flux.

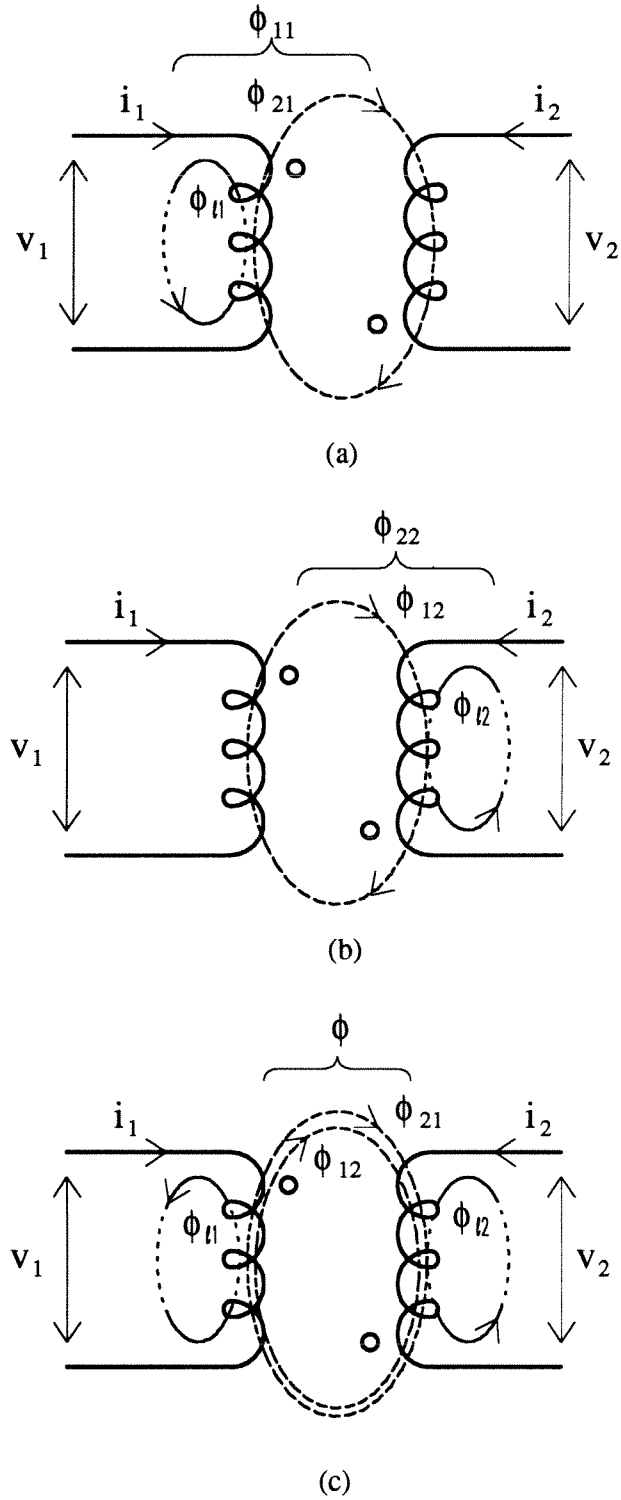

Figure 2.2: Two-coil coupled inductors. Current in coil 1 only (a), current in coil 2 only (b) and superposition of two previous cases (c).

2.1.3 Primary and Secondary Coupling Coefficients k_1 and k_2

We can define coupling coefficients k_1 and k_2 as

Primary only excited	*Secondary only excited*
$k_1 \triangleq \frac{\phi_{21}}{\phi_{11}}$	$k_2 \triangleq \frac{\phi_{12}}{\phi_{22}}$

(2.3)

Coupling coefficient k_1, for example, is the ratio of mutual flux to total flux *when only coil 1 is driven.* Therefore, these coefficients are a measure of coupling between the two coils and are always smaller than unity.

2.1.4 Coupled Inductors: Current in Both Coils

The general case of current in both coils can be studied by superposition of the two cases of Fig. 2.2a-b and it is shown in Fig. 2.2c. Flux ϕ represents flux that couples with both windings and it is the sum of fluxes ϕ_{12} and ϕ_{21}. Total flux linking primary coil is called ϕ_1 and total flux linking secondary coil is called ϕ_2. Using superposition we can write

$$\begin{aligned} \phi_1 &= \phi_{l1} + \overbrace{\phi}^{} \\ &= \phi_{l1} + \underbrace{\phi_{21}}_{} + \phi_{12} \\ &= \underbrace{\phi_{11}}_{} + \phi_{12} \end{aligned} \qquad \begin{aligned} \phi_2 &= \phi_{l2} + \overbrace{\phi}^{} \\ &= \phi_{l2} + \phi_{12} + \underbrace{\phi_{21}}_{} \\ &= \underbrace{\phi_{22}}_{} + \phi_{21} \end{aligned} \tag{2.4}$$

2.1.5 Definition of Inductances

The following inductances can be defined

Primary only excited		*Secondary only excited*
$L_{l1} \triangleq \frac{N_1\phi_{l1}}{i_1}$		$L_{l2} \triangleq \frac{N_2\phi_{l2}}{i_2}$
$L_{11} \triangleq \frac{N_1\phi_{11}}{i_1}$		$L_{22} \triangleq \frac{N_2\phi_{22}}{i_2}$
$\frac{N_2\phi_{21}}{i_1}$	$\triangleq M \triangleq$	$\frac{N_1\phi_{12}}{i_2}$

(2.5)

The last equality is due to reciprocity. L_{l1} and L_{l2} are the *leakage inductances* of the two coils, L_{11} and L_{22} are the *self-inductances* and M is the *mutual inductance*.

2.1.6 Coupling Coefficients in Terms of Inductances

Coupling coefficients (2.3) can be rewritten using (2.5) as

$$k_1 = \frac{N_1}{N_2}\frac{M}{L_{11}} \qquad\qquad k_2 = \frac{N_2}{N_1}\frac{M}{L_{22}}$$

The usual "coupling coefficient" is defined as as

$$k \triangleq \sqrt{\frac{M^2}{L_{11}L_{22}}}$$

There is an interesting relationship between k_1, k_2 and k. From the equations above it is

$$k_1 k_2 = \frac{N_1}{N_2}\frac{M}{L_{11}}\frac{N_2}{N_1}\frac{M}{L_{22}} = \frac{M^2}{L_{11}L_{22}} = k^2$$

2.1.7 Coupled-Inductor Equations

From Faraday's law (2.1) terminal voltages of the two coils are

$$\begin{aligned} v_1 &= N_1 \overset{\circ}{\phi}_1 \\ &= N_1\left(\overset{\circ}{\phi}_{11} + \overset{\circ}{\phi}_{12}\right) \\ &= L_{11}\overset{\circ}{i}_1 + M\overset{\circ}{i}_2 \end{aligned} \qquad\qquad \begin{aligned} v_2 &= N_2 \overset{\circ}{\phi}_2 \\ &= N_2\left(\overset{\circ}{\phi}_{22} + \overset{\circ}{\phi}_{21}\right) \\ &= L_{22}\overset{\circ}{i}_2 + M\overset{\circ}{i}_1 \end{aligned} \tag{2.6}$$

These are the usual coupled-inductor equations.

2.1.8 Coupled-Inductor Equations for Multiple-Winding Structures

The generalization of coupled-inductor equations to circuits with n windings is

$$\begin{bmatrix} v_1 \\ v_2 \\ \vdots \\ v_n \end{bmatrix} = \begin{bmatrix} L_{11} & M_{12} & \cdots & M_{1n} \\ M_{12} & L_{22} & \cdots & M_{2n} \\ \vdots & \vdots & \ddots & \vdots \\ M_{1n} & M_{2n} & \cdots & L_{nn} \end{bmatrix} \begin{bmatrix} \overset{\circ}{i}_1 \\ \overset{\circ}{i}_2 \\ \vdots \\ \overset{\circ}{i}_n \end{bmatrix} \tag{2.7}$$

Notice that the inductance matrix is symmetric due to reciprocity.

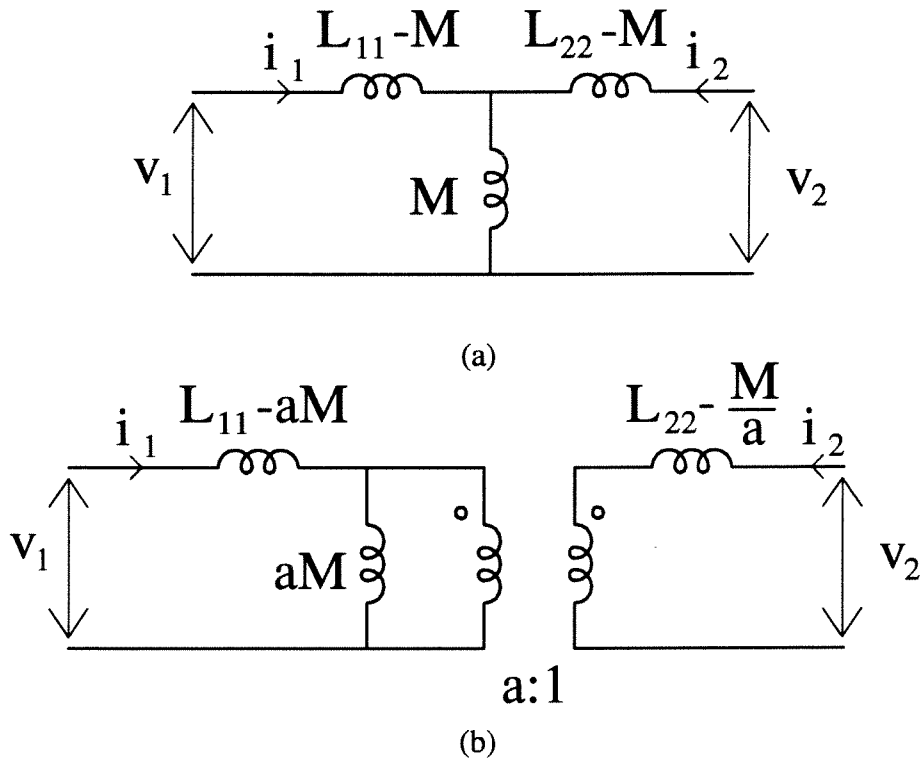

Figure 2.3: Equivalent circuit that satisfies coupled-inductor equations (a). Insertion of ideal transformer (b).

2.1.9 Circuit Equivalents of Coupled-Inductor Equations and Insertion of an Arbitrary Ideal Transformer

It can be easily verified that coupled-inductor equations (2.6) are satisfied by the circuit of Fig. 2.3a, which therefore represents an equivalent circuit for the coupled inductors.

It is possible to insert in the equivalent circuit an ideal transformer with an arbitrary ratio a as shown in Fig. 2.3b. It can be easily verified that the coupled-inductor equations are still satisfied.

2.1.10 Circuit Model: Ideal Transformer Ratio Equal to the Turns Ratio

The case $a = N_1/N_2$, i.e., transformer ratio equal to turns ratio, is particularly interesting because in this case inductances in the equivalent model assume a physical

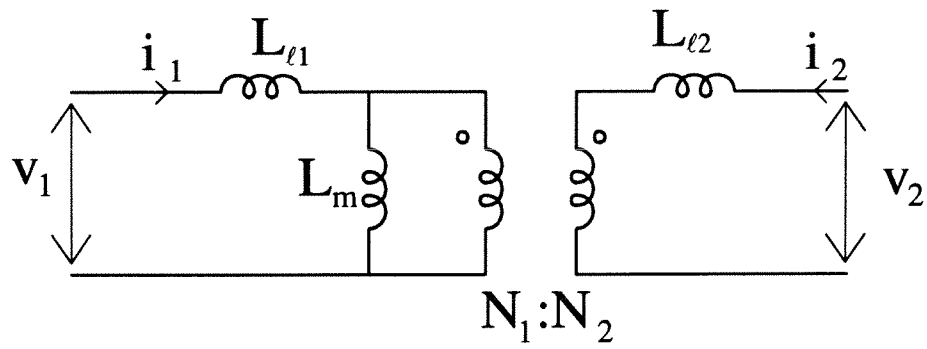

Figure 2.4: Circuit model for coupled inductors.

meaning with respect to the physical picture of Fig. 2.2. In fact from (2.5) and (2.4) it follows that

$$L_{l1} = \frac{N_1\phi_{l1}}{i_1} = L_{11} - \frac{N_1}{N_2}M \qquad\qquad L_{l2} = \frac{N_2\phi_{l2}}{i_2} = L_{22} - \frac{N_2}{N_1}M$$

$$L_m \triangleq \frac{N_1}{N_2}M$$

where L_m is the *magnetizing inductance*. The equivalent circuit of Fig. 2.3b becomes the circuit of Fig. 2.4. Notice that this is the usual circuit model of a transformer.

2.2 Reluctance Model

There is a striking similarity between static electric circuit equations and static magnetic circuit equations.

$$\oiint \overline{J} \cdot d\overline{S} = 0 \qquad \oiint \overline{B} \cdot d\overline{S} = 0 \tag{2.8}$$

$$emf = V = \oint_\ell \overline{E} \cdot d\overline{\ell} \qquad mmf = NI = \oint_\ell \overline{H} \cdot d\overline{\ell} \tag{2.9}$$

$$I = \iint_S \overline{J} \cdot d\overline{S} \qquad \phi = \iint_S \overline{B} \cdot d\overline{S} \tag{2.10}$$

$$\overline{J} = \sigma\overline{E} \qquad \overline{B} = \mu\overline{H} \tag{2.11}$$

Equation (2.8) represents Kirchhoff's current law and equation (2.9) represents Kirchhoff's voltage law. These equations are the basis of circuit analysis.

A simple electric circuit and the analog magnetic circuit are shown in Fig. 2.5a-b. These circuits have a uniform cross-section S and average length ℓ. For the magnetic

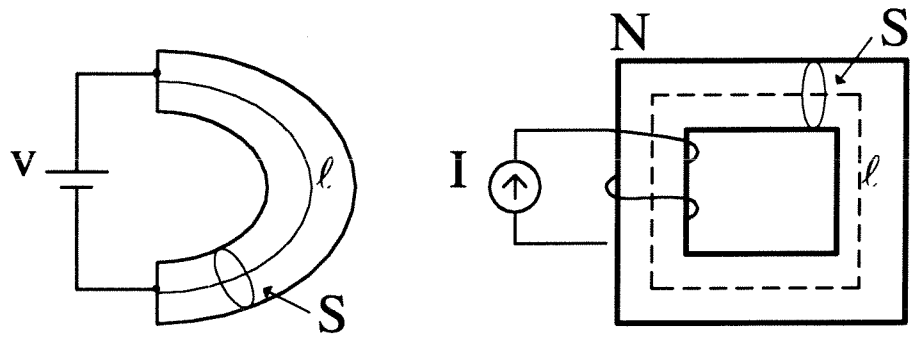

(a) (b)

Figure 2.5: An electric circuit (a) and its analog magnetic circuit (b).

circuit, from (2.9) it follows that

$$NI = H\ell \tag{2.12}$$

Equations (2.10) and (2.11) applied to a cross-section of the magnetic circuit give

$$\phi = BS = \mu HS \tag{2.13}$$

Substituting (2.13) into (2.12)

$$NI = \underbrace{\frac{\ell}{\mu S}}_{\mathcal{R}} \phi \tag{2.14}$$

The quantity $\mathcal{R}$ is the *reluctance* of the magnetic circuit. The reciprocal of this quantity is called *permeance* and is indicated by the symbol $\mathcal{P}$.

An analogous derivation based on the electric circuit leads to Ohm's law and to the definition of *resistance* R

$$V = \underbrace{\frac{\ell}{\sigma S}}_{R} I \tag{2.15}$$

The electric circuit model based on (2.15) and the analog magnetic circuit based on (2.14) are shown in Fig. 2.6a-b.

There are, however, two main differences between electric circuits and magnetic circuits that make the study of magnetic circuits more complicated:

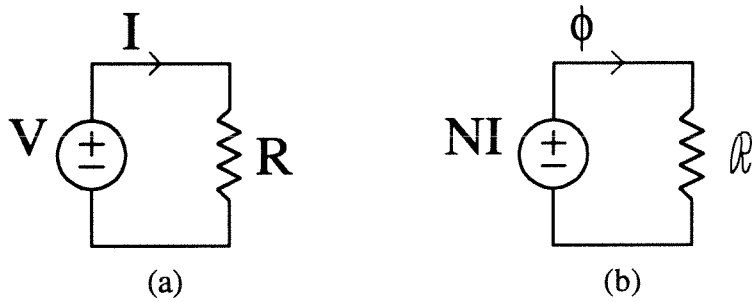

Figure 2.6: Electric circuit model (a) and magnetic circuit model (b).

- Ferromagnetic materials normally used in magnetic circuits like the one in Fig. 2.5b have a nonlinear and double-valued $B - H$ characteristic. This means that permeability μ is not constant for ferromagnetic materials. In particular, the $B - H$ characteristic exhibits *saturation*, i.e., after reaching a value B_{SAT}, flux density increases very little with excitation H.

- In electric circuits the conductivity σ of the conductors is usually more than 10^{15} times bigger than the conductivity of insulators, but the permeability μ of a magnetic circuit is only 100 to 10^4 times bigger than the permeability μ_0 of air. Therefore, leakage currents in an electric circuit can be almost always neglected, but leakage fluxes in a magnetic circuit usually need to be modelled.

2.2.1 Magnetic Saturation and the Introduction of Airgaps

The *B–H material characteristic* of a ferromagnetic material is shown in Fig. 2.7a. The slope represents (incremental) permeability μ. To study its effect on the magnetic circuit of Fig. 2.5, the *B–H* characteristic, neglecting losses, can be scaled to represent the *magnetic structure characteristic*. In Fig. 2.7b the x-axis is scaled by the length of the magnetic path ℓ so that it represents Ampere-turns (equation (2.12)) and the y-axis is scaled by core cross-section S so that it represents flux ϕ (equation (2.13)). The slope now represents permeance $\mathcal{P}$ of the magnetic structure. After flux density reaches the value B_{SAT}, the permeance value drops.

If a coil has a DC current that would make it operate in the saturation region, an air

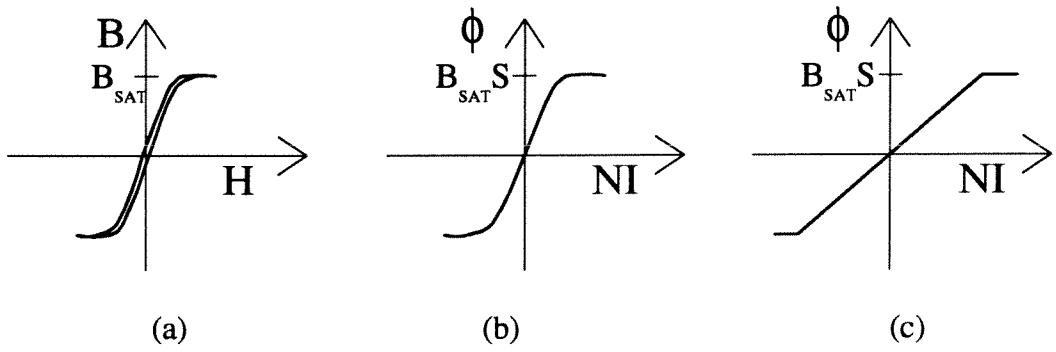

(a) (b) (c)

Figure 2.7: B-H loop for a ferromagnetic material (a) is scaled to represent core characteristic (b). Core characteristic with air gap (c).

gap can be introduced. The air gap reluctance appears in series with core reluctance in the model of Fig. 2.6b and its value is

$$\mathcal{R}_x = \frac{x}{\mu_0 S} \tag{2.16}$$

where x is gap thickness and $\mu_0 = 4\pi \cdot 10^{-7}\ H/m$ is the permeability of air. Since μ is 100 to 10^4 times bigger than μ_0, $\mathcal{R}_x$ usually dictates the total reluctance. The effect on the core characteristic is shown in Fig. 2.7c. Notice that the core reaches saturation for a higher magneto-motive force NI and that the core characteristic below saturation is linearized by the airgap.

2.3 Circuit Model

The circuit model for the generic coupled inductors of Fig. 2.2 was derived from the coupled-inductor equations in section 2.1. In general, circuit models can be derived from reluctance models. This approach is preferred because the circuit model so obtained is closely related to the physical structure of the coupled inductors. This issue will be discussed in chapter 6. The derivation of the circuit model from the reluctance model is illustrated through an example.

2.3.1 Derivation of Circuit Model from Reluctance Model

The magnetic structure studied here and its reluctance model are shown in Fig. 2.8. Reluctance $\mathcal{R}_x$ is given by (2.16). Leakage reluctances $\mathcal{R}_{l1}$ and $\mathcal{R}_{l2}$ represent leakage flux

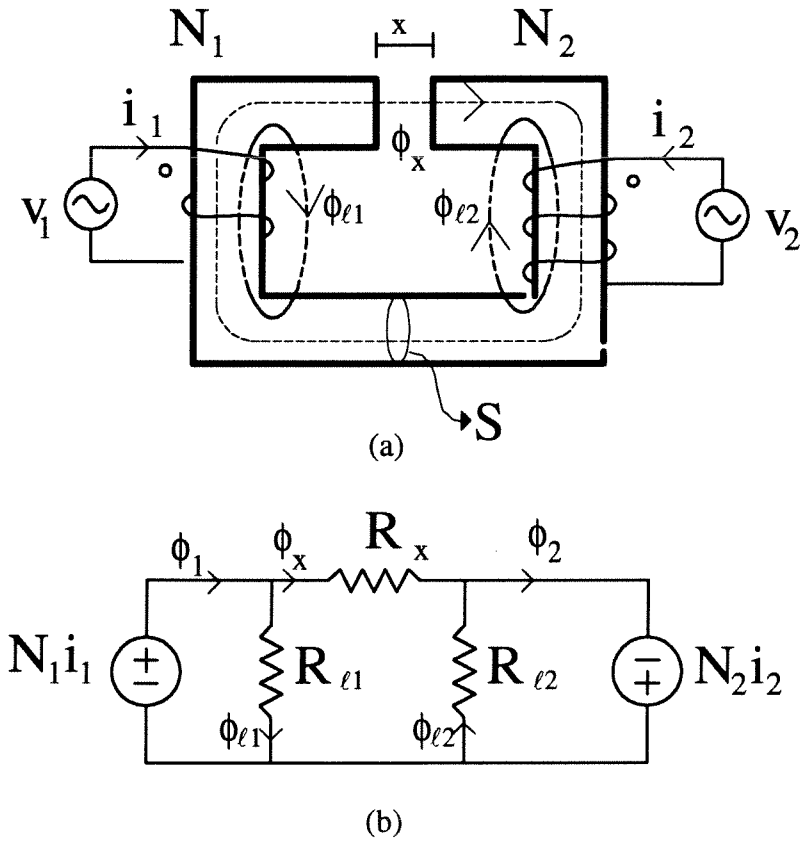

Figure 2.8: Example of magnetic structure (a) and its reluctance model (b).

paths in air. No simple formulas exist for these reluctances, and the only correct way to calculate them theoretically is to solve the three-dimensional magnetic field problem.

Duality Transformation

We want to go from the reluctance model to a circuit model. It can be observed that in the reluctance model *mmf* sources act as voltages and fluxes act as currents. This is in some sense the dual of a circuit model, because *mmf* sources are proportional to currents and fluxes are proportional to (the integral of) voltages. Therefore, the first step in the derivation of the circuit model is a duality transformation.

Duality

In circuit theory two networks are *dual* if the loop equations for one network are identical (with consistent change of notation) to the node equations for the other network. Therefore, if the solution for one of the networks is known, the solution for the other one can be immediately obtained if appropriate transcriptions are used.

Procedure to find the dual of a resistive network

The following procedure allows to obtain the dual of a given resistive network.

1. A dot is placed inside each loop of the network and a dot is placed outside the network. These dots will become nodes of the dual network.

2. The dual of each element is places across the original element, connecting the dots on both sides. In the case of resistive networks duals are

$$\textit{Resistor} \iff \textit{Conductor}$$

$$\textit{Voltage source} \iff \textit{Current source}$$

   The dual elements have the same numerical values of the original elements. For example, a 5 Ω resistor becomes a 5 Siemens conductor. Equivalently it may be said that the dual of a resistor is a resistor with a numerical value equal to the reciprocal of the original element (a 5 Ω resistor becomes a $1/5$ Ω resistor).

3. The direction of dual branches is obtained by rotating the direction of the original branch counter-clockwise until it coincides with the dual branch.

Application of the above procedure to our example is shown in Fig. 2.9. The resistances of the dual model have numerical values equal to the reciprocal of the reluctance values and therefore are represented by permeances.

Steps of Procedure from Reluctance Model to Circuit Model

1. Duality transformation. The first step is the duality transformation described above.

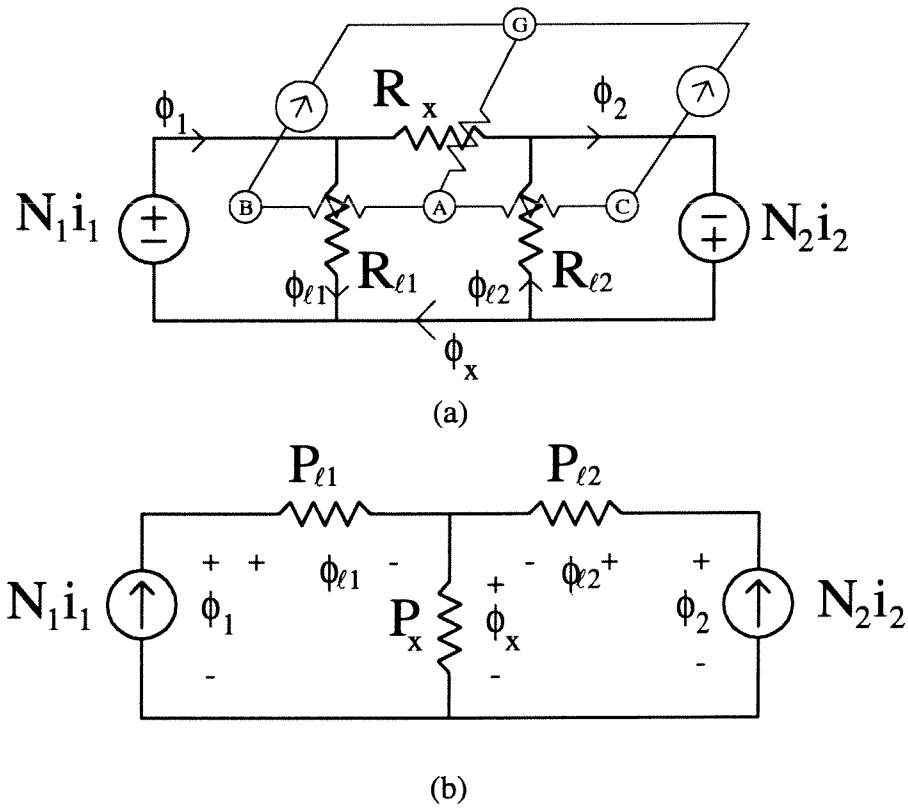

Figure 2.9: Application of duality to reluctance model (a) gives dual permeance model (b).

2. Current scaling. Current scaling is done with respect to the primary number of turns and the result is shown in Fig. 2.10a. Currents are divided by N_1 and resistances are multiplied by N_1, so that voltages are left unchanged.

3. Voltage scaling. In Fig. 2.10b voltages and resistances are scaled by N_1 so that currents are left unchanged. Notice that after this transformation voltages are numerically equal to flux linkages.

4. Inductance model. Realizing that $v = N\ d\phi/dt$ and $L = N^2\mathcal{P}$ the inductance model can be immediately derived as shown in Fig. 2.11a.

5. Ideal transformer. An ideal transformer can be inserted to match terminal voltages and currents to those in the original circuit as in Fig. 2.11b.

Note that in steps 2-3 the dual circuit could be scaled by any number. Fig. 2.12 shows the final inductance model if the dual model is scaled by N_2^2 or scaled by 1.

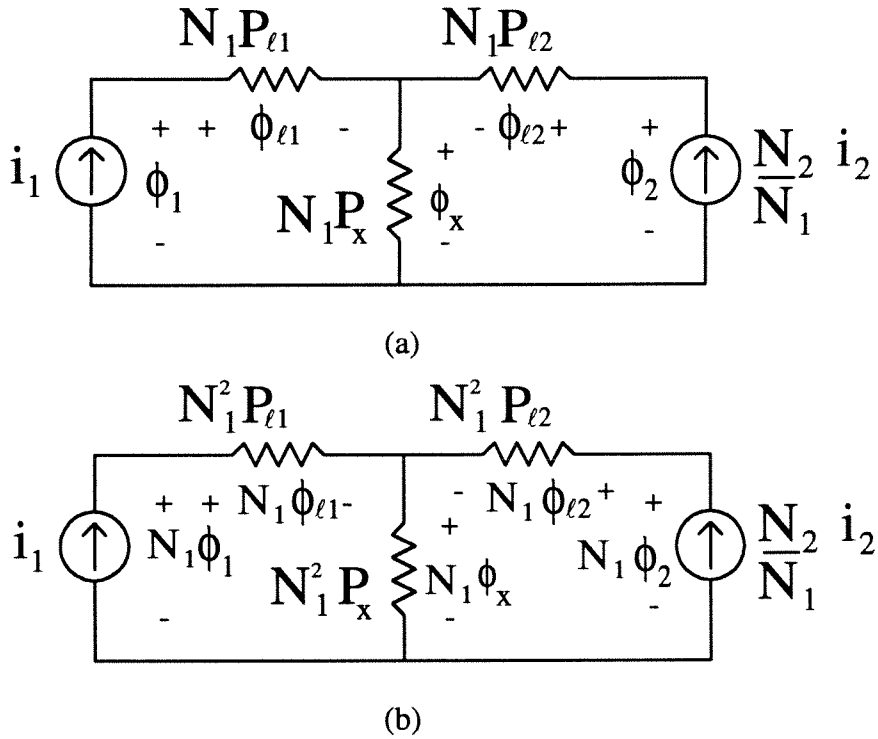

Figure 2.10: Current scaling (a) and voltage scaling (b) with respect to N_1.

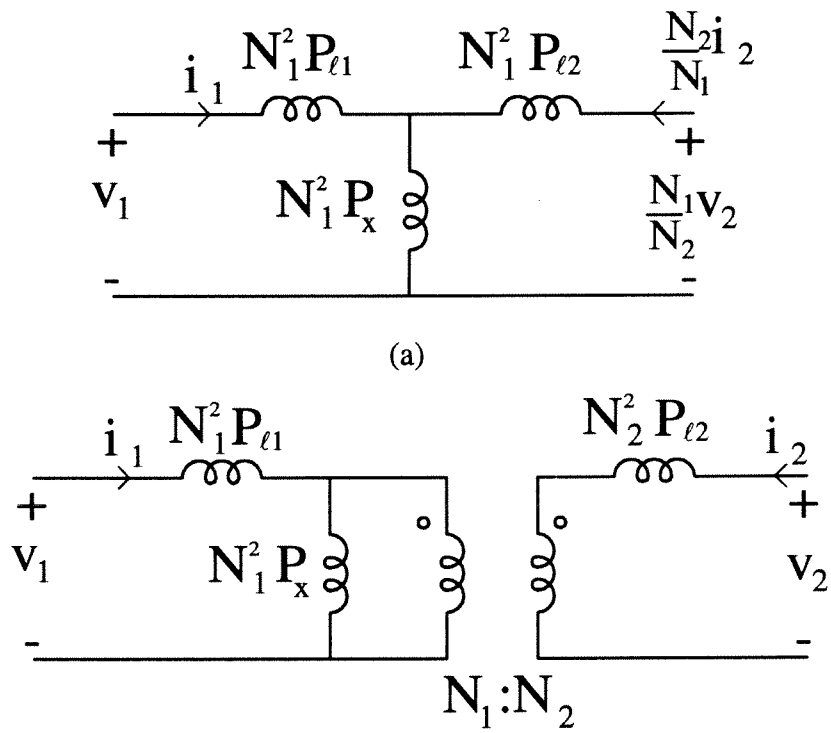

Figure 2.11: Inductance model (a) and insertion of ideal transformer (b).

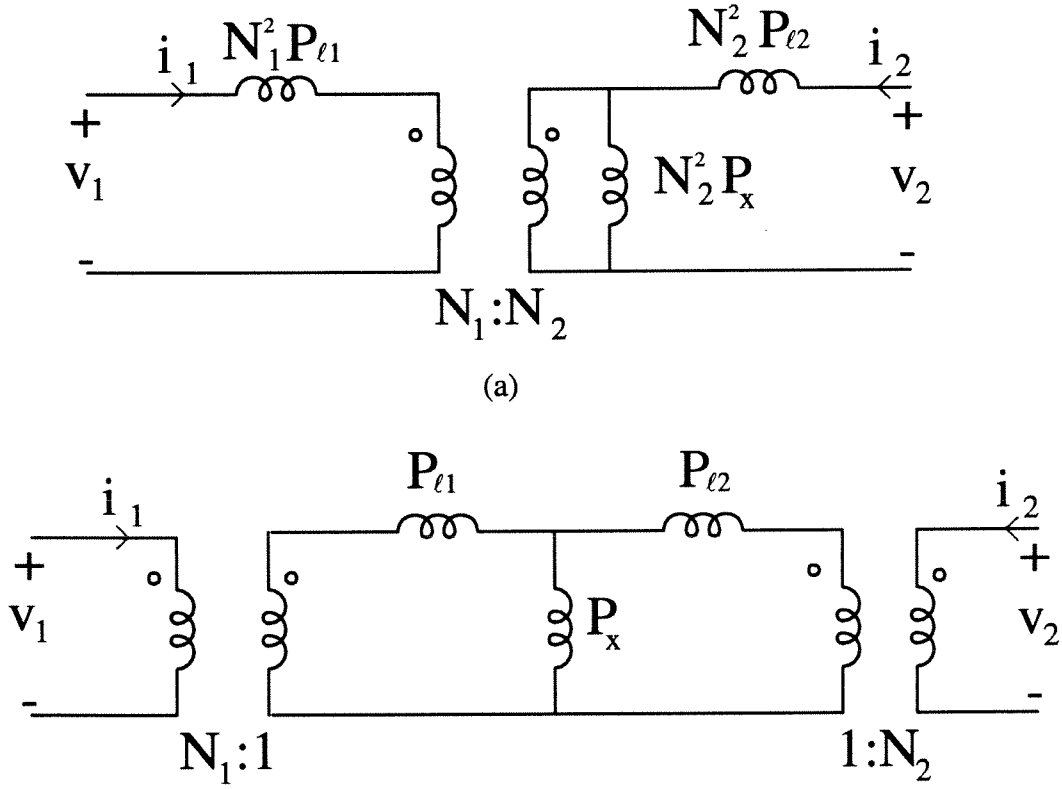

Figure 2.12: Inductance model scaled by N_2^2 (a) and inductance model scaled by 1 (b).

Chapter 3

Zero Ripple Condition

In this chapter the zero current ripple phenomenon is studied using the models reviewed in chapter 2.

In section 3.2, current ripple distribution in a coupled-inductor structure driven by identical voltage waveforms is studied. It is shown that current ripple in one of the windings can go to zero and even become negative for certain values of turns ratio and coupling.

In section 3.3, a more intuitive derivation of the zero ripple condition based on circuit model is given.

In sections 3.4 and 3.5 zero ripple condition is derived from coupled-inductor equations and from reluctance model respectively.

3.1 Introduction

As discussed in [1], if two (or more) inductors in a switching converter have proportional voltage waveforms, they can be magnetically coupled. In the following, without loss of generality, the case of equal voltage waveforms on all windings is studied. The proportional waveform case can be reduced to this case by scaling using winding turns ratio. In this chapter the case of two coupled inductors is considered. The extension to more than two windings is done in section 7.1.

A first advantage of coupled inductors with respect to separate inductors is size and weight reduction. This issue is discussed in [4] and in [5]. An interesting characteristic of coupled inductors is that by proper design unequal current ripple in the two windings can be obtained. Current ripple can be made zero or negative (decreasing current when a positive voltage is applied) on one of the windings. The case of zero current ripple

is particularly interesting from a practical point of view and represents a big advantage of the coupled-inductor approach: all current ripple is steered into one winding and the other one has ideally a purely DC current.

3.2 Coupled Inductors and Current Ripple Steering Effect

The current ripple steering effect is an intrinsic property of coupled inductors and can be studied without reference to a particular switching converter. Advantages of this approach are simplicity and the possibility to distinguish between intrinsic properties of the coupled inductors and effects of interactions between the converter and the coupled inductors. For example, a coupled-inductor structure designed for zero ripple can have some residual current ripple due to the fact that the turns ratio used is not exactly equal to the one required for ideal zero ripple. This is an intrinsic property of coupled inductors. But even if the exact turns ratio is used, the coupled-inductor structure will have some residual ripple when used in a switching converter due to the fact that the voltages applied by the converter to the two windings will not be exactly equal. The magnitude of this ripple depends on the switching converter characteristics.

Coupled inductors in a switching converter are subjected to 1) an AC voltage and 2) a DC current. As a result, flux in the core has a DC component due to the DC current and an AC component due to the AC voltage as shown in Fig. 3.1. As long as the magnetic core does not saturate, the effects of DC current and AC voltage can be studied separately. This is illustrated in Fig. 3.2. The DC current will be considered in chapter 9 where design equations are developed and conditions will be derived that ensure that the core does not saturate.

3.2.1 Choice of Transformer Circuit Model

In the following the case of coupled inductors driven by identical AC voltages is studied (Fig. 3.3) to determine currents i_1 and i_2. Notice that this situation is different from a standard transformer, where voltage is applied to the primary and some load is applied to the secondary. In this case both primary and secondary have an applied voltage.

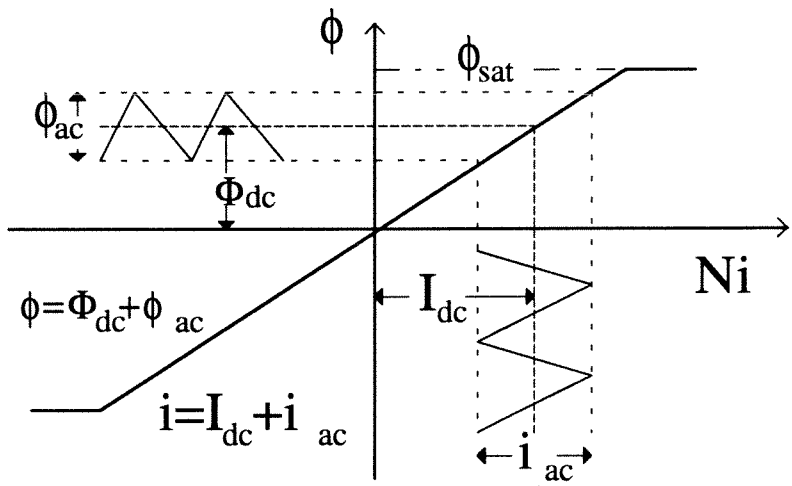

Figure 3.1: Separating AC voltage and DC current components.

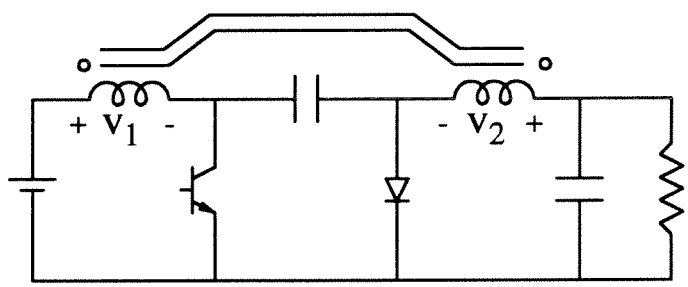

(a)

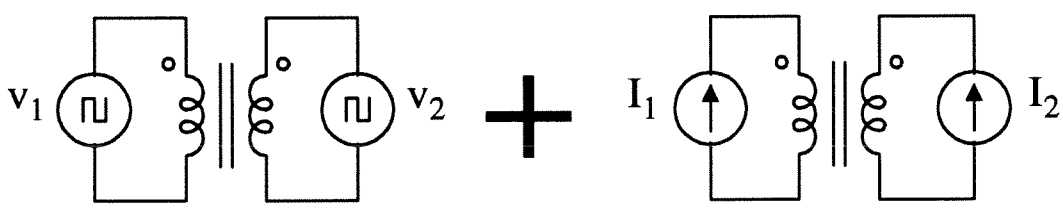

(b)

Figure 3.2: Coupled inductors driven by a Ćuk converter (a) and by equivalent AC voltage and DC current sources (b).

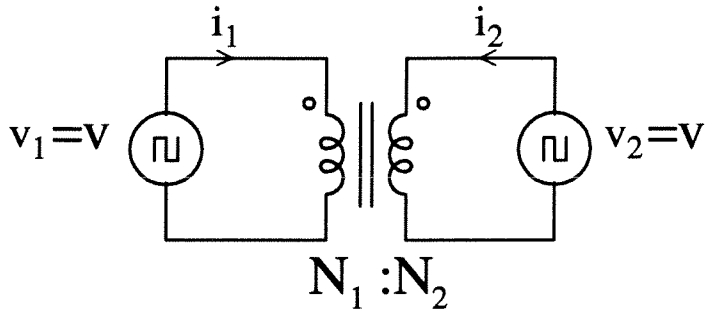

Figure 3.3: Coupled inductors driven by identical voltage sources.

In order to determine currents i_1 and i_2, it is necessary to define more precisely what the transformer symbol means. Transformer models with various levels of complexity are used in the study of electrical circuits. If a too simplistic model is used, it may be unable to capture whatever behavior of the circuit is of interest. The simplest possible transformer model is the ideal transformer that obeys the well-known voltage-scaling and current-scaling laws. A first nonideality that may be introduced is magnetizing inductance. A next step is to introduce leakage inductances. Finally, more complicated models exist that take into account winding losses, core losses, interwinding capacitance and so on.

The simplest model that describes the current ripple steering effect is the model with leakage inductances. In fact, in the case of an ideal transformer, the problem of Fig. 3.3 is not well-defined because the two voltage sources are connected directly in parallel as shown in Fig. 3.4. The circuit of Fig. 3.4 does not satisfy Kirchhoff voltage law. The problem becomes well-defined only if there is some impedance in the loop containing the two voltage sources. The situation does not improve if magnetizing inductance is introduced in the transformer model because magnetizing inductance is in *parallel* with the two voltage sources. The problem becomes well-defined if leakage inductance in *series* with the voltage sources is considered. Therefore, the circuit model used for coupled-inductor analysis is the usual transformer model of Fig. 2.4.

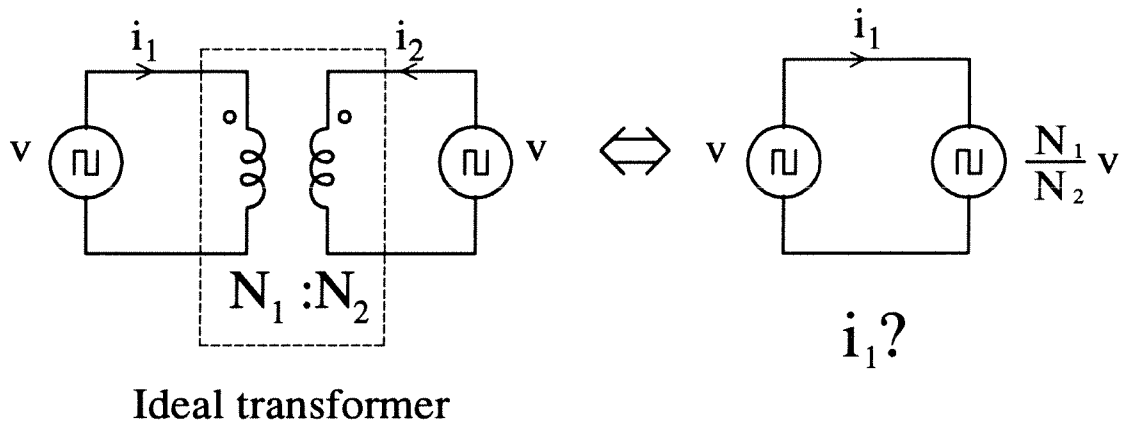

Figure 3.4: If coupled inductors are modeled as an ideal transformer, current i_1 is not well-defined.

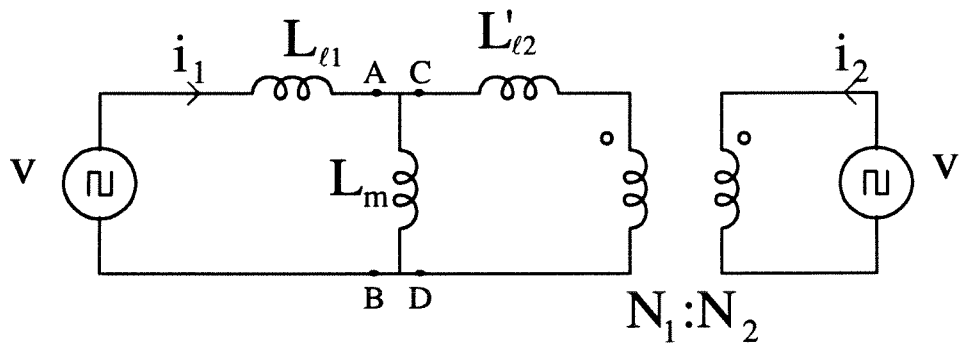

Figure 3.5: Circuit model used to determine currents i_1 and i_2. L_{l1}, L_m and L'_{l2} are constant, N_2 varies.

3.2.2 Current Ripple Variations and the Possibility of Negative Ripple

In this section current ripples i_1 and i_2 are calculated as a function of turns ratio. A coupled-inductor structure with a fixed number of turns N_1 and a variable number of secondary turns N_2 is considered. Primary leakage inductance L_{l1} and magnetizing inductance L_m are assumed to be constant. For simplicity secondary leakage inductance L_{l2} is reflected to the primary and called L'_{l2} as shown in Fig. 3.5. The advantage is that the primary number of turns is constant and inductance L'_{l2} can also be assumed to be a constant. In conclusion, all inductances of Fig. 3.5 are assumed to be constant.

The question to be answered is what happens to current ripples i_1 and i_2 as N_2 varies. To calculate current i_1 the portion of circuit to the right of points AB of Fig. 3.5

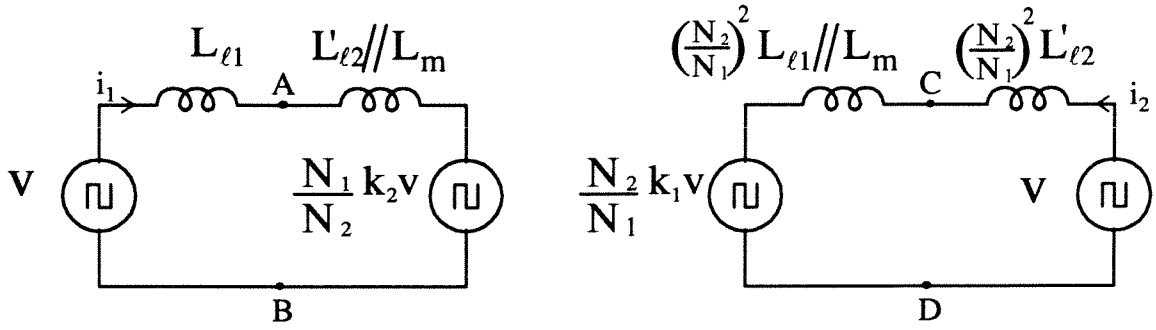

Figure 3.6: Thévenin equivalent model is used to calculate current i_1 (a) and i_2 (b).

is replaced by its Thévenin equivalent. The Thévenin equivalent voltage is the secondary voltage scaled by the turns ratio and the inductive voltage divider formed by L'_{l2} and L_m, i.e.,

$$v_{2\,Th} = \frac{N_1}{N_2} \frac{L_m}{L_m + L'_{l2}} v = \frac{N_1}{N_2} k_2 v$$

where k_2 is the secondary coupling coefficient defined in (2.3). The Thévenin equivalent inductance is

$$L_{2\,Th} = L'_{l2} \| L_m$$

The equivalent circuit is shown in Fig. 3.6a. Therefore, current i_1 is

$$i_1 = \left(1 - \frac{N_1}{N_2} k_2\right) \int \frac{v}{L_{l1} + L'_{l2} \| L_m} dt \tag{3.1}$$

In the same way, current i_2 can be determined by calculating the Thévenin equivalent circuit to the left of points CD in Fig. 3.5. This time all quantities are reflected to the secondary side of the transformer. As before

$$\begin{aligned} v_{1\,Th} &= \frac{N_2}{N_1} \frac{L_m}{L_m + L_{l1}} v = \frac{N_2}{N_1} k_1 v \\ L_{1\,Th} &= \left(\frac{N_2}{N_1}\right)^2 L_{l1} \| L_m \end{aligned}$$

The equivalent circuit is shown in Fig. 3.6b. Current i_2 is

$$i_2 = \frac{1 - \frac{N_2}{N_1} k_1}{\left(\frac{N_2}{N_1}\right)^2} \int \frac{v}{L_{l1} \| L_m + L'_{l2}} dt \tag{3.2}$$

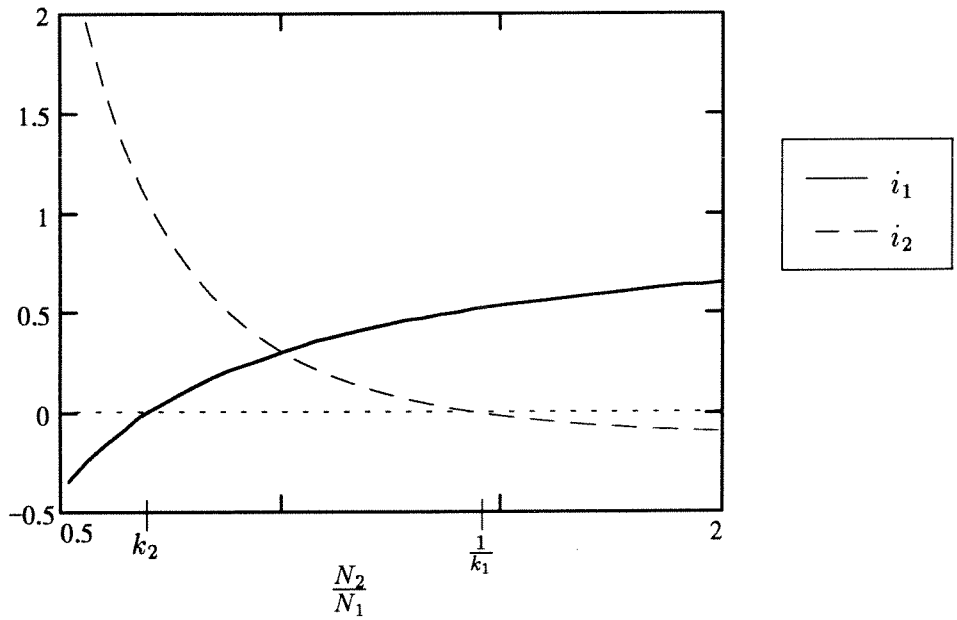

Figure 3.7: Normalized plot of amplitude of current ripples i_1 and i_2 as a function of turns ratio.

Notice that the expressions under the integral sign in (3.1) and (3.2) are approximately equal if $L_m \gg L_{l1}, L'_{l2}$. From these equations it is also evident that if v is a square voltage with zero average (typical case in PWM converters), currents i_1 and i_2 are triangular waveforms with amplitude proportional to the expressions in front of the integrals.

$$\begin{aligned} i_1 &\propto 1 - \frac{N_1}{N_2} k_2 \\ i_2 &\propto \frac{1 - \frac{N_2}{N_1} k_1}{\left(\frac{N_2}{N_1}\right)^2} \end{aligned} \tag{3.3}$$

Equations (3.3) represent normalized values of current ripple and can be plotted as a function of turns ratio N_2/N_1, as shown in Fig. 3.7 in the case $k_1 = k_2 = 0.7$.

The interesting thing to notice is that current ripples go to zero and become *negative*. The ripple currents for different values of N_2/N_1 are shown in Fig. 3.8. Notice that for

$$\frac{N_2}{N_1} = \frac{1}{k_1}$$

the secondary current ripple goes to zero. For bigger values of N_2/N_1 current ripple becomes "negative," i. e., when voltage is positive current decreases and vice versa. This

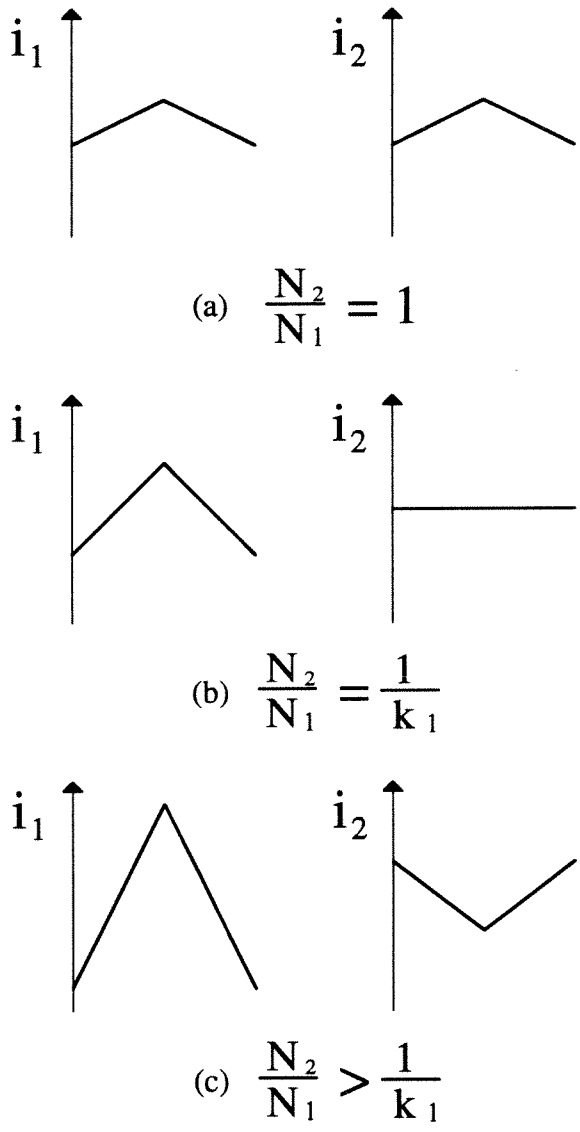

Figure 3.8: Current ripples for different values of turns ratio.

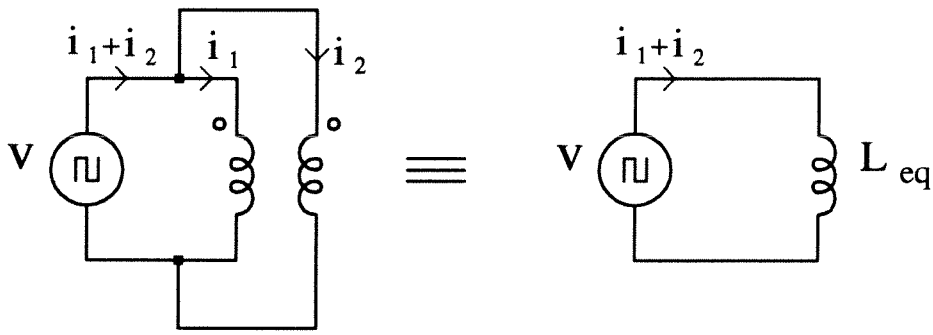

Figure 3.9: Total current ripple is always positive.

kind of behavior cannot be obtained from a network formed by a single voltage source and any interconnection of inductances only, because in that case the equivalent Thévenin impedance is inductive. This behavior is due to the presence of two voltage sources. If v is a sinusoidal voltage, in the negative ripple region current i_2 leads voltage v_2 by $\pi/2$. In some sense the circuit behaves as a capacitor.

In any case, the total current ripple $i_1 + i_2$ is always positive, because the impedance of the parallel connection of primary and secondary is inductive (Fig. 3.9). This means that if i_2 has negative ripple, then i_1 must have a positive ripple bigger than i_2 as shown in Fig. 3.8c. This situation is highly undesirable from a practical point of view.

The case of Fig. 3.8b is particularly important. It shows that zero current ripple can be achieved and that equation

$$k_1 = \frac{N_1}{N_2} \tag{3.4}$$

is the *zero ripple condition.* Fig. 3.7 shows that for

$$k_2 = \frac{N_2}{N_1}$$

there is zero current ripple on the primary winding. This is the zero ripple condition for the primary winding and all ripple is steered into the secondary winding.

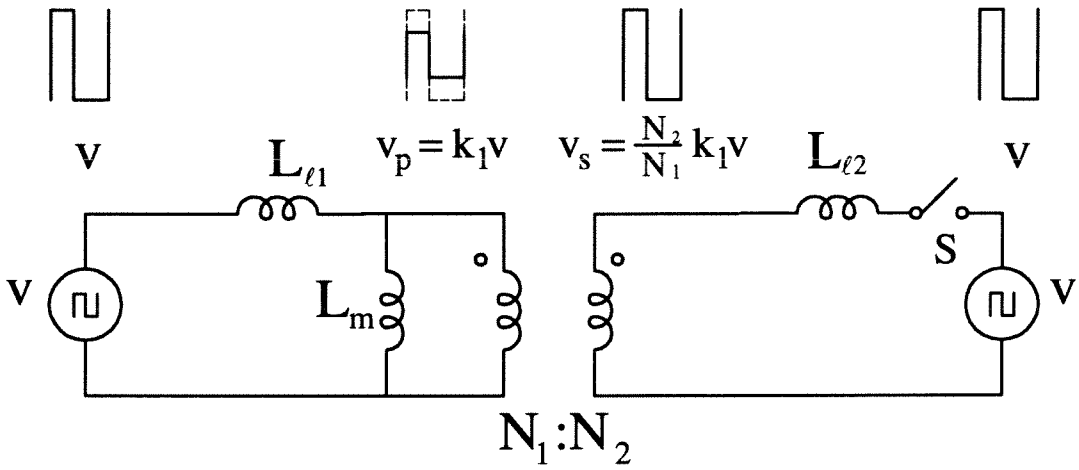

Figure 3.10: Voltages in coupled-inductor structure with open-circuited secondary side.

3.3 Intuitive Derivation of Zero Ripple Condition from Circuit Model

A more intuitive derivation of zero ripple condition from the transformer circuit model is given here. A coupled-inductor structure, represented by the equivalent circuit model, is driven by identical voltage sources in the primary and secondary. If the secondary voltage source is temporarily disconnected, voltages in various points of the circuit are as shown in Fig. 3.10. Leakage inductance L_{l1} and magnetizing inductance L_m form an inductive voltage divider, so that voltage v_p at the primary of the ideal transformer is

$$v_p = \frac{L_m}{L_{l1} + L_m} v = k_1 v$$

The voltage v_s at the transformer secondary is equal to v_p scaled by the transformer ratio

$$v_s = \frac{N_2}{N_1} v_p = \frac{N_2}{N_1} k_1 v$$

The turns ratio can be chosen in such a way to compensate the attenuation of voltage v due to the inductive voltage divider. In particular, if

$$\frac{N_2}{N_1} k_1 = 1 \tag{3.5}$$

then $v_s = v$. If the switch S of Fig. 3.10 is closed reconnecting the secondary side voltage source, no current will circulate through L_{l2} (provided that $L_{l2} \neq 0$) because the same

voltage is applied to the two terminals of L_{l2}. Therefore, there is zero current ripple in the secondary. Equation (3.5) is the zero ripple condition (3.4) derived earlier. In conclusion, zero current ripple on the secondary is obtained if the primary voltage source by itself induces on the secondary a voltage identical to the secondary voltage source.

3.4 Derivation of Zero Ripple Condition from Coupled-Inductor Equations

The zero ripple condition can also be derived from the coupled-inductor equations (2.6). If the same voltage is applied to both windings, these equations become

$$\begin{aligned} v &= L_{11}\frac{di_1}{dt} + M\frac{di_2}{dt} \\ v &= M\frac{di_1}{dt} + L_{22}\frac{di_2}{dt} \end{aligned} \tag{3.6}$$

Eliminating di_1/dt and solving for di_2/dt gives

$$\frac{di_2}{dt} = \frac{L_{11} - L_m}{L_{11}L_{22} - M^2}\, v$$

Imposing the condition $di_2/dt = 0$ gives

$$L_{11} = M \quad L_{22} \neq M$$

These conditions can be shown [5] to be equivalent to the zero ripple condition (3.4). Equations (3.6) can be represented by the three-inductor model shown in Fig. 3.11a. Fig. 3.11b shows the three-inductor model in the special case of zero current ripple in the secondary. This model can be useful for analytic and numerical analysis of switching converters with coupled inductors. For example, a Ćuk converter with coupled inductors and zero ripple in the output can be represented by the equivalent model of Fig. 3.12.

3.5 Derivation of Zero Ripple Condition from Reluctance Model

The zero ripple condition can be derived directly from the reluctance model. This is the method that will be more frequently used in the following chapters. The procedure is demonstrated through an example.

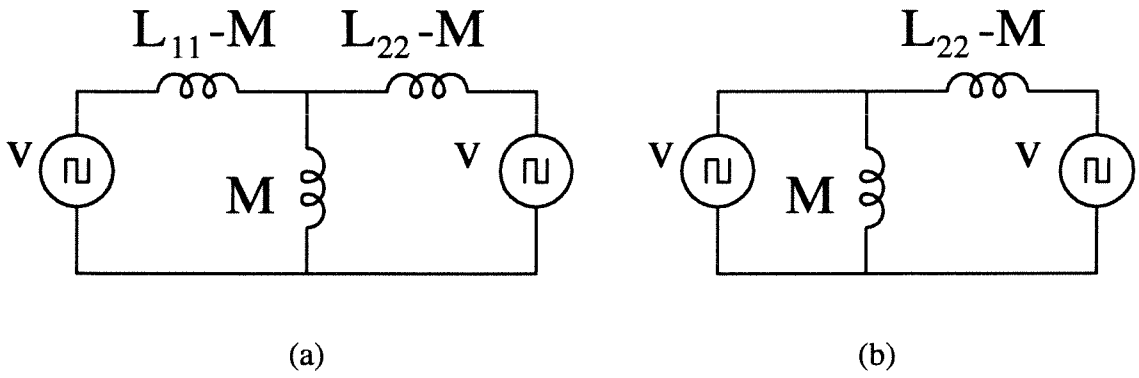

Figure 3.11: Inductance model from coupled-inductor equations in general (a) and for the special case of zero current ripple in the secondary (b).

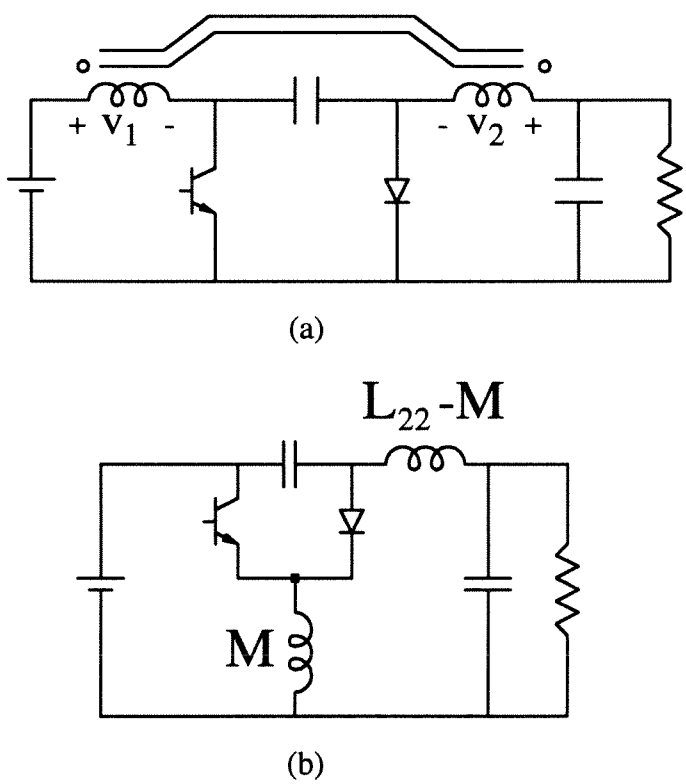

Figure 3.12: Coupled-inductor Ćuk converter (a) and equivalent model for zero current ripple in the output (b).

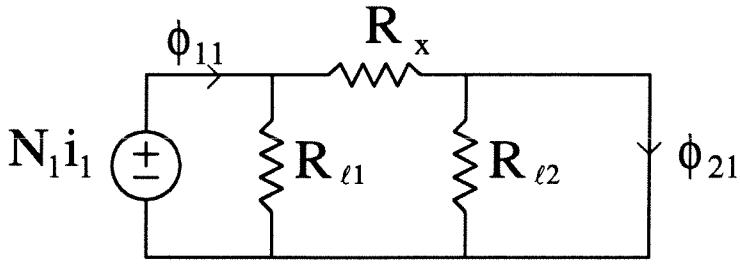

Figure 3.13: Reluctance model for $N_2 i_2 = 0$.

The magnetic structure considered in this example and its reluctance model are shown in Fig. 2.8. Reluctances $\mathcal{R}_{l1}$ and $\mathcal{R}_{l2}$ represent leakage flux of the primary and secondary windings respectively and $\mathcal{R}_x$ is the reluctance associated with gap x. Sources $N_1 i_1$ and $N_2 i_2$ represent flux linkages of primary and secondary winding respectively.

Notice that in this model reluctance of the magnetic core is neglected. This is a good approximation for cores with substantial air gaps where main flux ϕ_x is determined by air gap reluctance. This approximation will always be made in the following.

The first step is to impose the zero ripple condition $N_2 i_2 = 0$. Notice that in the reluctance model current linkages are represented by *voltage* sources, so the condition $N_2 i_2 = 0$ means that voltage source $N_2 i_2$ is *shorted*, as shown in Fig. 3.13. As a result, the secondary leakage reluctance $\mathcal{R}_{l2}$ is shorted and does not appear in the zero ripple condition. From this circuit the ratio ϕ_{21}/ϕ_{11} can be calculated as

$$\left.\frac{\phi_{21}}{\phi_{11}}\right|_{i_2=0} = \frac{\mathcal{R}_{l1}}{\mathcal{R}_x + \mathcal{R}_{l1}} \tag{3.7}$$

Application of Faraday's law to the primary and secondary windings gives

$$\phi_{11} = \frac{1}{N_1}\int v_1\, dt \tag{3.8}$$

$$\phi_{21} = \frac{1}{N_2}\int v_2\, dt \tag{3.9}$$

At this point condition $v_1 = v_2$ is imposed. From (3.7), (3.8) and (3.9)

$$\frac{N_1}{N_2} = \frac{\mathcal{R}_{l1}}{\mathcal{R}_x + \mathcal{R}_{l1}}$$

This condition is identical to (3.4). This can be seen directly from (3.7), since

$$k_1 = \left.\frac{\phi_{21}}{\phi_{11}}\right|_{i_2=0}$$

or, with an intermediate step, it can be seen from

$$\frac{\mathcal{R}_{l1}}{\mathcal{R}_x + \mathcal{R}_{l1}} = \frac{N_1^2/\mathcal{R}_x}{N_1^2/\mathcal{R}_x + N_1^2/\mathcal{R}_{l1}} = \frac{L_m}{L_m + L_{l1}} = k_1$$

Chapter 4

Sensitivity of Zero Ripple Condition and the Need for High Leakage

In the previous chapter the zero ripple condition for coupled inductors was derived. Ideally, if this condition is met and equal voltages are applied to the coupled inductors, one inductor will have zero current ripple and all ripple will be steered into the other one.

In a real-life situation with coupled inductors used in a converter, the zero ripple condition will not be perfectly met (*zero ripple condition mismatch*) and also the voltages imposed by the converter on the two windings will not be perfectly equal (*applied voltage mismatch*). As a result, there will be some residual ripple due to these nonidealities. It is important to determine the sensitivity of the zero ripple condition and estimate the residual current ripple as a function of *applied voltage mismatch* and *zero ripple condition mismatch.*

The sensitivity analysis in the next section shows that low sensitivity can be achieved if the magnetic coupling is not very good and there is significant leakage between the two windings. This explains why "leaky" magnetic structures like the ones shown at the end of this chapter are used for coupled-inductor applications.

4.1 Sensitivity Analysis

A coupled-inductor structure is driven by voltage sources v_1 and v_2, not necessarily identical. Moreover, zero ripple condition (3.4) is not exactly met. The transformer circuit model of Fig. 3.5 is used for this analysis. The residual ripple on the secondary side can be evaluated as in section 3.2 calculating the Thévenin equivalent voltage of the circuit to the left of points CD in Fig. 3.5 (see Fig. 3.6). The only difference is that now

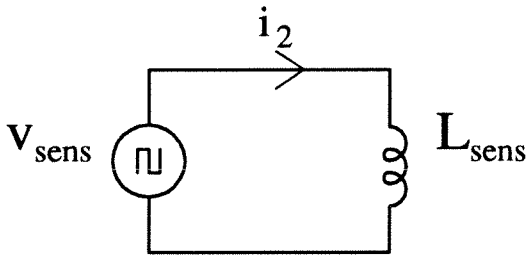

$$v_{sens} = v_2 - \frac{N_2}{N_1} k_1 v_1$$

$$L_{sens} = L_{l2} + \left(\frac{N_2}{N_1}\right)^2 (L_{l1} \| L_M)$$

Figure 4.1: Equivalent circuit to evaluate residual ripple.

v_1 and v_2 are not equal. The resulting circuit is shown in Fig. 4.1. The voltage source

$$v_{sens} = v_2 - \frac{N_2}{N_1} k_1 v_1$$

represents deviations from the ideal zero ripple case. In fact, if $v_1 = v_2$ (the driving voltages applied by the converter are identical) and zero ripple condition (3.4) is met, voltage v_{sens} is zero. The inductance

$$L_{sens} = L_{l2} + \left(\frac{N_2}{N_1}\right)^2 (L_{l1} \| L_M) \tag{4.1}$$

limits the residual ripple. Since $L_{l1} \ll L_M$, equation (4.1) can be approximated as

$$L_{sens} \approx L_{l2} + \left(\frac{N_2}{N_1}\right)^2 L_{l1}$$

Therefore, L_{sens} is approximately equal to the total leakage inductance reflected to the secondary side. In order to minimize residual ripple, it is necessary to maximize this inductance. Unlike in the design of conventional transformers, high leakage is a desired property in coupled inductor design.

4.2 Magnetic Structures with High Leakage

In order to have magnetic structures with high leakage, two different approaches can be taken.

A first approach is to add a separate series inductance that acts as leakage inductance. This is a brute-force approach and it requires a separate inductor. The advantage of reduction of number of separate magnetic elements provided by the coupled-inductor approach is lost.

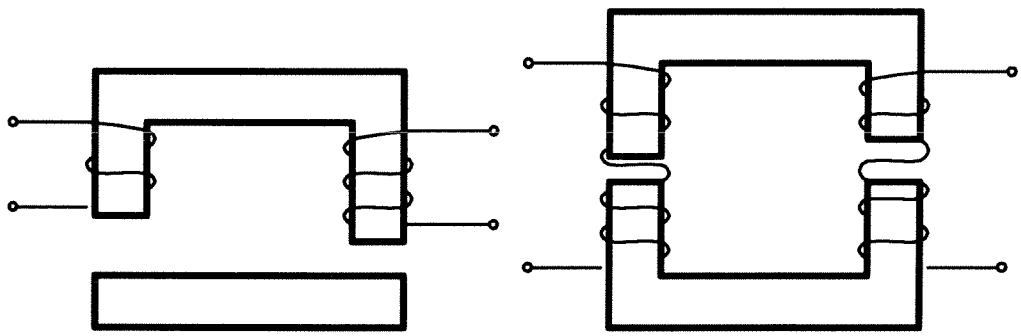

Figure 4.2: UI and UU core structures for coupled inductors.

The other possible approach is to maximize the leakage inductance of a single-core coupled-inductor structure. This is the preferred approach that takes full advantage of coupled inductors. Standard UI and UU cores with the two windings wound on separate legs as in Fig. 4.2 exhibit significant leakage inductance and have been successfully used in the past. Since inductors in a switching converter usually have a DC current, an air gap is needed to prevent core saturation. In the case of Fig. 4.2 both core legs are gapped.

Chapter 5

New Reluctance Model

From the derivation of the zero ripple condition given in chapter 3, the importance of accurate leakage models is apparent. As explained in the previous chapter, the preferred coupled inductor structure is UI and UU cores with windings on different legs as shown in Fig. 4.2.

In section 5.1, the reluctance model currently used for coupled-inductor design is reviewed.

In section 5.2, an experiment is presented that shows that air gap position in the coupled-inductor structure has a dramatic effect on coupled-inductor characteristics. The old reluctance model is unable to model this behavior.

In section 5.3, an improved reluctance model is introduced that successfully predicts the effect of air gap position. This model has three leakage reluctances that are constant for a given core.

In section 5.4, experimental results verifying the accuracy of the new model are presented. It is found that two of the leakage reluctances can be neglected, leaving a simple model with a single leakage reluctance.

In section 5.5, a method to model fringing flux at gaps is suggested.

5.1 Old Reluctance Model

The reluctance model used in the past [3] for coupled-inductor analysis and design is reviewed. This model will be referred to as "old model" in the rest of this work.

A UI core and its old reluctance model are shown in Fig. 5.1. Each winding has its own leakage flux, which is modelled by reluctances $\mathcal{R}_{l1}$ and $\mathcal{R}_{l2}$. Flux paths in air are assumed to be independent of gap sizes and therefore these leakage reluctances are

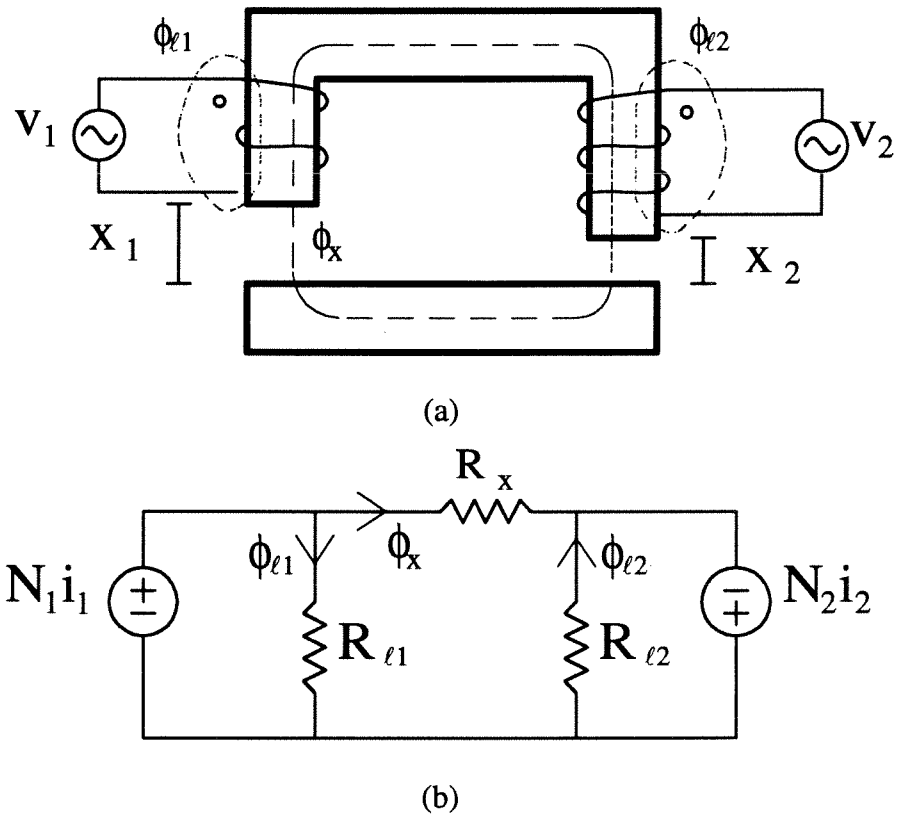

Figure 5.1: UI core (a) and its old reluctance model (b).

assumed to be constant for a certain magnetic core. The reluctance of the main flux path in the core is called $\mathcal{R}_x$. Since the core of Fig. 5.1 has a gap on each leg, $\mathcal{R}_x$ is the reluctance of the two gaps combined together and is given by

$$\mathcal{R}_x = \frac{x_1 + x_2}{\mu_0 S}$$

where S is core cross-section and x_1 and x_2 are gap widths. In this model, as in all models described in the following, the reluctance of the high-permeability core material is neglected.

Notice that in this model the two gaps are lumped together and only total gap size $x_1 + x_2$ is considered. Individual gap sizes are not taken into account by this model. For example, the same reluctance model is obtained for these three gap arrangements:

1. $x_1 = 2x$, $x_2 = 0$: gap concentrated on the primary leg.

2. $x_1 = 0$, $x_2 = 2x$: gap concentrated on the secondary leg.

3. $x_1 = x$, $x_2 = x$: gap evenly split between the two legs (spacer gap).

5.2 Effect of Gap Position

The following experiment dramatically demonstrates the effect of gap position on the characteristics of the magnetic structure and at the same time the inadequacy of the old model. In the experiment shown in Fig. 5.2, the two windings of a UU60 magnetic core (represented for simplicity as a UI core in Fig. 5.2) have the same number of turns. Winding 1 is driven with a sinusoidal voltage source v_1 and winding 2 is left open. The following measurements are performed: coupling coefficient k_1 (which is equal to v_2/v_1 because the two windings have the same number of turns), inductance L_1 seen from winding 1 and radiated noise measured using a telephone pickup placed at a fixed distance from the core. The issue of radiated noise is very important in power supply design, because power supplies can be physically close to noise-sensitive equipment like a magnetic storage device in a computer.

These measurements are repeated for three different gap arrangements: gap concentrated on leg 1 (Fig. 5.2a), gap concentrated on leg 2 (Fig. 5.2b) and spacer gap (Fig. 5.2c). The total gap is kept constant in the three cases so that reluctance $\mathcal{R}_x$ has the same value. Very similar results for the three sets of measurements were expected on the basis of the reluctance model of Fig. 5.1, but the measurements in Fig. 5.2a-b-c are very different. For example, coupling coefficient k_1 varies dramatically from 0.98 (almost perfect coupling) for gap concentrated on the primary to 0.57 for gap concentrated on the secondary. These variations cannot be explained by the old model. Since $\mathcal{R}_x$ is the same in the three cases, the only way to obtain good agreement between model and experiment is to arbitrarily assign three different values to leakage reluctance $\mathcal{R}_{l1}$ in the three cases ($\mathcal{R}_{l2}$ does not have any effect because winding 2 is open and the equivalent voltage source $N_2 i_2$ is shorted).

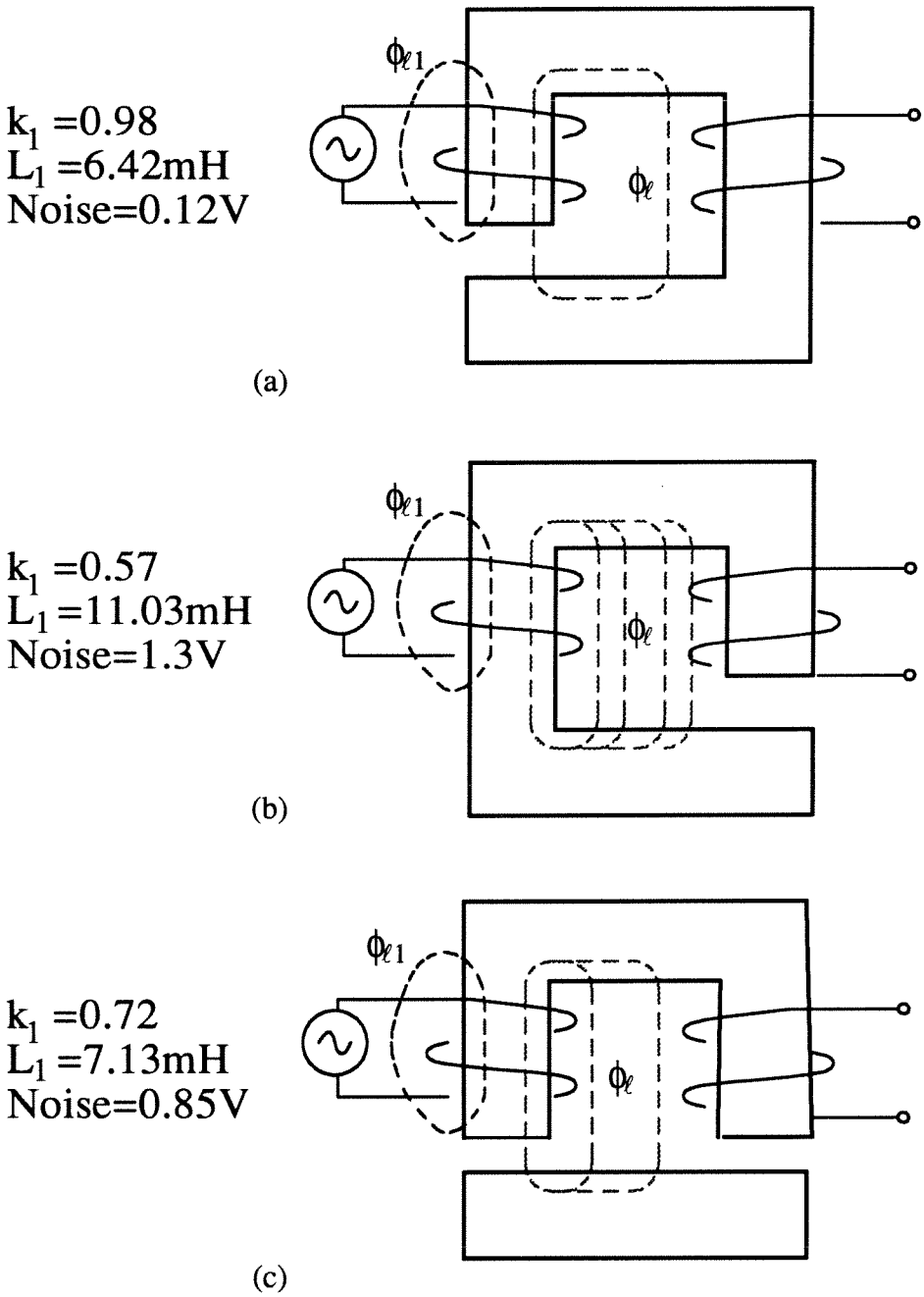

Figure 5.2: Same total gap distributed differently results in very different measured values of coupling coefficient k_1, inductance L_1 and radiated noise.

5.3 New Reluctance Model

The experimental results of Fig. 5.2a-b-c can be qualitatively explained as follows. Let us look, for example, at coupling k_1 for the structures of Fig. 5.2a and Fig. 5.2b: in the first case coupling is almost perfect (0.98) while in the second case it is only 0.57. In the first case the gap is very close to winding 1. The *mmf* due to the current in winding 1 drops on the gap, so that most of the UI core (except the small portion between winding 1 and the gap) is at a constant magnetic potential. As a result, the leakage in air is small and most of the flux couples with winding 2, so that coupling is good. In the second case the gap is far from winding 1. The upper part of the U piece and the I piece are at a different magnetic potential, so that there is significant leakage flux and coupling is much worse.

An alternative explanation goes as follows. The leakage flux can be divided into two parts, ϕ_{l1} and ϕ_l, as shown in Fig. 5.2a-b. Flux ϕ_{l1} closes before the gap on leg 1 and flux ϕ_l closes after it. Flux ϕ_{l1} is not affected by the size of the gap on leg 1 and is the same in the two cases. On the contrary, flux ϕ_l goes through the gap on leg 1 and therefore is affected by it. As an effect of gap reluctance, ϕ_l is smaller in the case of Fig. 5.2a and therefore coupling is better.

The different values of inductance L_1 and radiated noise can be explained by similar reasoning. As explained above, leakage flux is bigger for the structure of Fig. 5.2b. Leakage flux contributes to the value of inductance L_1, making it bigger in the case of Fig. 5.2b. Radiated noise is leakage flux in air and therefore it is also bigger in the case of Fig. 5.2b.

From the previous discussion the conclusion is that leakage flux from a winding must be divided into two parts: flux that closes in air *before* crossing the gap and flux that closes in air *after* crossing the gap. This is shown in Fig. 5.3a.

A modified reluctance model that distinguishes between these two leakage flux components is shown in Fig. 5.3b. $\mathcal{R}_{x1}$ and $\mathcal{R}_{x2}$ are the reluctances of gaps x_1 and x_2. $\mathcal{R}_{l1}$ and $\mathcal{R}_{l2}$ are the reluctances of flux paths in air that do not cross the gaps. $\mathcal{R}_l$ is the reluctance of leakage flux paths that cross the gaps.

Measurements on different cores (some of them presented in section 5.4) show that

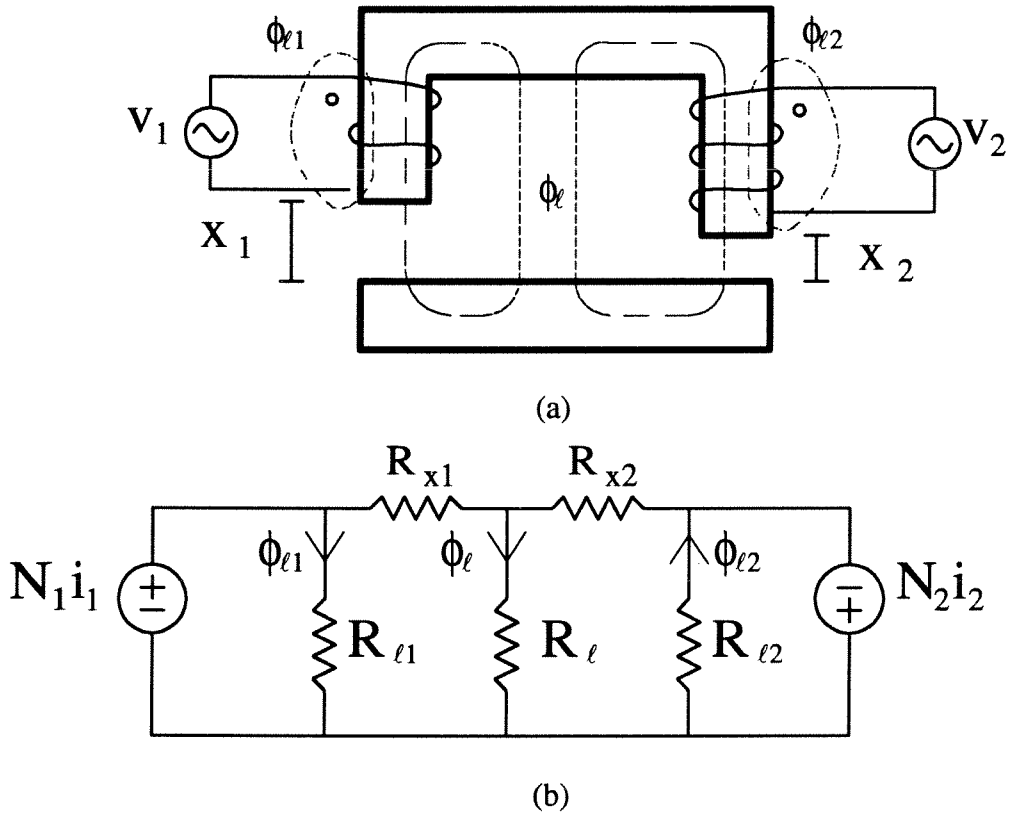

Figure 5.3: New reluctance model separately models flux ϕ_l with reluctance $\mathcal{R}_l$.

for a given core geometry, reluctances $\mathcal{R}_{l1}$, $\mathcal{R}_{l2}$ and $\mathcal{R}_l$ are constant irrespective of gap arrangement and gap sizes used. Only $\mathcal{R}_{x1}$ and $\mathcal{R}_{x2}$ depend on the gaps.

Leakage reluctances $\mathcal{R}_{l1}$, $\mathcal{R}_{l2}$ and $\mathcal{R}_l$ can be experimentally determined from a single set of measurements. Since gap values are known, reluctances $\mathcal{R}_{x1}$ and $\mathcal{R}_{x2}$ can be calculated from the well-known formula. That leaves three unknowns, $\mathcal{R}_{l1}$, $\mathcal{R}_{l2}$ and $\mathcal{R}_l$. A non-saturated coupled-inductor structure is a linear reciprocal two-port, and three independent measurements can be performed. Therefore, the three unknowns can be experimentally determined. The main advantage of this model is that from a single set of measurements on a certain core with any value of gaps, reluctances $\mathcal{R}_{l1}$, $\mathcal{R}_{l2}$ and $\mathcal{R}_l$ can be uniquely determined. These leakage reluctances completely characterize the core, and the model accurately describes the magnetic structure for any other values of gaps.

In particular this model is valid for concentrated gaps. For example, if gap is concen-

trated on the primary, the model has $\mathcal{R}_{x2} = 0$ and $\mathcal{R}_l$ and $\mathcal{R}_{l2}$ are directly in parallel.

It is interesting to notice that in the case of concentrated gap, the old model and the new model are identical with the following equalities between reluctances:

$$\begin{array}{ll} \text{Primary gap} & \text{Secondary gap} \\ 0 = \mathcal{R}_{x2}|_{new} & 0 = \mathcal{R}_{x1}|_{new} \\ \mathcal{R}_{l1}|_{old} = \mathcal{R}_{l1}|_{new} & \mathcal{R}_{l1}|_{old} = \mathcal{R}_{l1}\|\mathcal{R}_l|_{new} \\ \mathcal{R}_x|_{old} = \mathcal{R}_{x1}|_{new} & \mathcal{R}_x|_{old} = \mathcal{R}_{x2}|_{new} \\ \mathcal{R}_{l2}|_{old} = \mathcal{R}_l\|\mathcal{R}_{l2}|_{new} & \mathcal{R}_{l2}|_{old} = \mathcal{R}_{l2}|_{new} \end{array} \tag{5.1}$$

In the case of concentrated gaps, leakage reluctances of the old model are constant and independent of gap size because they are equal to combinations of leakage reluctances of the new model. However, as can be seen from equations (5.1), different values of leakage reluctances need to be used depending on whether the gap is on the primary or on the secondary. Therefore, using equations (5.1) it is possible to obtain the new model leakage reluctances from data expressed in terms of the old model leakage reluctances. Equations (5.1) give only two conditions on the three leakage reluctances of the new model. However, a symmetry argument implies that for symmetric cores

$$\mathcal{R}_{l1}|_{\text{new}} = \mathcal{R}_{l2}|_{\text{new}}$$

and therefore all three leakage reluctances in the new model can be determined.

The old model and the new model are different if gaps are present on both legs and it is not possible to obtain the new model leakage reluctances from old model data unless the gap sizes used in the measurement are known.

5.4 Experimental Verification of New Model

To validate the proposed reluctance model, measurements are performed on different standard UI and UU cores for different values of spacer and concentrated gaps. These experiments show that reluctances $\mathcal{R}_{l1}$, $\mathcal{R}_{l2}$ and $\mathcal{R}_l$ are approximately constant for a given core geometry.

The measurement procedure is as follows:

1. An equal number of turns is wound on each core leg. The number of turns is chosen to fully utilize the window area.

2. Primary and secondary inductances are measured using an HP 4261A LCR meter, and coupling coefficients k_1 and k_2 are measured using an HP 3577A network analyzer. Measurements are repeated for different values of concentrated and spacer gaps.

3. From each set of measurements reluctances $\mathcal{R}_{l1}$, $\mathcal{R}_{l2}$ and $\mathcal{R}_l$ are determined. These values are then averaged to obtain a unique value for each reluctance. It is worth noticing that more accurate values of leakage reluctances can be obtained by performing measurements on cores with substantial air gaps, because leakage reluctances appear in parallel with gap reluctances and measurement sensitivity is high if gap reluctance is much smaller than the leakage reluctance that appears in parallel with it. Therefore, in the averaging of measured reluctances, bigger weight is given to measurements performed in the case of substantial gaps.

4. Measurements are compared with predictions using the reluctance model with the measured average values of leakage reluctances.

Both at points 3 and 4 corrections for fringing flux at gaps are introduced in the reluctance model in the form of a fringing reluctance as described in section 5.5.

Tables 5.1 and 5.2 show comparison of measured and predicted values of coupling coefficient k_1 and inductance L_1 for a UI60 core with 80 turns on each winding in the case of spacer gap, primary leg gap and secondary leg gap.

5.4.1 Simplified Reluctance Model

Measurements for various standard cores are shown in Table 5.3. From these measurements it appears that $\mathcal{R}_{l1}$ and $\mathcal{R}_{l2}$ are an order of magnitude bigger than $\mathcal{R}_l$. The same result was found for various EI cores (the reluctance model for EI cores will be introduced in section 7.2.1). Therefore $\mathcal{R}_{l1}$ and $\mathcal{R}_{l2}$ can be neglected without introducing significant errors. Experimental validation of this approximation is given in section 5.4.

Spacer gap						
gap *[mm]*	k_1			L_1 *[μH]*		
	Th.	*Exp.*	*Err.*	*Th.*	*Exp.*	*Err.*
0.39	0.80	0.77	3.8%	2842	2740	3.7%
0.69	0.70	0.68	2.9%	1820	1830	0.5%
1.00	0.62	0.62	0%	1400	1450	3.4%
1.31	0.57	0.57	0%	1176	1220	3.6%
1.63	0.52	0.53	1.9%	1033	1100	6.1%
1.94	0.49	0.50	2.0%	937	1000	6.3%
2.25	0.46	0.47	2.1%	867	910	4.7%
2.57	0.44	0.45	2.2%	812	880	7.7%
2.89	0.42	0.43	2.3%	768	837	8.2%
3.20	0.40	0.41	2.4%	734	800	8.2%
3.51	0.39	0.39	0%	706	770	8.3%

Table 5.1: Comparison of measured and predicted values of coupling coefficient k_1 and inductance L_1 for a UI60 core in the case of spacer gap. Reluctance values used in the model are: $\mathcal{R}_{l1} = \mathcal{R}_{l2} = 60\ [1/\mu H]$, $\mathcal{R}_l = 6.1\ [1/\mu H]$, $\mathcal{R}_{fring} = 18\ [1/\mu H]$

An intuitive justification for this approximation can be given looking at Fig. 5.3a: winding 1 is very close to gap x_1, so that flux ϕ_{l1} that closes in air before crossing gap x_1 is small compared to flux ϕ_l that closes in air after crossing the gap. Neglecting reluctances $\mathcal{R}_{l1}$ and $\mathcal{R}_{l2}$ reduces the reluctance model to a T model. An advantage of this model with respect to the complete model of Fig. 5.3b is that it can be fully determined from a single set of measurements. In the previous complete model it was necessary to assume that reluctances $\mathcal{R}_{x1}$ and $\mathcal{R}_{x2}$ were known.

At this point it is instructive to compare the old model with the new simplified model. Fig. 5.4 shows a comparison of the old and the new model. It is clear that one model can be obtained from the other with a Y–Δ transformation. In general any two-port has an

Primary leg gap						
gap *[mm]*	k_1			L_1 *[μH]*		
	Th.	*Exp.*	*Err.*	*Th.*	*Exp.*	*Err.*
0.52	0.97	0.96	1%	3942	3740	5%
0.95	0.95	0.95	0%	2367	2410	1.8%
1.30	0.94	0.94	0%	1854	1810	2.4%
1.45	0.94	0.94	0%	1710	1660	2.9%

Secondary leg gap						
gap *[mm]*	k_1			L_1 *[μH]*		
	Th.	*Exp.*	*Err.*	*Th.*	*Exp.*	*Err.*
0.52	0.77	0.75	1.9%	4991	4800	3.8%
0.95	0.66	0.65	1.2%	3416	3500	2.5%
1.30	0.60	0.57	4.6%	2903	2930	9.2%
1.45	0.58	0.56	3.6%	2760	2800	1.5%

Table 5.2: Comparison of measured and predicted values of coupling coefficient k_1 and inductance L_1 for a UI60 core in the case of primary leg gap and secondary leg gap. Reluctance values used in the model are: $\mathcal{R}_{l1} = \mathcal{R}_{l2} = 60\ [1/\mu H]$, $\mathcal{R}_l = 6.1\ [1/\mu H]$, $\mathcal{R}_{fring} = 18\ [1/\mu H]$

Core	$\mathcal{R}_l$ $[1/\mu H]$	$\mathcal{R}_{l1}, \mathcal{R}_{l2}$ $[1/\mu H]$
UI60	6.10	60
UU60	5.71	250
UI45	6.99	40

Table 5.3: Measured leakage reluctances for various standard cores show that $\mathcal{R}_{l1}$, $\mathcal{R}_{l2} \gg \mathcal{R}_l$.

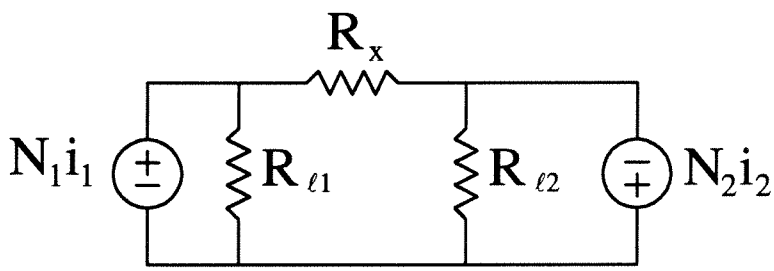

Π model
R ℓ1 and R ℓ2 dependent on gap

(a)

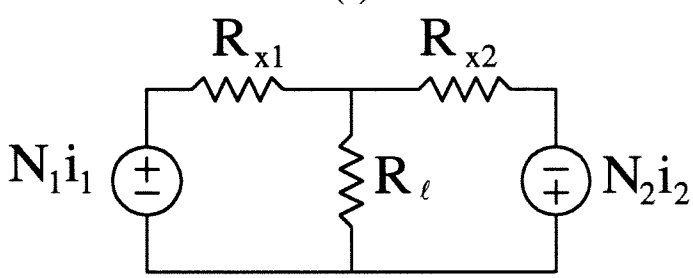

T model
R ℓ independent of gap

(b)

Figure 5.4: Old reluctance model (a) and new simplified model (b) are equivalent for given gaps. The advantage of the new model is that reluctance $\mathcal{R}_l$ *does not change with gaps.*

equivalent Π model and an equivalent T model. A natural question is:

If the two models are equivalent, what is the advantage of the new model?

The advantage is that $\mathcal{R}_l$ in the new model is constant and independent of gaps, whereas $\mathcal{R}_{l1}$ and $\mathcal{R}_{l2}$ in the old model vary with gaps.

The fact that $\mathcal{R}_l$ in the new model is independent of gaps has been experimentally established (see Tables 5.1-5.2). The fact that $\mathcal{R}_{l1}$ and $\mathcal{R}_{l2}$ change with gaps can be proven as a consequence of $\mathcal{R}_l$ being constant. The argument goes as follows: for a certain gap value the reluctances in the new model have some value that can be experimentally measured. Using a Y–Δ transformation reluctance $\mathcal{R}_{l1}$ in the old model, for example, can be calculated as

$$\mathcal{R}_{l1} = \frac{\mathcal{R}_l\mathcal{R}_{x1} + \mathcal{R}_l\mathcal{R}_{x2} + \mathcal{R}_{x1}\mathcal{R}_{x2}}{\mathcal{R}_{x2}} \tag{5.2}$$

If gaps are changed, $\mathcal{R}_{x1}$ and $\mathcal{R}_{x2}$ vary accordingly but $\mathcal{R}_l$ remains constant. Therefore $\mathcal{R}_{l1}$, which is a function of $\mathcal{R}_{x1}$ and $\mathcal{R}_{x2}$, has to change with gaps.

5.4.2 Experimental Verification of Simplified Model and Comparison with Complete Model

The same experimental data on a UI60 core used in section 5.4 are compared with theoretical predictions using the simplified reluctance model. Leakage reluctance $\mathcal{R}_l$ and fringing reluctance $\mathcal{R}_{fring}$ are reevaluated for a best fit of the experimental data using the same procedure described in section 5.4. Results are shown in Tables 5.4 and 5.5. The maximum relative error on k_1 is less than 7% and the maximum relative error on L_1 is less than 11%. Figures 5.5-5.6-5.7 show a comparison of experimental data and predictions with the complete model and the simplified model. The fact that very similar predictions are obtained from the two models justifies the approximation of the simplified model.

5.5 Modeling of Fringing Flux

In order to accurately describe the behavior of gapped magnetic circuits, it is important to model the fringing flux at gaps. It is well known that flux going through a

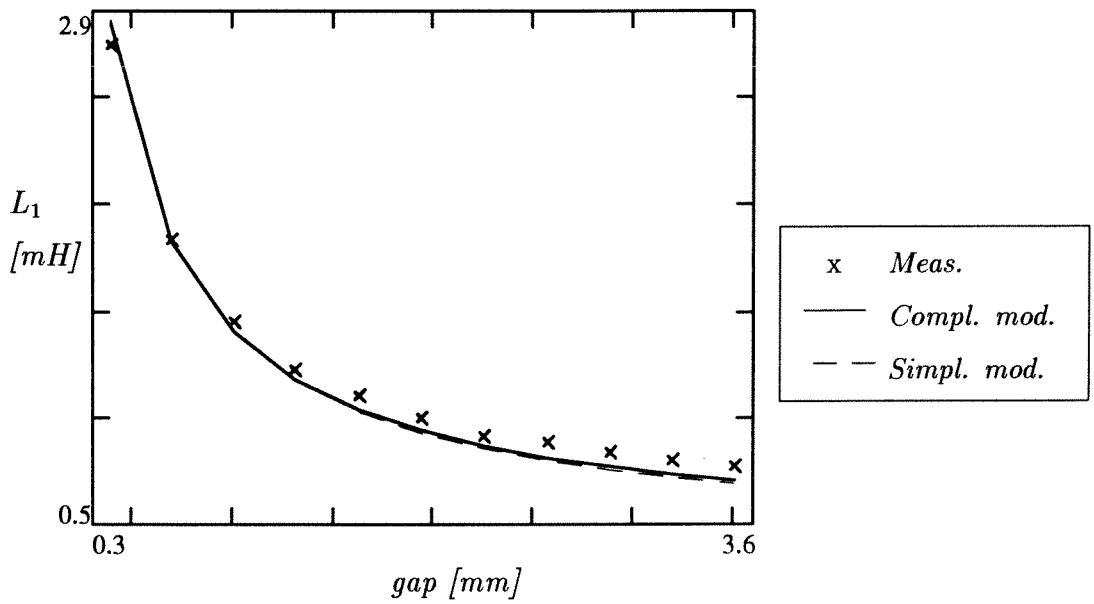

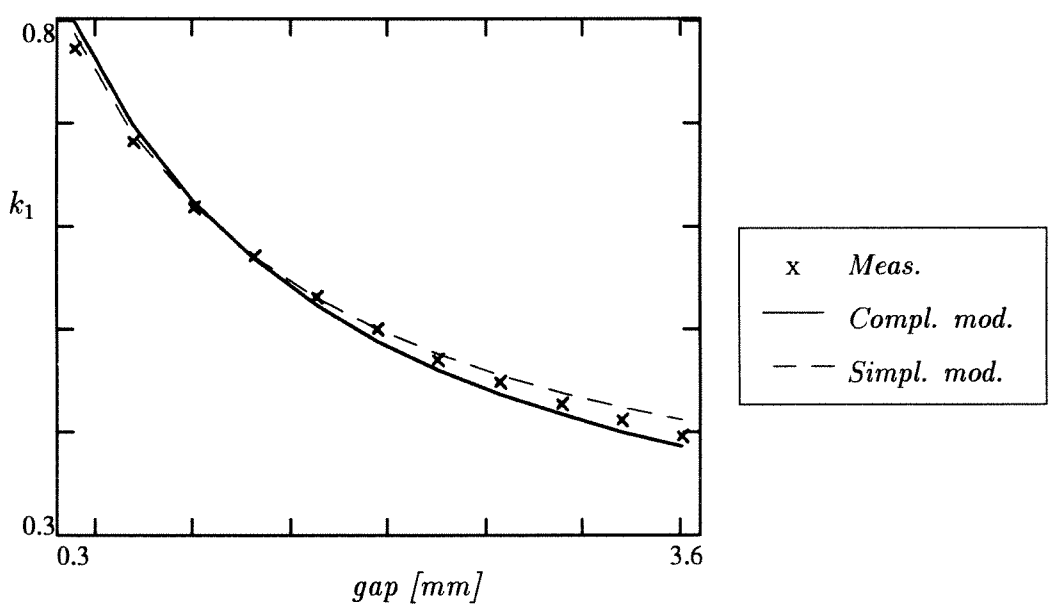

Figure 5.5: Comparison of predictions using the simplified model and the complete model in the case of spacer gap.

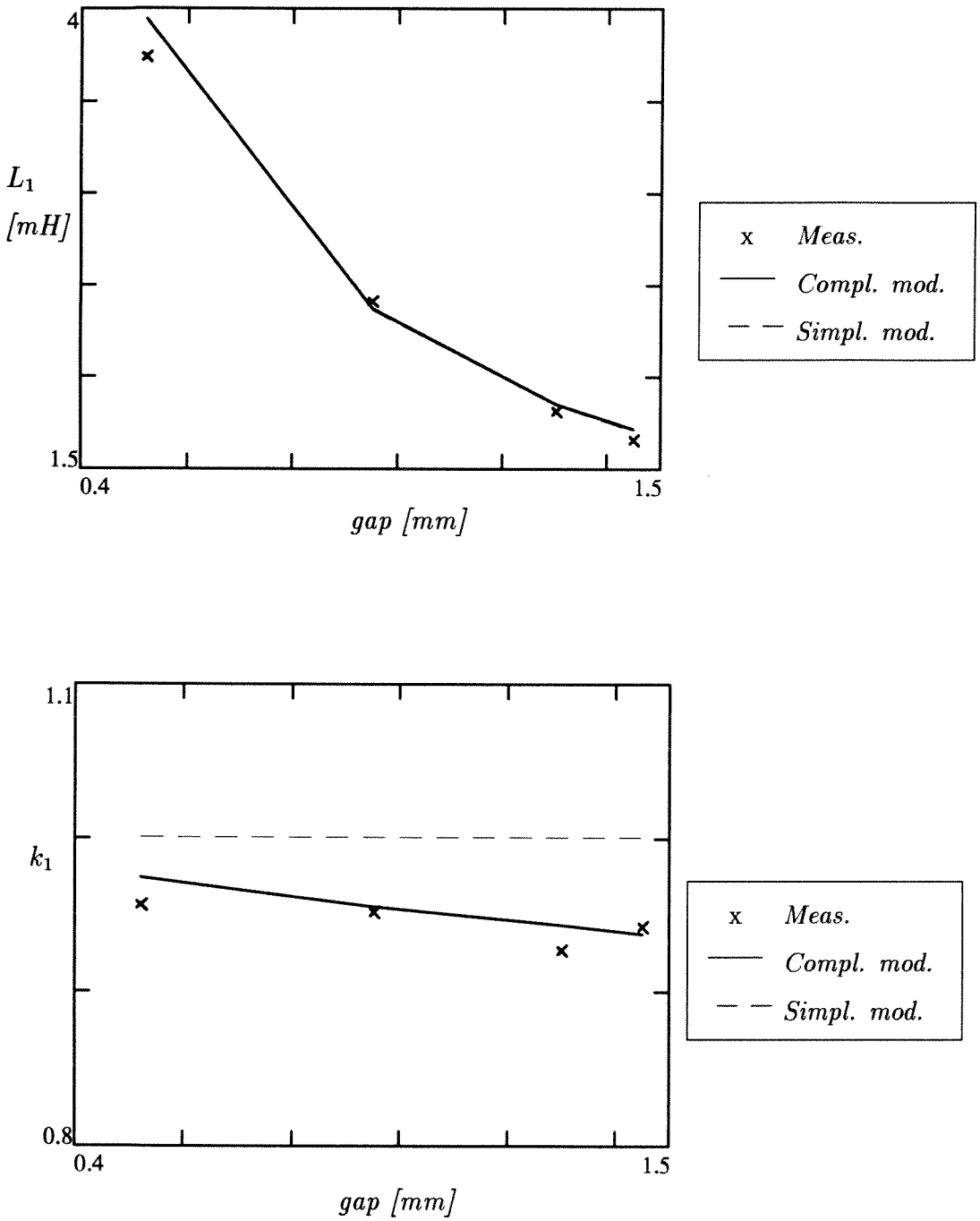

Figure 5.6: Comparison of predictions using the simplified model and the complete model in the case of primary gap. The prediction plots are obtained in the following way: predicted values are calculated only for the values of gaps used for measurements and these values are then connected by straight lines. This explains why prediction plots are not smooth. In the upper plot the two prediction plots are practically undistinguishable.

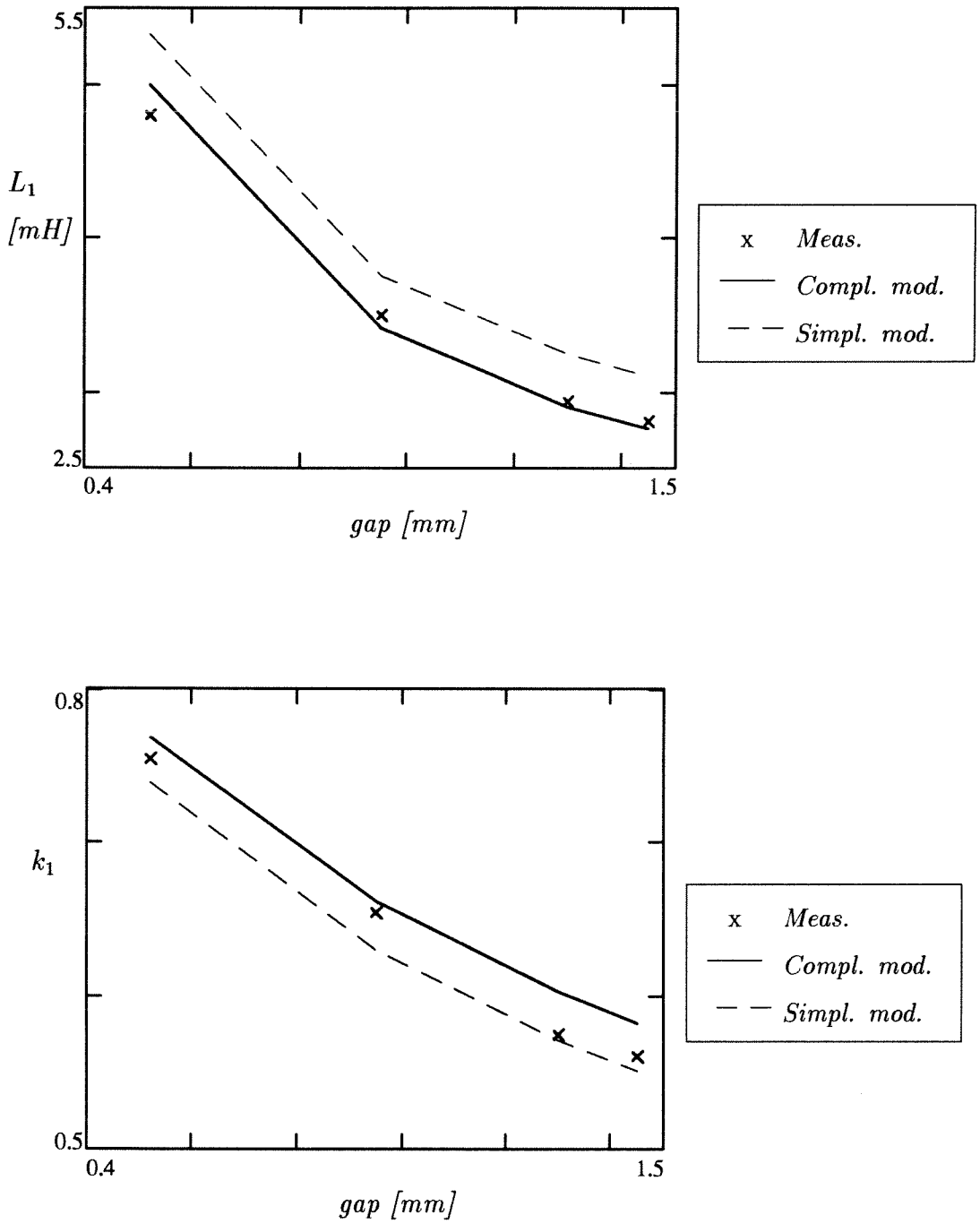

Figure 5.7: Comparison of predictions using the simplified model and the complete model in the case of secondary gap. The prediction plots are obtained in the following way: predicted values are calculated only for the values of gaps used for measurements and these values are then connected by straight lines. This explains why prediction plots are not smooth.

Spacer gap						
gap *[mm]*	k_1			L_1 *[μH]*		
	Th.	*Exp.*	*Err.*	*Th.*	*Exp.*	*Err.*
0.39	0.79	0.77	2.6%	2860	2740	4.3%
0.69	0.69	0.68	1.5%	1820	1830	0.5%
1.00	0.62	0.62	0%	1400	1450	3.4%
1.31	0.57	0.57	0%	1170	1220	4.1%
1.63	0.53	0.53	0%	1020	1100	7.3%
1.94	0.50	0.50	0%	927	1000	7.3%
2.25	0.48	0.47	2%	855	910	4.6%
2.57	0.46	0.45	2.2%	798	880	6%
2.89	0.44	0.43	2.3%	753	837	10%
3.20	0.42	0.41	2.4%	718	800	10.2%
3.51	0.41	0.39	5.1%	689	770	10.5%

Table 5.4: Measurements and predictions using the simplified model in the case of spacer gap. Reluctance values used in the model are: $\mathcal{R}_l = 4.6\ [1/\mu H]$, $\mathcal{R}_{fring} = 14\ [1/\mu H]$

gap tends to spread out decreasing gap reluctance. This effect becomes more and more significant as gap size increases. A usual way to take this effect into account (which we can call "standard method") is to add to leg dimensions a length equal to the gap thickness. For a leg of dimensions a and b with a gap x, gap reluctance is calculated as

$$\mathcal{R}_x = \frac{x}{\mu_0(a+x)(b+x)} \tag{5.3}$$

An alternative way suggested in [5] (which we can call "fringing reluctance method") is to put a fixed reluctance $\mathcal{R}_{fring}$ in parallel with the total gap reluctance as shown in Fig. 5.8. This reluctance is constant for a given core. The effect of this reluctance is to put an upper bound on gap reluctance regardless of gap size. Fig. 5.9 shows a comparison of gap reluctance values measured on a UI60 core and predicted using the two methods.

Primary leg gap						
gap *[mm]*	k_1			L_1 *[μH]*		
	Th.	*Exp.*	*Err.*	*Th.*	*Exp.*	*Err.*
0.52	1.0	0.96	4.2%	3937	3740	5.3%
0.95	1.0	0.95	5.3%	2360	2410	2.1%
1.30	1.0	0.94	6.4%	1850	1810	2.2%
1.45	1.0	0.94	6.4%	1705	1660	2.7%

Secondary leg gap						
gap *[mm]*	k_1			L_1 *[μH]*		
	Th.	*Exp.*	*Err.*	*Th.*	*Exp.*	*Err.*
0.52	0.74	0.75	1.3%	5330	4800	11%
0.95	0.63	0.65	3%	3750	3500	7.1%
1.30	0.57	0.57	0%	3240	2930	10.5%
1.45	0.55	0.56	1.8%	3100	2800	10.7%

Table 5.5: Measurements and predictions using the simplified model in the case of primary leg gap and secondary leg gap. Reluctance values used in the model are: $\mathcal{R}_l = 4.6\ [1/\mu H]$, $\mathcal{R}_{fring} = 14\ [1/\mu H]$

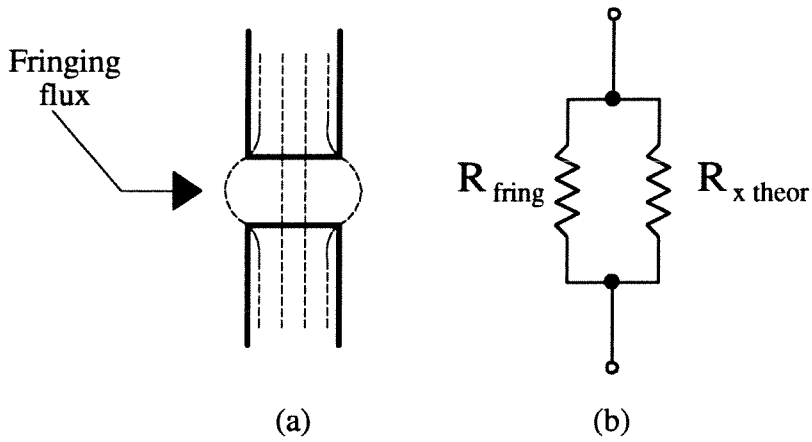

Figure 5.8: Fringing flux at gap (a) is modelled by a constant reluctance $\mathcal{R}_{fring}$ in parallel with theoretical gap reluctance (b).

The fringing reluctance method is more accurate for big gaps. Therefore, correction for fringing flux at gaps can be introduced in the models discussed previously by putting in parallel to each gap reluctance a fringing reluctance $\mathcal{R}_{fring}$. If the simplified model is used, fringing reluctances can also be easily measured. From a single set of measurements it is possible to calculate values for $\mathcal{R}_{x1}$, $\mathcal{R}_{x2}$ and $\mathcal{R}_l$. Fringing reluctance for leg 1 can be calculated from

$$\mathcal{R}_{x1} = \mathcal{R}_{x1theor} \| \mathcal{R}_{fring}$$

where $\mathcal{R}_{x1theor}$ is the theoretical value calculated from the well-known formula. In an analogous way, fringing reluctance for leg 2 can be calculated. Since UI and UU cores are symmetric, the same value of fringing reluctance is used for the two gaps.

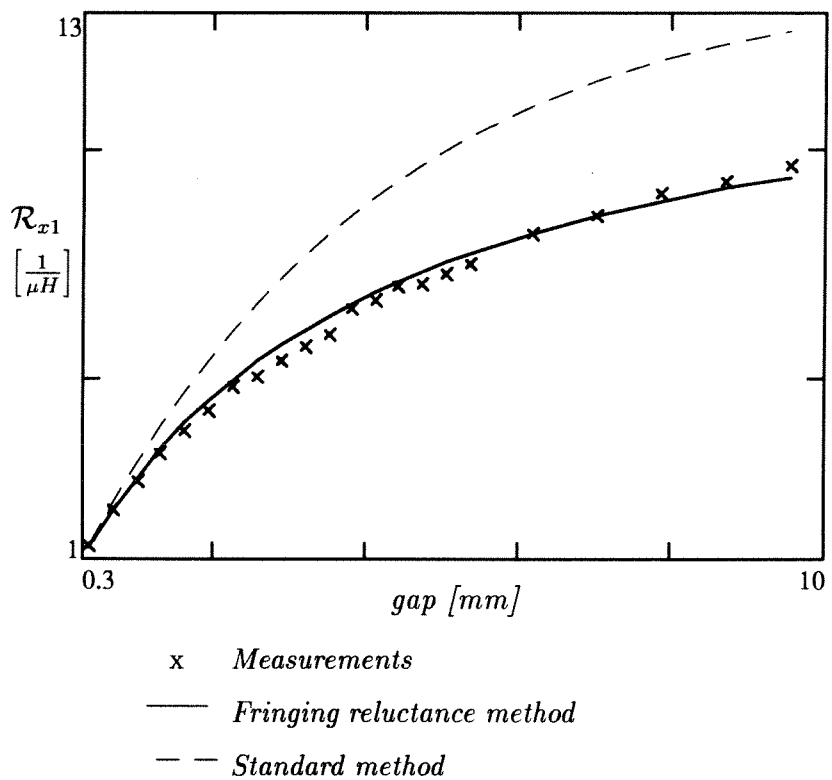

Figure 5.9: Comparison of gap reluctance measurements with predicted values using two different corrections for fringing flux.

Chapter 6

Physical Models

The success of the new reluctance model for UU and UI cores introduced in chapter 5 is attributed to the fact that it faithfully describes physical fluxes in the magnetic structure. In this chapter this approach is generalized.

In section 6.1, the difference between physical models and equivalent models is discussed.

In section 6.2, a procedure to derive "physical reluctance models" for generic gapped magnetic structures is presented.

In the following sections three examples with experimental verification are presented.

6.1 Equivalent Models and Physical Models

The concept of physical models has been introduced by [9] and further discussed by [13]. Given an electrical circuit, for example the "black-box" two-port shown in Fig. 6.1, two different approaches can be taken to describe it.

On one hand, it is possible to develop an *equivalent model* to describe the *external*

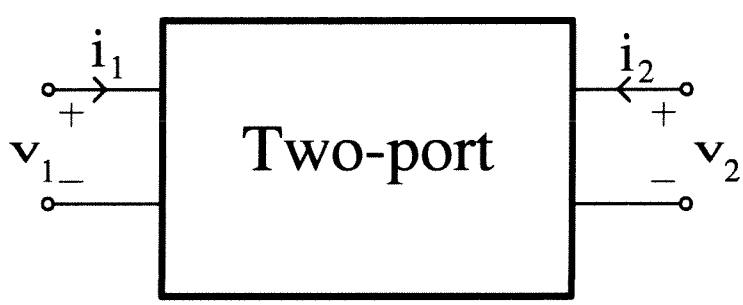

Figure 6.1: A black-box two-port.

behavior of the two-port. This type of model does not try to describe what is actually present inside the black box, but to give a model that behaves in the same way as the black box and is indistiguishable from it on the basis of external measurements.

On the other hand, it is possible to develop a *physical model* that describes what is physically happening *inside* the black box. In a physical model there is a one-to-one correspondence between elements inside the black box and elements in the model. In a magnetic model, for example, there is a reluctance corresponding to each flux path in the physical system. Element values in a physical model can sometimes be calculated as a function of physical quantities inside the black box. For example, a gap reluctance in a magnetic circuit can be calculated as a function of cross-section and gap thickness. This type of model can obviously be much more complicated than an equivalent model.

Equivalent models like Thévenin and Norton equivalents are very useful in the study of electric circuits because they give a simple description from which quantities of interest can be calculated. The limitations of equivalent circuits are twofold.

First of all, in equivalent models there can be elements that do not make sense physically. A well-known example is the class of equivalent transformer circuits shown in Fig. 2.3b, where the transformer ratio a can assume any positive value. It is clear that transformer ratio a can be chosen in such a way to make inductance $L_{11} - aL_M$ negative. A negative inductance does not have a physical meaning, even if the equivalent circuit is still perfectly valid.

The second limitation of equivalent models is that any information on what is present inside the black box of Fig. 6.1 is lost and, therefore, if something is changed inside the black box, it is not clear how that will affect the equivalent model. This limitation was clearly demonstrated in the previous chapter. The old reluctance model of Fig. 5.1 is an equivalent model, whereas the new reluctance model of Fig. 5.3 is a physical model. It was shown that a variation of gap (which is a change inside the black box of Fig. 6.1) affects all reluctances in the old model, but it does not change physical leakage reluctances $\mathcal{R}_l$, $\mathcal{R}_{l1}$ and $\mathcal{R}_{l2}$ in the new model. Therefore, the superiority of the new model lies in the fact that it is a physical model and physically describes the leakage fluxes in air. In the new model there is a one-to-one correspondence between flux paths and reluctances in

the model.

6.2 Procedure to Determine Physical Models

In this section a procedure to find the physical reluctance model for a given magnetic structure is described. The magnetic structure consists of a high-permeability core with air gaps to prevent core saturation. Various windings are wound around the core. In section 5.2 it was shown that the position of gaps with respect to the windings has a significant effect on electrical characteristics of the magnetic structure. A physical reluctance model that accurately describes these effects is desired. The assumption is made that permeability of the magnetic material is infinite. In all reluctance models discussed so far, this assumption was implicitly made since no core reluctance was used.

The procedure to determine the physical reluctance model can be divided in two steps:

1. Main core model. Only flux paths in the core material are considered at this stage. Each winding is modeled by an *mmf* source, and each gap is modeled by a reluctance. Since the core material is assumed to have infinite permeability, the only reluctances present in this model are gap reluctances. Interconnections between model elements are determined as follows: if there is a continuous magnetic path in the core between two elements, they are connected together in the reluctance model.

2. Addition of air reluctances. Air reluctances are added to the main core model to model flux paths that close in air. A brute-force approach is to put leakage reluctances between every couple of nodes in the main core model. Except for extremely simple magnetic structures, this approach leads to models with a big number of air reluctances, many of which have values significantly bigger than air gap reluctances and could be neglected without introducing significant errors. Another problem with this approach is that if the model has too many reluctances, their value cannot be determined from measurements. A much better approach is to use engineering judgment to decide which air flux paths are important and which

ones can be neglected. In case of poor agreement between model and measurements, the model can be refined by adding more air reluctances.

Various examples are given to illustrate the method and discuss some interesting special cases.

6.3 Example 1: UU Core with Side Gaps

The core structure shown in Fig. 6.2a is considered. It is a two-winding UU structure with two side gaps. This structure is different from the ones considered until now due to gap position. The first step in the procedure is to find the main core model, which is shown in Fig. 6.2b. It has two *mmf* sources modeling the two windings and two reluctances modeling the air gaps. The circuit represents the main flux path inside the core and through the air gaps. This is the end of the first step of the procedure.

The second step is the introduction of air reluctances. The main core model has four nodes, A-B-C-D. The brute-force approach of putting an air reluctance between every two nodes would give six reluctances as shown in Fig. 6.3. The two air reluctances $\mathcal{R}_{AB}$ and $\mathcal{R}_{CD}$ in parallel with gap reluctances $\mathcal{R}_{x1}$ and $\mathcal{R}_{x2}$ are the fringing reluctances introduced in section 5.5 to model fringing flux at gaps. As mentioned in that section, fringing reluctances can be neglected in the case of small gaps. As has been done in the previous chapters, fringing reluctances will not be explicitly drawn, but they are considered as a correction to gap reluctance values.

At this point it is a good idea to look at fluxes corresponding to the various air reluctances to decide whether some of them may be neglected. Fluxes corresponding to $\mathcal{R}_{BC}$ and $\mathcal{R}_{AC}$ are shown in Fig. 6.3b. It seems reasonable to say that flux ϕ_{AC} will probably be bigger than ϕ_{BC}. If $\mathcal{R}_{BC}$ (and $\mathcal{R}_{AD}$, by symmetry) are neglected, the resulting reluctance model is shown in Fig. 6.4. This approximation will be experimentally verified in the following.

It is interesting to notice that the two gap reluctances $\mathcal{R}_{x1}$ and $\mathcal{R}_{x2}$ can be lumped together in a single reluctance, and then this reluctance model is identical to the old reluctance model of Fig. 5.1. This model is a physical model for the magnetic structure of Fig. 6.2a, but it is not a physical model for the magnetic structure of Fig. 5.1 due to

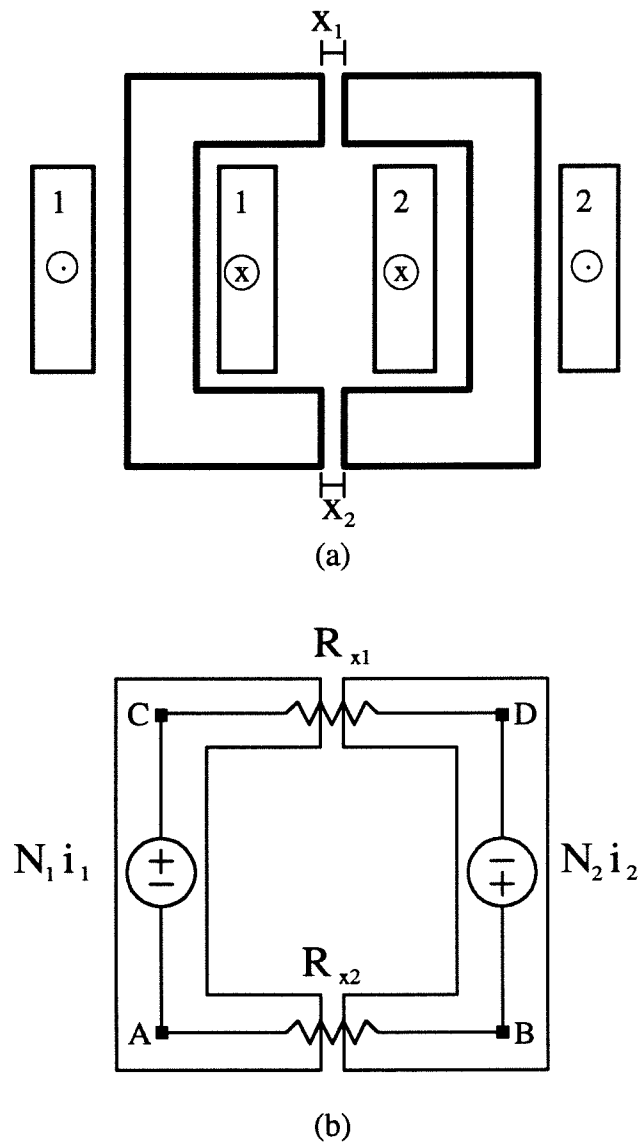

Figure 6.2: Example 1: core structure (a) and its main core model (b).

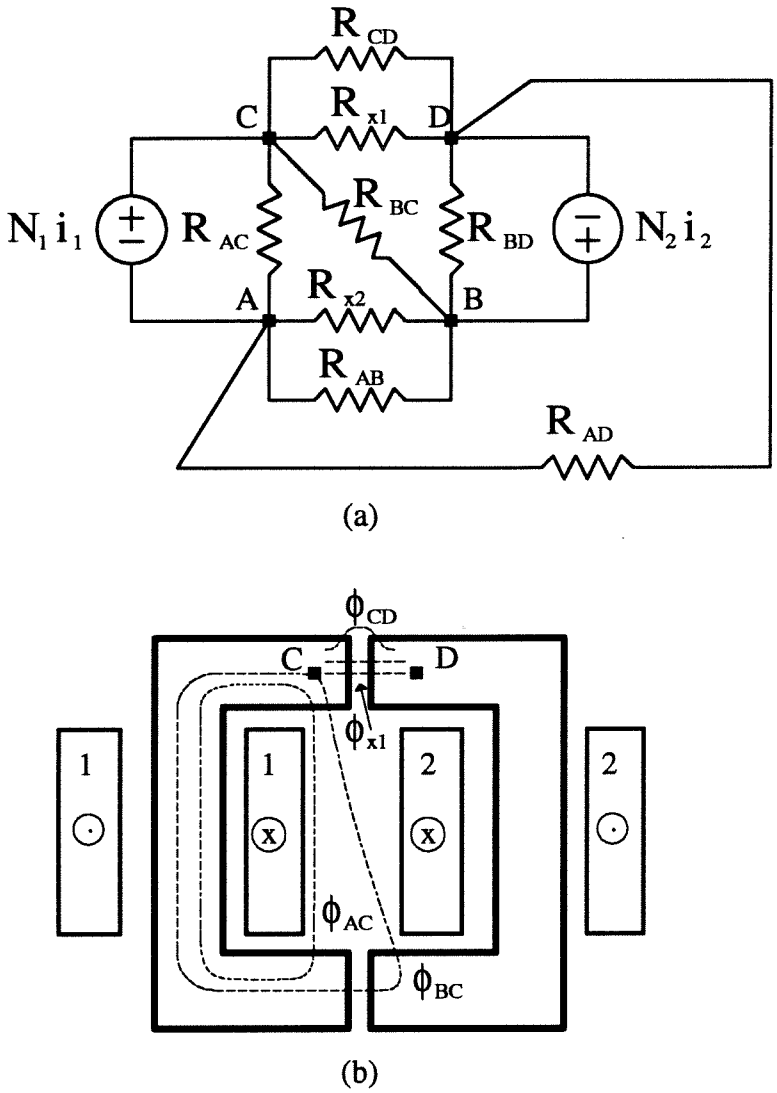

Figure 6.3: Example 1: an air reluctance is added between every two nodes of the main core model (a). Fluxes corresponding to $\mathcal{R}_{AC}$ and $\mathcal{R}_{BC}$ are shown in (b).

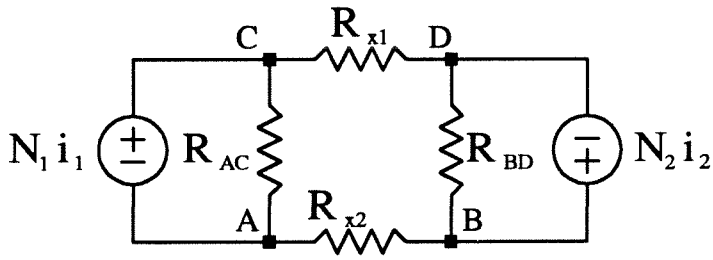

Figure 6.4: Example 1: simplified reluctance model.

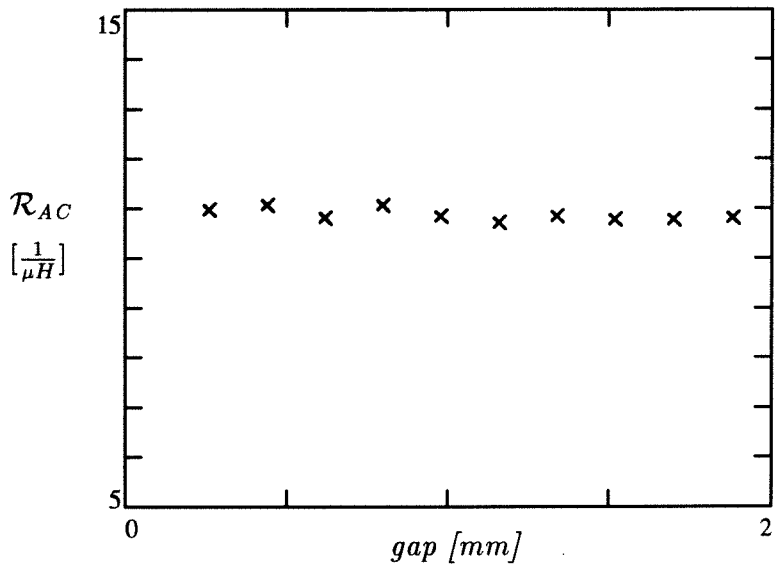

Figure 6.5: Example 1: measured values of air reluctance $\mathcal{R}_{AC}$ as a function of gap. The fact that $\mathcal{R}_{AC}$ is constant verifies the model.

the different gap positions.

Measurements to validate the model are performed on a UU60 core with 26 turns per winding and various values of spacer gap. Since the structure is symmetric, it is $\mathcal{R}_{AC} = \mathcal{R}_{BD}$ and $\mathcal{R}_{x1} = \mathcal{R}_{x2}$. As usual, inductance L_1 and coupling coefficient k_1 are measured. From the model of Fig. 6.4

$$L_1 = \frac{N_1^2}{\mathcal{R}_{AC} \| (2\mathcal{R}_{x1})} \tag{6.1}$$

$$k_1 = \frac{\mathcal{R}_{AC}}{\mathcal{R}_{AC} + 2\mathcal{R}_{x1}} \tag{6.2}$$

From (6.2) an expression for $\mathcal{R}_{x1}$ can be derived and substituted in (6.1). From the resulting expression $\mathcal{R}_{AC}$ can be calculated as

$$\mathcal{R}_{AC} = \frac{N_1^2}{(1 - k_1)L_1} \tag{6.3}$$

Air reluctance $\mathcal{R}_{AC}$ is expected to be approximately independent of gap size. A dependence of $\mathcal{R}_{AC}$ on gap may indicate that the model is not accurate enough and that reluctances $\mathcal{R}_{BC}$ and $\mathcal{R}_{AD}$ cannot be neglected. The plot of $\mathcal{R}_{AC}$ as a function of gap in Fig. 6.5 shows that $\mathcal{R}_{AC}$ is indeed constant and therefore validates the model. Gap

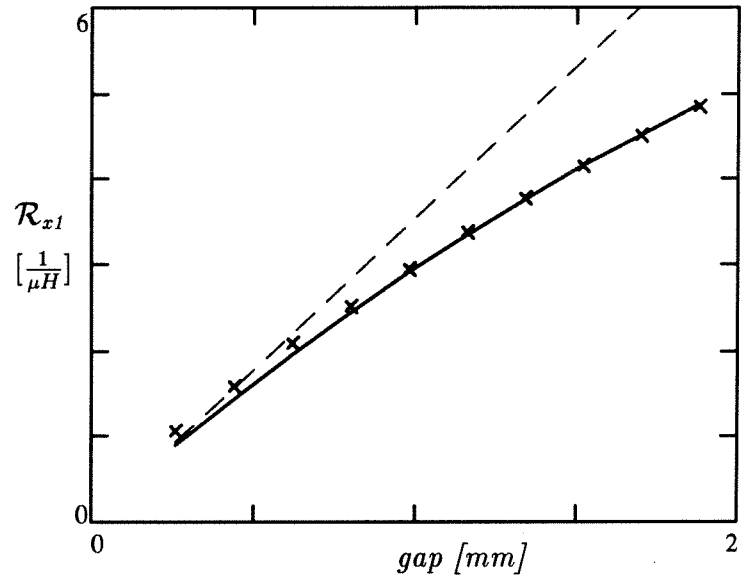

x Measured values of R_{x1}
— — Predictions without correction for fring. flux
—— Predictions with correction for fring. flux

Figure 6.6: Example 1: gap reluctance $\mathcal{R}_{x1}$ as a function of gap. Introducing a correction for fringing flux ($\mathcal{R}_{fring}$=18 [1/μH]) improves predictions.

reluctance $\mathcal{R}_{x1}$ is calculated from (6.2) and plotted in Fig. 6.6. In the absence of fringing flux, gap reluctance is

$$\mathcal{R}_{x1} = \frac{x_1}{\mu_0 S} \tag{6.4}$$

and it increases linearly with gap. The experimental data show that $\mathcal{R}_{x1}$ increases less than linearly with gap due to fringing flux. A very good fit can be obtained if a fringing reluctance $\mathcal{R}_{fring}$ = 18 [$1/\mu H$] is put in parallel with the ideal gap reluctance given by (6.4). As explained above, fringing reluctance $\mathcal{R}_{fring}$ is represented by reluctances $\mathcal{R}_{AB}$ and $\mathcal{R}_{CD}$ in Fig. 6.3.

6.4 Example 2: UU Core with Windings Overlapping the Gaps

A UU60 core with spacer gap and windings overlapping the gaps as shown in Fig. 6.7 is considered. In this case the main core model is not obvious because the windings cover the gaps and, therefore, the relative position of the *mmf* source modeling the winding and of the reluctance modeling the gap is unclear. A method to solve this problem is to break

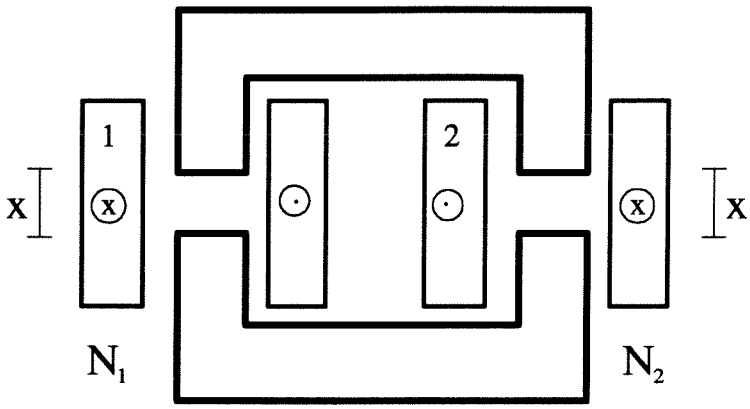

Figure 6.7: Example 2: core structure.

up the winding in two parts at the position where the gap is, as shown in Fig. 6.8. The advantage of this method is that the main core model preserves the physical structure of the magnetic core. This is important for the second step when air reluctances are added. For example, if the two voltage sources $N_1 i_1/2$ were lumped together as an $N_1 i_1$ voltage source between nodes B and C, a node would disappear from the model because nodes A and F would coincide (capital letters refer to Fig. 6.8b).

At this point air reluctances can be added. Since in the main core model there are six nodes, which means a maximum of 15 air reluctances, it is important to limit the number of air reluctances introduced. First of all, it seems reasonable to neglect flux paths from the left leg to the right leg, i.e., reluctances between nodes A-B and nodes D-E. Therefore, reluctances $\mathcal{R}_{AD}$, $\mathcal{R}_{AE}$, $\mathcal{R}_{BD}$ and $\mathcal{R}_{BE}$ are neglected.

Of the remaining air fluxes, the most important one is ϕ_l of Fig. 6.8a, which is flux between the bars of high-permeability material α-β and γ-δ. This flux is modeled by reluctance $\mathcal{R}_{CF}$. The remaining air reluctances model air flux in the regions close to the two windings. Given the symmetry between the two legs, attention is focused on leg 1. There are five possible air reluctances as shown in Fig. 6.9a. In general, all these reluctances will be rather large because the copper winding acts as a shield and limits the air fluxes represented by these reluctances. Since $\mathcal{R}_{x1}$ is surely much smaller than all these reluctances, a small error is committed if one of these reluctances is moved across

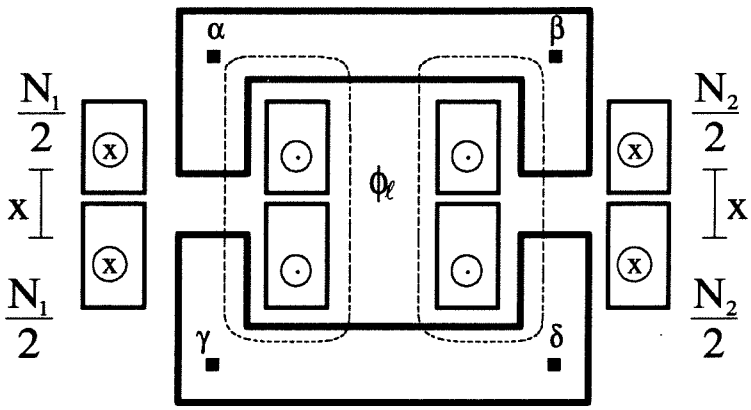

(a)

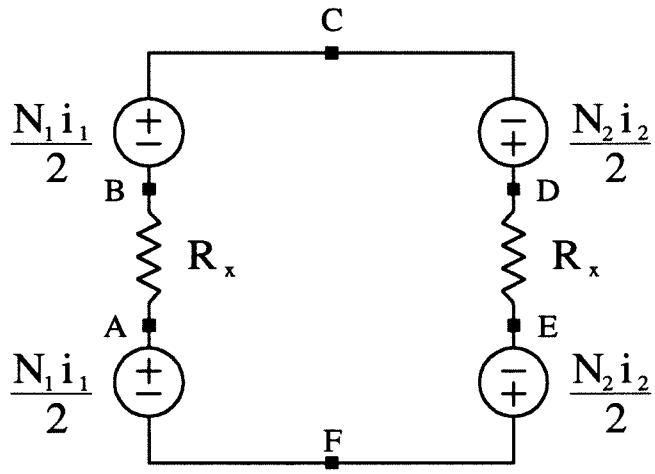

(b)

Figure 6.8: Example 2: windings are broken in two parts (a) to give unambiguous main core model (b).

$\mathcal{R}_{x1}$. For example, reluctance $\mathcal{R}_{BF}$ can be moved across $\mathcal{R}_{x1}$ so that it appears directly in parallel with $\mathcal{R}_{AF}$. The same can be done with $\mathcal{R}_{AC}$. This is shown in Fig. 6.9b. By symmetry it is $\mathcal{R}_{AC}\|\mathcal{R}_{BC} = \mathcal{R}_{AF}\|\mathcal{R}_{BF}$ and, therefore, the two voltage sources can be combined together as shown in Fig. 6.9c. Air reluctance $2(\mathcal{R}_{AC}\|\mathcal{R}_{BC})$ appears directly in parallel with voltage source $N_1 i_1$. Reluctance $\mathcal{R}_{AB}$ is the gap fringing reluctance and, as usual, it is merged with $\mathcal{R}_{x1}$. The final reluctance model with a simplified notation for reluctances is shown in Fig. 6.10, which is identical to the new model for UI cores introduced in section 5.3.

To validate the model measurements are performed on a UU60 core with 160 turns per winding. As mentioned above, $\mathcal{R}_{l1}$ and $\mathcal{R}_{l2}$ are expected to be rather large. Therefore, it seems legitimate to neglect them in a first attempt to model this magnetic structure. The resulting model is identical to the simplified new model of section 5.4.1, and it has only a single leakage reluctance $\mathcal{R}_l$. Values of this reluctance as a function of gap as obtained from the measurements are shown in Fig. 6.11. This reluctance is approximately constant, thereby validating the model. Gap reluctance $\mathcal{R}_{x1}$ is also calculated from the measurements and, as in Example 1, a correction for fringing reluctance is introduced ($\mathcal{R}_{fring} = 20\ [1/\mu H]$). Comparison of predictions and measurements is shown in Fig. 6.12.

6.5 Example 3: UU Core with Two Side-by-Side Windings on the Same Leg

As a last example, the UU60 core structure with spacer gap and two windings shown in Fig. 6.13a is considered. In this case the two windings are on the same leg in a side-by-side arrangement. In order to maximize the leakage flux, an empty space is left between the two windings. In any case, the leakage is expected to be smaller than in the case of Example 2, where the two windings were on different core legs.

The main core model is shown in Fig. 6.13b. Important air flux paths are shown in Fig. 6.13a. Notice that fluxes ϕ_{l1} and ϕ_{l2} are leakage fluxes of winding 1 and 2 respectively, whereas flux ϕ_l represents mutual flux that closes in the air. These fluxes are modeled by reluctances $\mathcal{R}_{l1}$, $\mathcal{R}_{l2}$ and $\mathcal{R}_l$ in the complete reluctance model of Fig. 6.14.

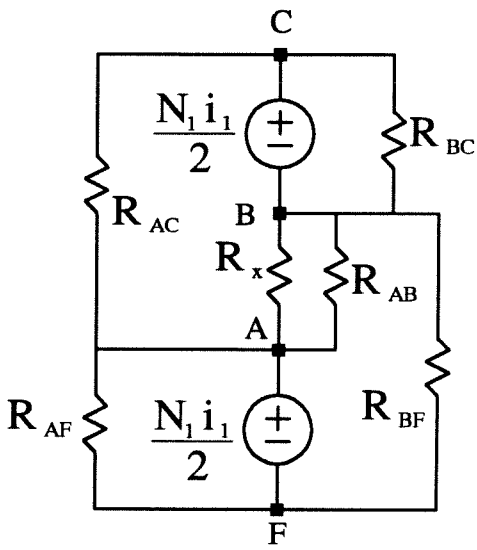

(a)

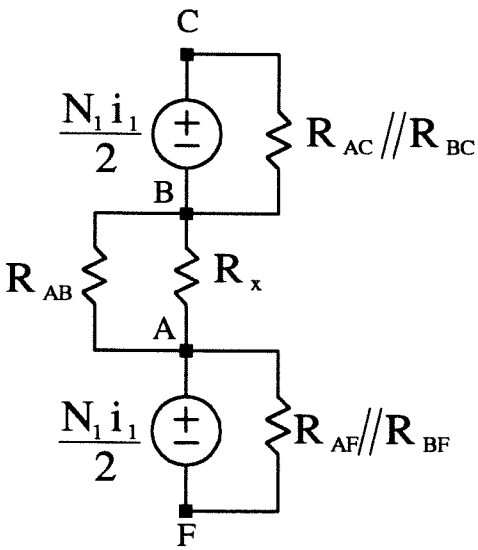

(b)

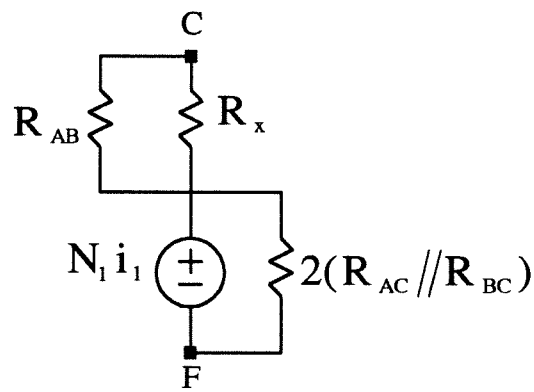

(c)

Figure 6.9: Example 2: complete reluctance model for a core leg (a) and successive simplifications (b)-(c).

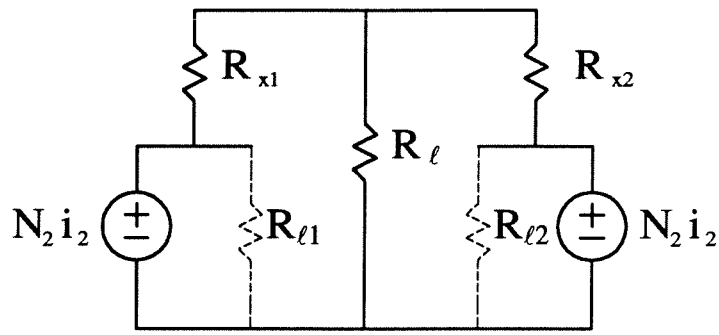

Figure 6.10: Example 2: final reluctance model. Measurements will show that reluctances $\mathcal{R}_{l1}$ and $\mathcal{R}_{l2}$ may be neglected.

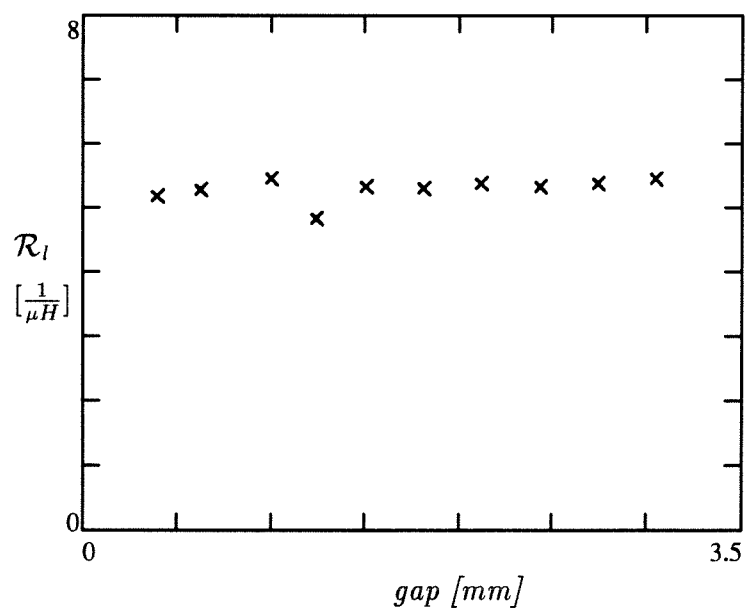

Figure 6.11: Example 2: leakage reluctance $\mathcal{R}_l$ as a function of gap. The fact that $\mathcal{R}_l$ is approximately constant justifies the approximation of neglecting $\mathcal{R}_{l1}$ and $\mathcal{R}_{l2}$.

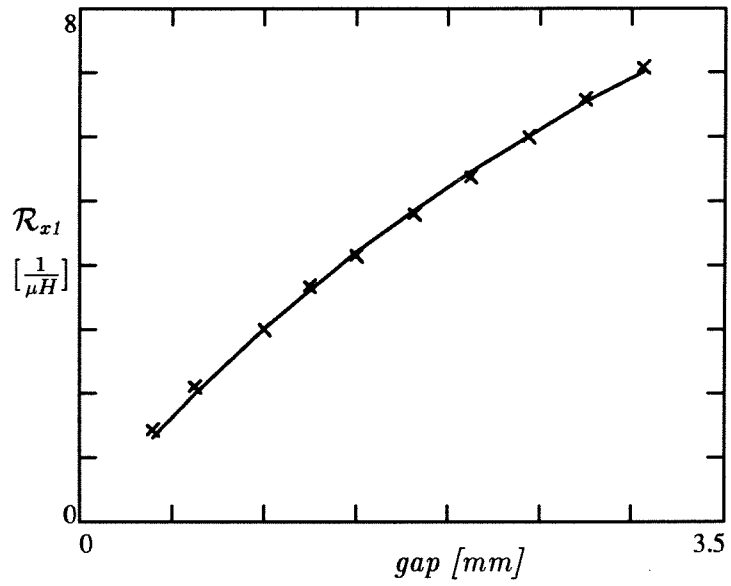

Figure 6.12: Example 2: comparison of measurements and predictions for $\mathcal{R}_{x1}$ as a function of gap.

Given the symmetry of the system, reluctances $\mathcal{R}_{l1}$ and $\mathcal{R}_{l2}$ are equal.

Measurements are performed for different values of spacer gap. From these measurements leakage reluctance $\mathcal{R}_{l1}$ is calculated as shown in Fig. 6.15 and it is indeed approximately constant. It should be evident from Fig. 6.14 that it is *not* possible to distinguish between reluctances $\mathcal{R}_{x1}$, $\mathcal{R}_{x2}$ and $\mathcal{R}_l$. All that can be measured is the total reluctance in series with the two *mmf* sources, that is reluctance $\mathcal{R}_{series} = \mathcal{R}_{x1} + \mathcal{R}_{x2} \| \mathcal{R}_l$. A possibility to check the measured value of this reluctance comes from Example 2 in which the same core was used and reluctance $\mathcal{R}_l$ was found to be $\mathcal{R}_l = 6\ [1/\mu H]$. Using also the value of fringing reluctance found in Example 2 ($\mathcal{R}_{fring} = 20\ [1/\mu H]$) and knowing gap thickness, it is possible to estimate reluctance $\mathcal{R}_{series}$. The comparison of measurements and predictions in Fig. 6.16 shows a reasonably good agreement. The fact that values of $\mathcal{R}_l$ obtained from a different set of measurements with a different type of windings could be succesfully used shows that air reluctances are approximately constant for a given core geometry.

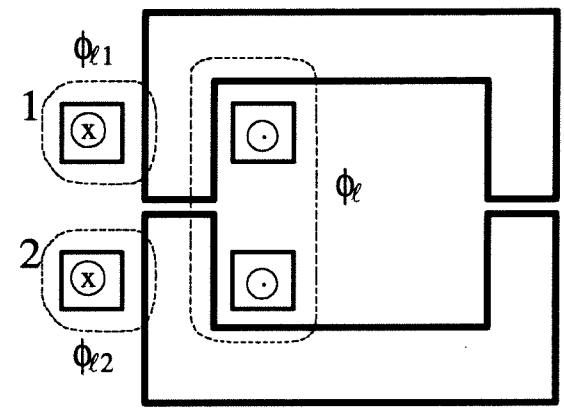

(a)

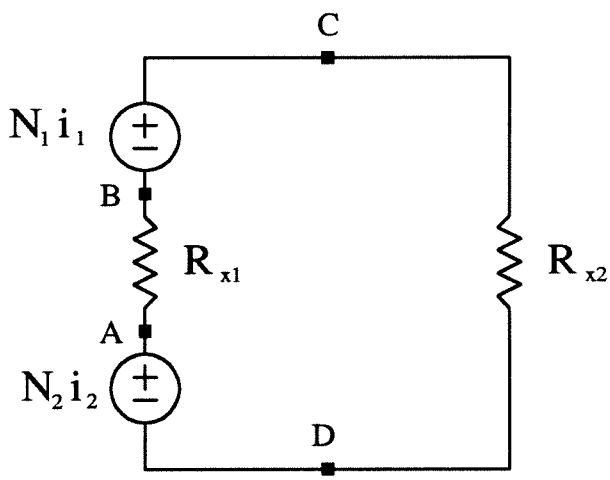

(b)

Figure 6.13: Example 3: core structure (a) and its main core model (b).

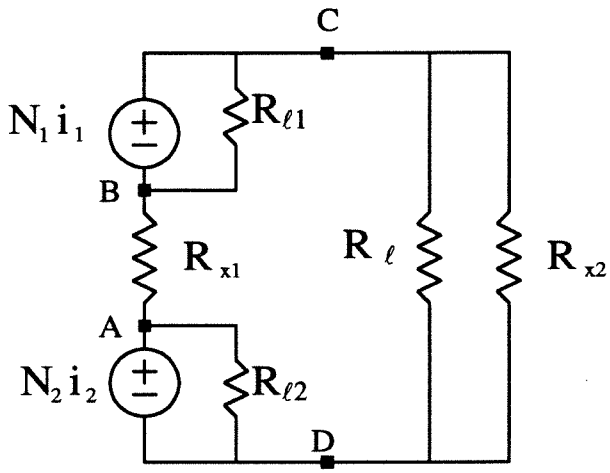

Figure 6.14: Example 3: complete reluctance model.

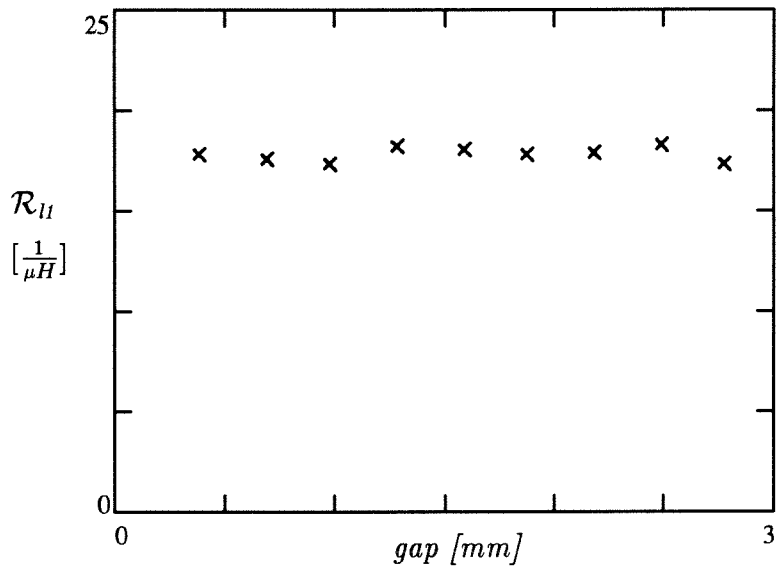

Figure 6.15: Example 3: leakage reluctance $\mathcal{R}_l$ is approximately constant as expected.

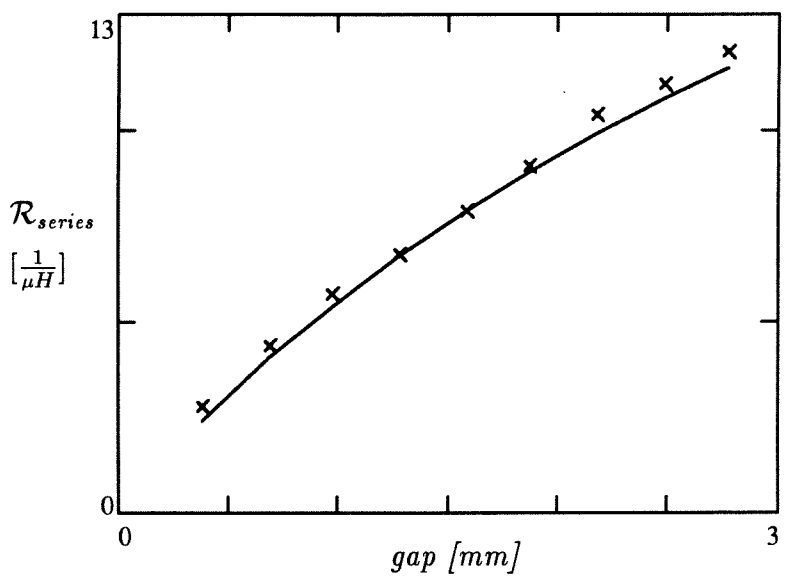

Figure 6.16: Example 3: reluctance $\mathcal{R}_{x1} + \mathcal{R}_{x2} \| \mathcal{R}_l$ as a function of gap: comparison of measurements and predictions.

Chapter 7

Multiple Winding Structures

In certain switching converter topologies there are more than two inductors that have proportional voltage waveforms when the converter operates in steady state. Typical examples are multiple-output forward converter and isolated Ćuk converter [4]. All these inductors can be coupled together and zero current ripple can be achieved in all but one of them. For example, in the case of an isolated Ćuk converter, all ripple can be steered into the isolation transformer, so that input and output inductor have approximately constant current.

In the first section, the zero ripple condition is generalized to multiple-winding structures.

In the second section, commonly used multiple-winding structures are considered and their physical reluctance models are established using the procedure of section 6.2 and experimentally verified.

7.1 Generalization of Zero Ripple Condition to Multiple Winding Structures

In this section a procedure to find the zero ripple condition for a generic multi-winding structure is briefly described.

First of all, a definition is needed. In section 2.1.3 coupling coefficients k_1 and k_2 for a two-winding structure were defined (a slightly different notation is used here) as

$$k_1 = \left.\frac{\phi_2}{\phi_1}\right|_{i_2=0} \qquad k_2 = \left.\frac{\phi_1}{\phi_2}\right|_{i_1=0} \tag{7.1}$$

where ϕ_i is the flux linking the i-th winding. Coupling coefficient k_1, for example, is the ratio of coupled flux to total flux with the secondary winding open ($i_2 = 0$). This

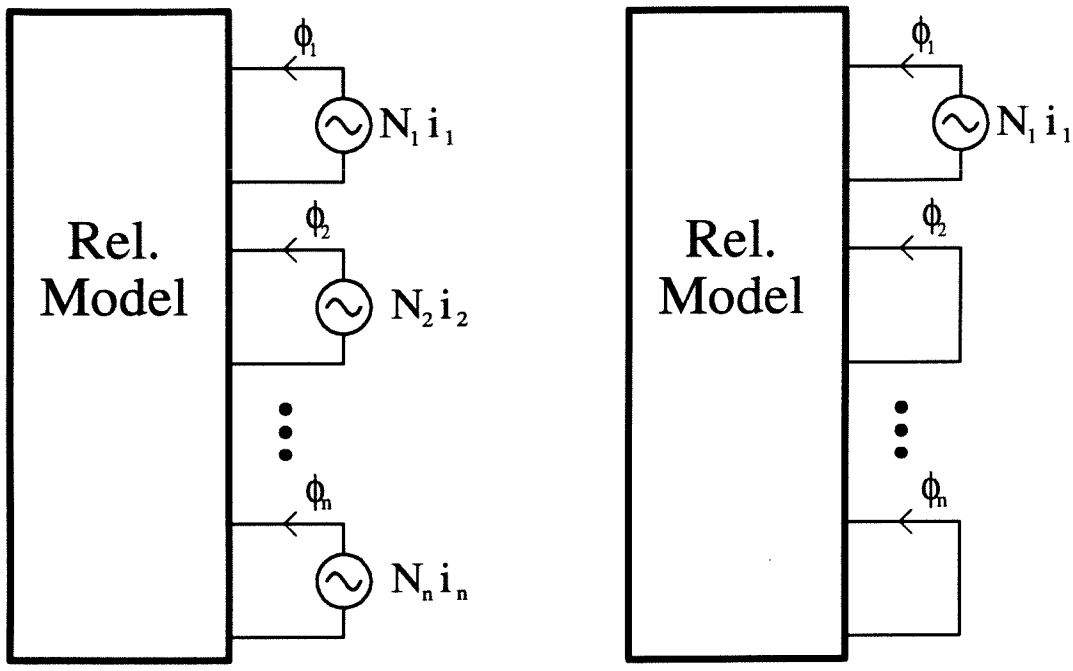

Figure 7.1: Black-box reluctance model for an n-winding structure (a). Zero current ripple condition is applied to all windings except the first one by shorting the mmf sources (b).

definition can be generalized to the n-winding case. For each winding $n-1$ coupling coefficients with respect to the remaining windings can be defined. For example, the coupling coefficients for winding 1 are

$$k_{1j} = \left.\frac{\phi_j}{\phi_1}\right|_{i_2=i_3=\cdots=i_n=0} \tag{7.2}$$

where ϕ_j is the flux linking the j-th winding.

The zero ripple condition is now derived for a multi-winding structure with n windings. The special case of identical voltages applied to all windings is considered. The case of proportional voltages can be reduced to this case by voltage scaling using the winding turns ratio. The multi-winding structure is assumed to have n windings and ripple is steered into winding 1. The starting point of the procedure is a reluctance model of the magnetic structure, which is represented by the generic n-port in Fig. 7.1a. Zero ripple conditions $i_j = 0$, $j = 2...n$, are imposed as shown in Fig. 7.1b by shorting the

corresponding *mmf* sources.

Faraday's law applied to the k-th winding gives

$$\phi_k = \frac{1}{N_k} \int v_k \, dt \tag{7.3}$$

Substituting (7.3) into (7.2) gives

$$k_{1j} = \frac{\frac{1}{N_j} \int v_j dt}{\frac{1}{N_1} \int v_1 dt} \tag{7.4}$$

The condition of identical voltages on all windings gives

$$k_{1j} = \frac{N_1}{N_j} \qquad j = 2...n \tag{7.5}$$

If the $n-1$ conditions (7.5) are satisfied, all ripple is steered into winding 1.

It is important to realize that all $n-1$ equations (7.5) must be satisfied for zero ripple. If one of these conditions is not satisfied, in general all windings will have some ripple. For example, if the zero ripple condition is not satisfied for winding 2, then the *mmf* source $N_2 i_2$ cannot be set to zero as in Fig. 7.1b. Since the zero ripple conditions are derived under the assumption that all *mmf* sources but one are zero, they are not valid any more and in general all windings will have some ripple.

7.2 Reluctance Models for Multiple-Winding Structures

In section 6.2 a procedure to determine the reluctance model of a gapped magnetic structure was given. The procedure was applied to three different two-winding core structures and the resulting reluctance models were experimentally verified. In this section three more examples are given, all of them three-winding structures. These examples cover the most common practical cases.

As explained in chapter 4, high-leakage magnetic structures are desirable for zero-ripple applications, because leakage inductance reduces the sensitivity of the zero-ripple condition to nonidealities. For this reason, in the structures described in the previous chapters, windings are placed on different core legs.

In Example 4 the natural extension of this approach, a three-legged structure with a winding on each leg, is considered. Standard cores like EE and EI cores can be used.

Sometimes it is desirable to put more than one winding on a core leg, especially if there are many windings and it becomes impractical to use a core with so many legs. Since loose coupling is desirable, windings should be physically placed as far as possible. Two different winding arrangements are considered.

In Example 5 a UU core is used with one winding on a leg and the other two windings on the other leg in a top-bottom arrangement.

In Example 6 the same UU core is used but the two windings on the same leg are in a side-by-side arrangement.

Experimental verification of the reluctance models is provided by plotting predicted and measured values of inductances and coupling coefficients as a function of gap thickness. In the previous chapter experimental verification was done in a different way: reluctances in the model were calculated from measurements and the verification was done as follows for gap reluctances and for air reluctances. Gap reluctances were compared with predicted values based on gap thickness and corrected for fringing flux. Air reluctances were plotted as a function of gap thickness to show that they are approximately constant as expected. These verifications ensured good agreement between model and measurements because the number of degrees of freedom in the model was the same as the number of independent measurements in the magnetic structure. All examples in the previous chapter were symmetric two-winding structures, which allow two independent measurements, and the reluctance models had two degrees of freedom, an air reluctance and a gap reluctance. In the examples in this chapter the number of degrees of freedom in the model is usually smaller than the number of independent measurements in the magnetic structure. A generic three-winding structure can be described by the equations

$$\begin{vmatrix} v_1 \\ v_2 \\ v_3 \end{vmatrix} = \begin{vmatrix} L_{11} & L_{12} & L_{13} \\ L_{12} & L_{22} & L_{23} \\ L_{13} & L_{23} & L_{33} \end{vmatrix} \begin{vmatrix} \frac{di_1}{dt} \\ \frac{di_2}{dt} \\ \frac{di_3}{dt} \end{vmatrix}$$

Since the inductance matrix is symmetric, the structure has six degrees of freedom. In some cases considerations of symmetry allow the number of independent parameters to be reduced even more. For example, in the case of the EE core of Example 4, there is a symmetry between the two outer legs. If the windings on these legs are called winding 2

and 3, then

$$L_{12} = L_{13} \qquad L_{22} = L_{33}$$

and therefore the structure has only four degrees of freedom. In the reluctance model for this structure, there are only two unknowns (assuming the gap thickness is known): leakage reluctance $\mathcal{R}_l$ and fringing reluctance $\mathcal{R}_{fring}$. As usual, gap reluctances are calculated from gap thickness, leg cross-section and fringing reluctance.

The two unknowns in the model can be determined from two of the four independent measurements, but there is no guarantee that the model will correctly predict the values of the other two independent measurements. For this reason, model verification in this chapter is done by comparing measured quantities with their predicted values from the model using constant values for reluctances $\mathcal{R}_l$ and $\mathcal{R}_{fring}$.

7.2.1 Example 4: EE Core with a Winding on Each Leg

The EE core with a winding on each leg and spacer gap is shown in Fig. 7.2. The main core model is shown in Fig. 7.3a. As discussed in Example 2 of the previous chapter, very little leakage flux can leak through the winding as flux ϕ of Fig. 7.2 does. If this type of leakage flux is neglected, the only other possible leakage flux path is of the type of flux ϕ_l. This flux path corresponds to a leakage reluctance between nodes A and B in the main core model. The complete reluctance model is shown in Fig. 7.3b. Notice the simplicity of this model that has only one leakage reluctance $\mathcal{R}_l$.

Measurements were performed on an EE60 core with 120 turns per winding. Leakage reluctance and fringing reluctance (the same value of fringing reluctance is used for all gaps for simplicity) are found to be $\mathcal{R}_l = 6\ [1/\mu H]$ and $\mathcal{R}_{fring} = 17.5\ [1/\mu H]$. Comparison of measured and predicted values of inductances and coupling coefficients are shown in Fig. 7.4. The agreement between calculated and measured values is very good.

7.2.2 Example 5: UU Core with Top-Bottom Winding Arrangement

The structure under consideration is a spacer-gapped UU core with a winding on one leg and two windings on the other leg in a top-bottom arrangement as shown in Fig. 7.5.

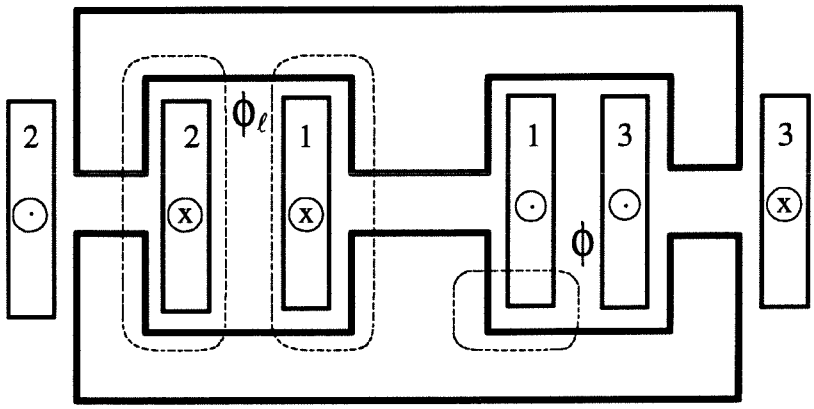

Figure 7.2: Example 4: spacer-gapped EE core with a winding on each leg.

A paper spacer is inserted between winding 2 and winding 3 to increase leakage.

The main core model is shown in Fig. 7.6a. Different types of leakage flux are shown in Fig. 7.5. It is interesting to notice that the path of leakage flux ϕ_{l2} is partially inside the core and it crosses the leg air gap. Therefore, the corresponding leakage reluctance $\mathcal{R}_{l2}$ is in parallel with the series combination of *mmf* source $N_2 i_2$ and gap reluctance $\mathcal{R}_{x2}$ (nodes A and C) and not directly in parallel with the *mmf* source (nodes B and C). Another interesting observation is that flux ϕ_{l3} is completely in air and therefore the corresponding reluctance $\mathcal{R}_{l3}$ is expected to be rather big.

The complete reluctance model is shown in Fig. 7.6b. Notice that if winding 3 is left open, i.e., *mmf* source $N_3 i_3$ is shorted, the model becomes identical to the model of Example 2 in the previous chapter with $\mathcal{R}_l|_{Ex.2} = \mathcal{R}_l \| \mathcal{R}_{l2}$. This is hardly surprising since the magnetic structure of this example becomes identical to the one of Example 2 if winding 3 is removed. Since a spacer gap is used, gap reluctance $\mathcal{R}_{x1}$ is equal to $\mathcal{R}_{x2}$ and the model with winding 3 removed is symmetric. Therefore, it is expected that $L_1 = L_2$ and $k_{12} = k_{21}$. Measurements performed on a UU60 core with 60 turns per winding showed that this is indeed the case.

From the measurements it was found $\mathcal{R}_l = 5.6\ [1/\mu H]$, $\mathcal{R}_{l2} = 60\ [1/\mu H]$, $\mathcal{R}_{l3} = 190\ [1/\mu H]$ and $\mathcal{R}_{fring} = 25\ [1/\mu H]$. Notice that as expected $\mathcal{R}_{l3} \gg \mathcal{R}_l, \mathcal{R}_{l2}$. Therefore, $\mathcal{R}_{l3}$ could be neglected without introducing significant errors. Comparison of measured and predicted values of inductances and coupling coefficients is shown in Fig. 7.7.

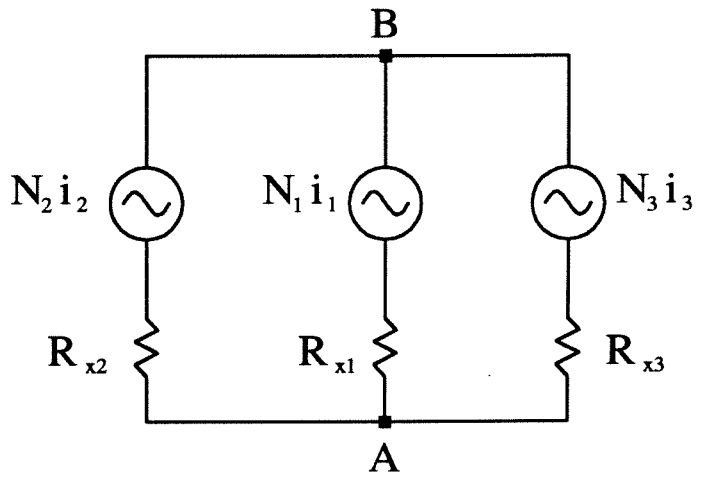

(a)

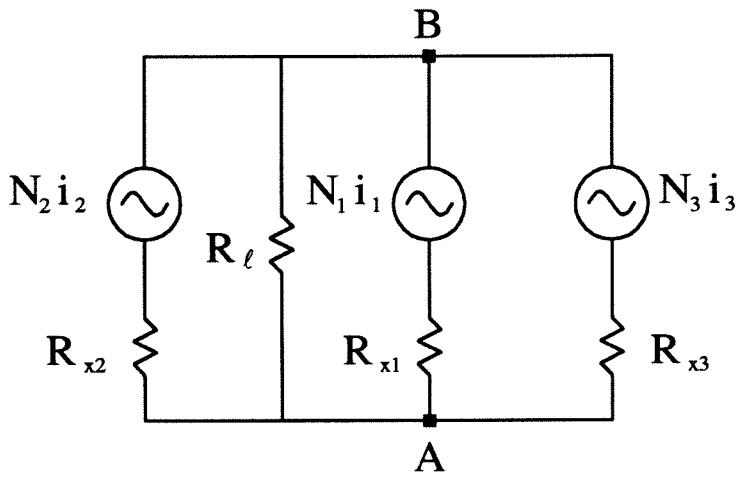

(b)

Figure 7.3: Example 4: main core model (a) and complete reluctance model (b).

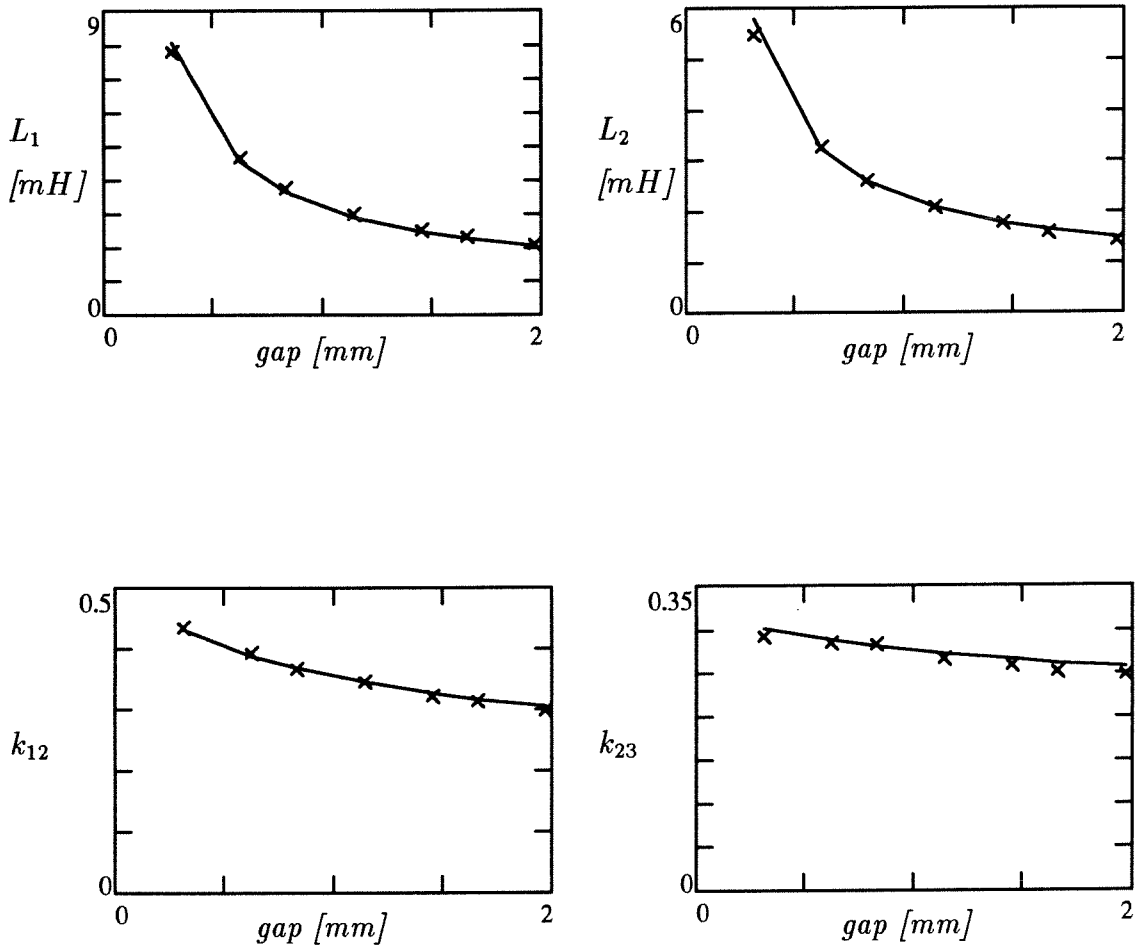

Figure 7.4: Example 4: comparison of measured and predicted values of inductances L_1, L_2 and coupling coefficients k_{12}, k_{23}.

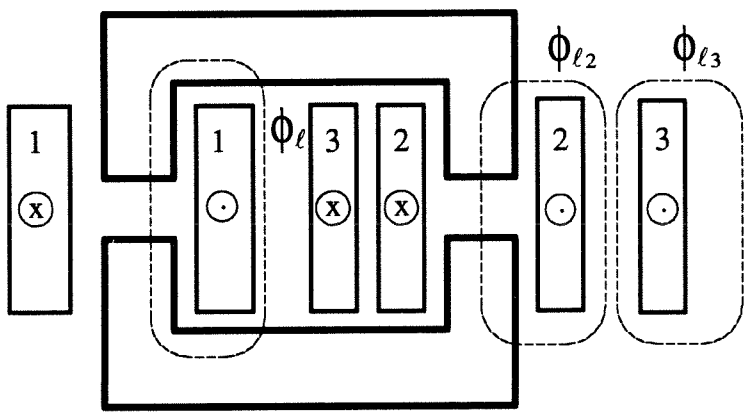

Figure 7.5: Example 5: spacer-gapped UU core with two windings on the same leg in a top-bottom arrangement.

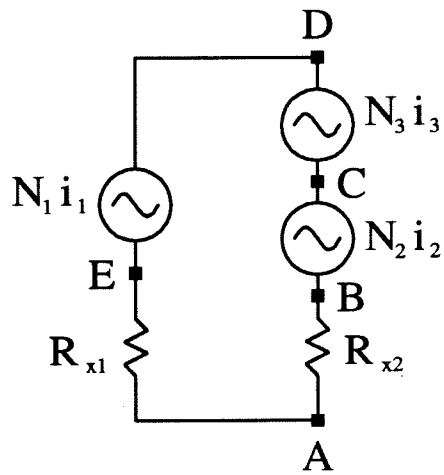

(a)

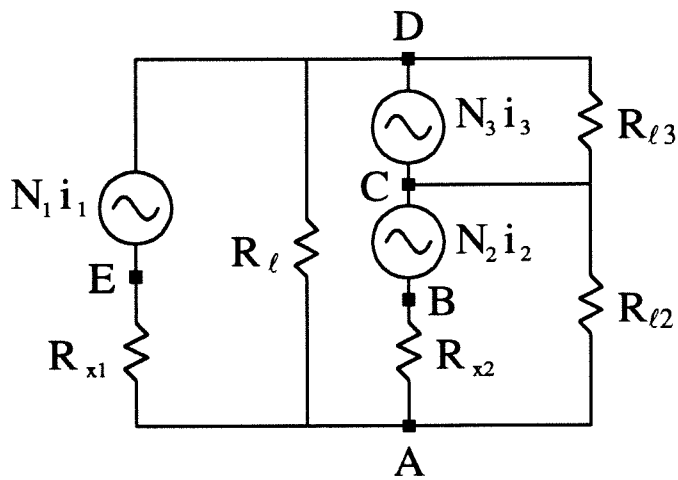

(b)

Figure 7.6: Example 5: main core model (a) and complete reluctance model (b).

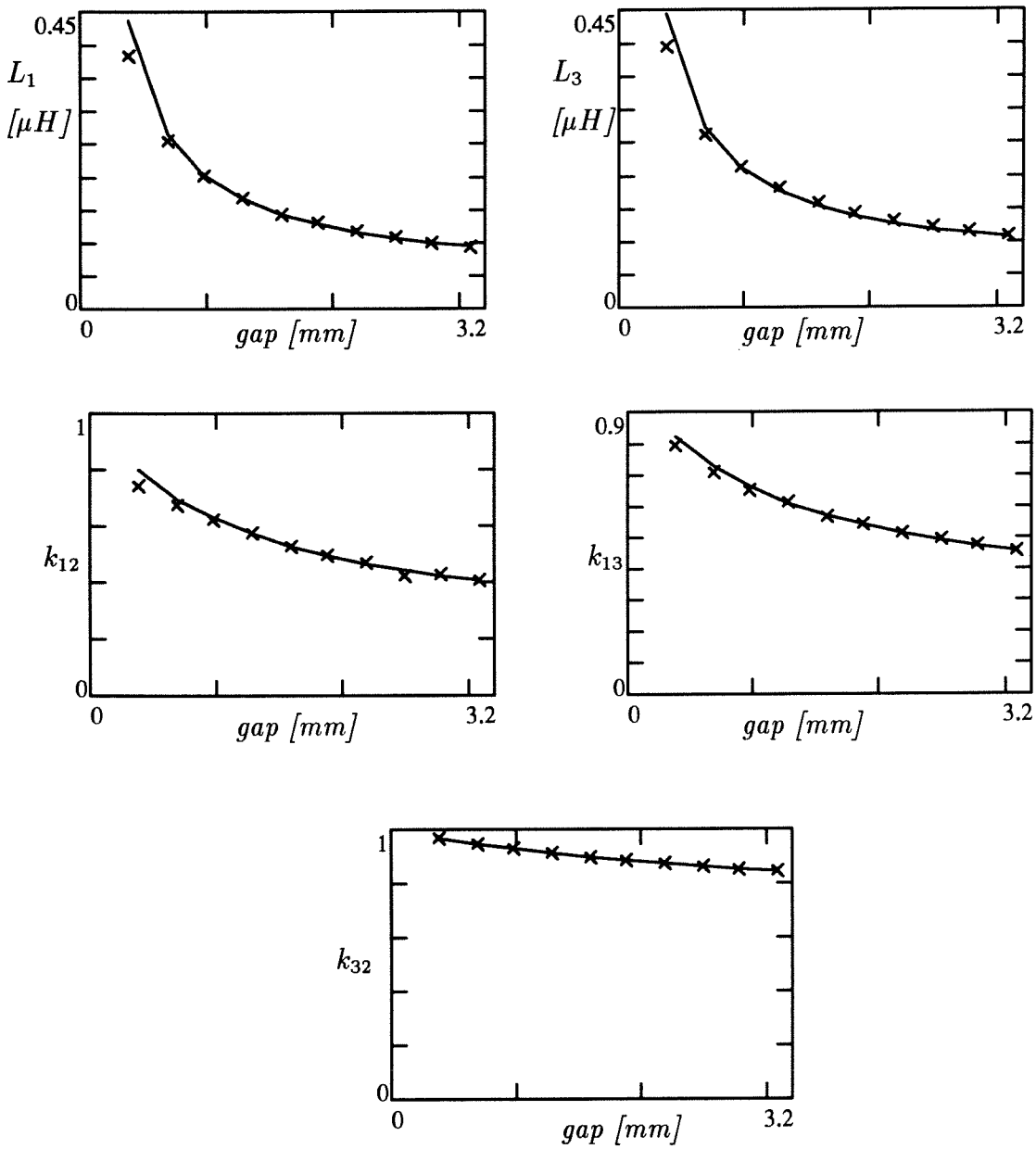

Figure 7.7: Example 5: comparison of measured and predicted values of inductances L_1, L_3 and coupling coefficients k_{12}, k_{23} and k_{32}.

7.2.3 Example 6: UU Core with Side-by-Side Winding Arrangement

The structure under consideration, a spacer-gapped UU core with a winding on one leg and two windings on the other leg in a side-by-side arrangement, is shown in Fig. 7.8. In this case we will see that the reluctance model obtained following the usual procedure with the usual approximations is not very accurate and a refinement is necessary. An improved model with an additional leakage reluctance gives good agreement with measurements.

The main core model is shown in Fig. 7.9a. Different types of leakage flux in air are shown in Fig. 7.8. The complete reluctance model is shown in Fig. 7.9b.

Given the symmetry of the core structure, it is $\mathcal{R}_{x1} = \mathcal{R}_{x2}$ and $\mathcal{R}_{l2} = \mathcal{R}_{l3}$. Notice also that from this reluctance model it follows that

$$k_{21} = k_{12}k_{23} \tag{7.6}$$

This is true because $\mathcal{R}_{x1} = \mathcal{R}_{x2}$ and

$$\begin{aligned} k_{12} &= \frac{\mathcal{R}_l}{\mathcal{R}_l + \mathcal{R}_{x2}} \\ k_{23} &= \frac{\mathcal{R}_{l2}}{\mathcal{R}_{l2} + \mathcal{R}_{x2} + \mathcal{R}_{x1} \| \mathcal{R}_l} \\ k_{21} &= \frac{\mathcal{R}_l}{\mathcal{R}_l + \mathcal{R}_{x1}} \frac{\mathcal{R}_{l2}}{\mathcal{R}_{l2} + \mathcal{R}_{x2} + \mathcal{R}_{x1} \| \mathcal{R}_l} \end{aligned}$$

If measured data do not satisfy equation (7.6), then predictions from the model of Fig. 7.9b will be wrong regardless of the reluctance values used.

Measurements were performed on a UU60 core with 50 turns per winding. Fig. 7.10 shows a plot of quantity $k_{21}/(k_{12}k_{23})$, which the model predicts to be unity (equation (7.6)). Measured values are as much as 30% off. Using the reluctance model of Fig. 7.9b would therefore give at least a 30% error. A way to improve the model is to add a reluctance $\mathcal{R}_{l1}$ in parallel with *mmf* source $N_1 i_1$ as shown in Fig. 7.11. Calculated values of reluctances in this model are $\mathcal{R}_l = 8\ [1/\mu H]$, $\mathcal{R}_{l1} = 51\ [1/\mu H]$, $\mathcal{R}_{l2} = 17.5\ [1/\mu H]$ and $\mathcal{R}_{fring} = 36\ [1/\mu H]$. Comparison of measurements and predictions is shown in Fig. 7.12.

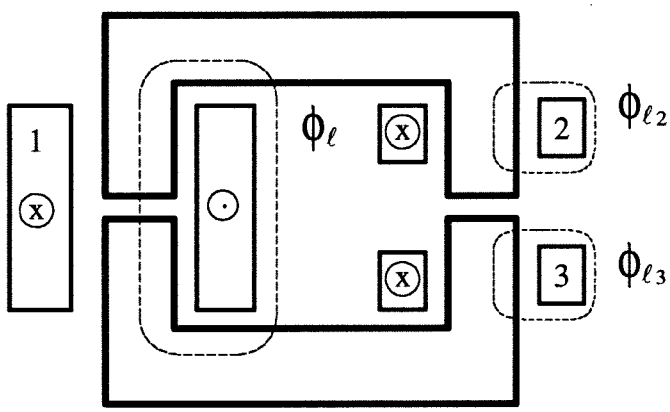

Figure 7.8: Example 6: spacer-gapped UU core with two windings on the same leg in a side-by-side arrangement.

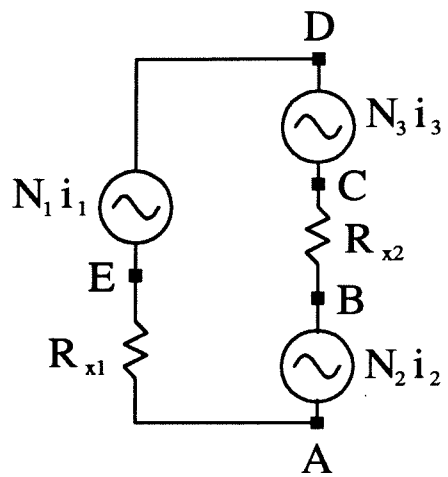

(a)

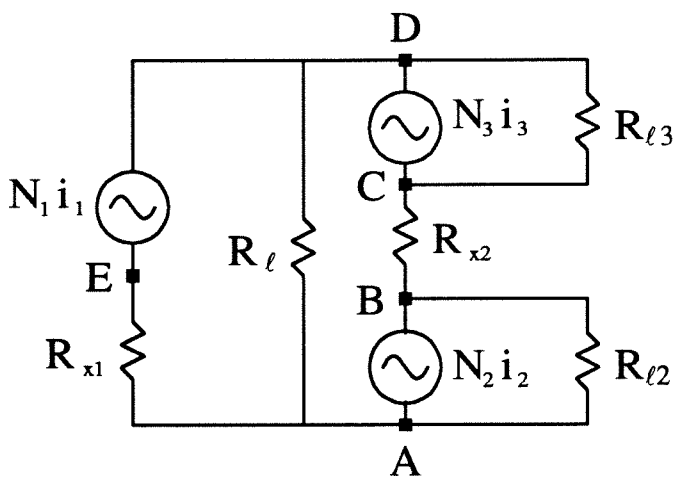

(b)

Figure 7.9: Example 6: main core model (a) and complete reluctance model (b).

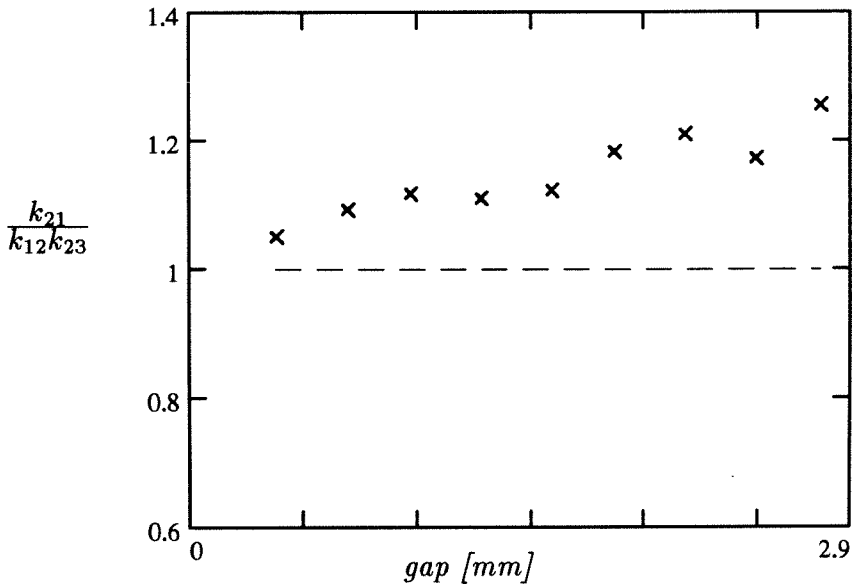

Figure 7.10: Example 6: the reluctance model of Fig. 7.9 predicts $k_{21} = k_{12}k_{23}$. Measured values of $k_{21}/(k_{12}k_{23})$ show that the model is off by as much as 30%.

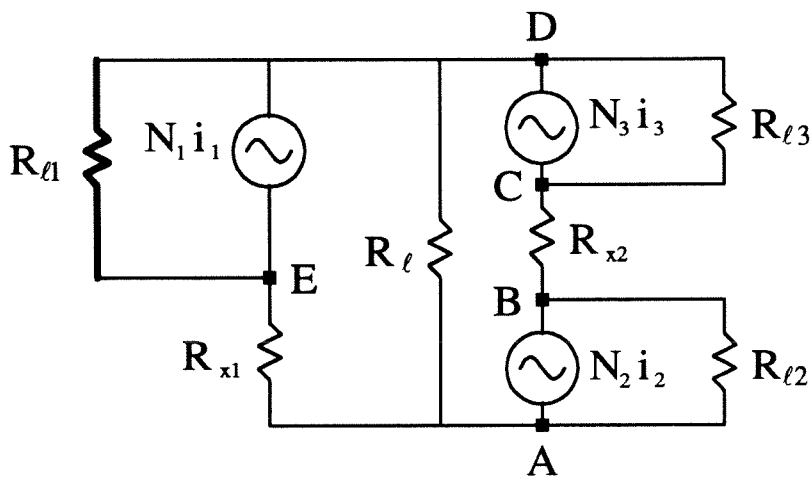

Figure 7.11: Example 6: refined reluctance model with additional leakage reluctance $\mathcal{R}_{l1}$.

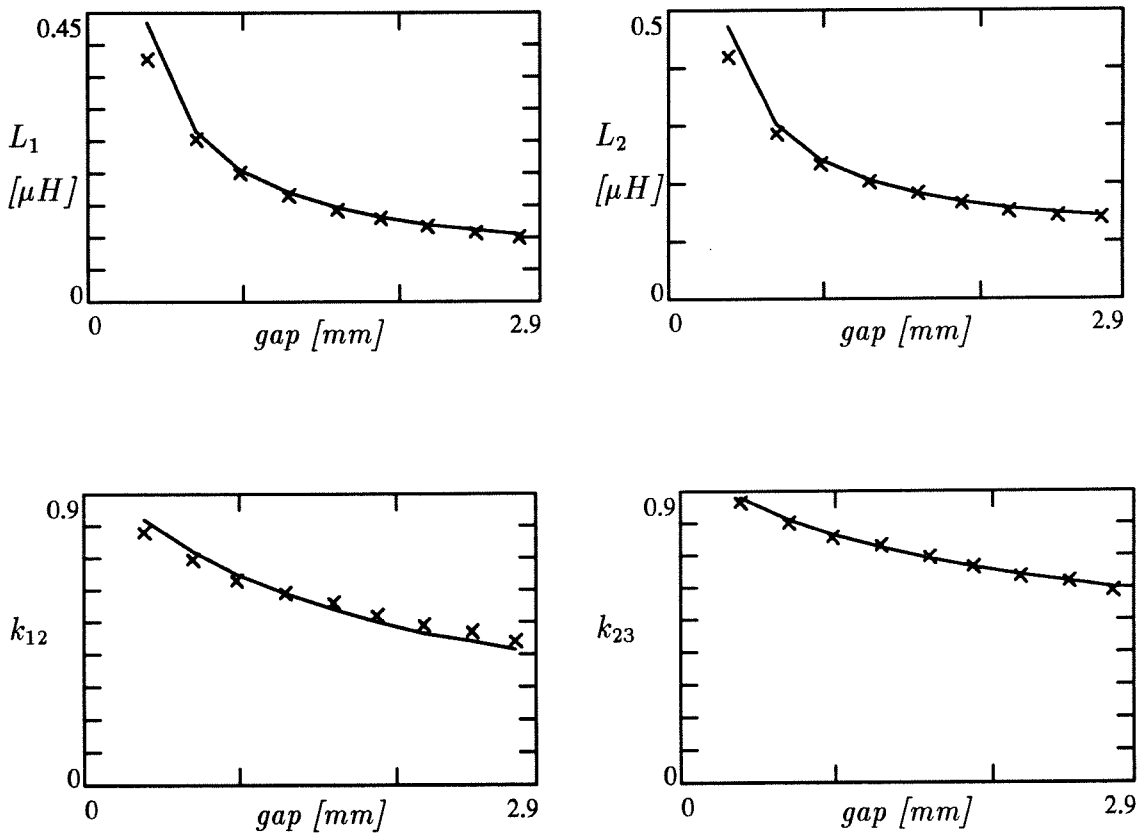

Figure 7.12: Example 6: comparison of measured and predicted values of inductances L_1, L_2 and coupling coefficients k_{12}, k_{21}.

Chapter 8

Zero Ripple Condition Sensitivity and New Coupled-Inductor Structure

In this chapter a new coupled-inductor structure is proposed that does not need turns ratio adjustment for zero current ripple. In fact, the new structure achieves zero current ripple with the *same number of turns* on the two windings, significantly simplifying design. Another advantage of the new structure is that it has greatly reduced radiated noise. It is also shown that sensitivity of the zero ripple condition is as good as the sensitivity of conventional coupled-inductor structures that use the same magnetic core.

In section 8.1, a sensitivity analysis of the zero ripple condition is presented based on the the new reluctance model of chapter 5. The main result is that sensitivity of the zero ripple condition depends on the leakage reluctance of the core. Since the leakage reluctance of a given core is constant and does not depend on gap position (see chapter 5), the sensitivity of the zero ripple condition is also independent of gap position for a given core.

In section 8.2, the new coupled-inductor structure is proposed and its advantages and disadvantages discussed.

8.1 Sensitivity Analysis

As discussed in chapter 4, in a real-life converter application coupled inductors designed for zero current ripple will inevitably have some non-zero ripple due to nonidealities, which will be called residual ripple.

The coupled-inductor structure can be represented by a two-port as shown in Fig. 8.1. As usual, coupled inductors are designed for zero current ripple on the secondary, i.e., port 2. Residual ripple is the current i_2 of Fig. 8.1. Voltage sources v_1 and v_2, not

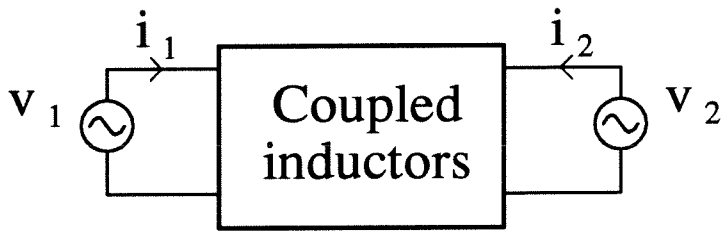

Figure 8.1: Two-port representing coupled-inductor structure.

necessarily identical, represent the voltage waveforms imposed by the converter. The residual ripple can be divided in two components as shown in Fig. 8.2. The causes of these two ripple components are different and can be so identified:

1. *Zero ripple condition mismatch.* The zero current ripple condition will not be perfectly met in a real design. A common reason for this is that one is restricted to integer number of turns. Another common reason is that the gap thickness may not be exactly equal to the value required by the zero ripple condition. Therefore, this current ripple component is due to nonidealities in the coupled inductors themselves and does not depend on the rest of the converter.

2. *Applied voltage mismatch.* The switching converter will not apply identical voltage waveforms to the two windings of the coupled inductors. Differences may be due to non-zero voltage ripple on capacitors, resistive drops on the coupled inductors due to DC current components, noise due to the switching action and so on. Therefore, this current ripple component is due to reasons external to the coupled inductors and depends on the converter design. For example, the voltage ripple on the capacitors can be reduced by increasing capacitor size.

8.1.1 Calculation of Residual Ripple from Inductance Model

Fig. 8.3a shows the reluctance model for standard UI cores derived in chapter 5, and Fig. 8.3b shows the inductance model obtained by duality. Inductances in this model have the following values:

$$L_{x1} = \frac{N_1^2}{\mathcal{R}_{x1}}$$

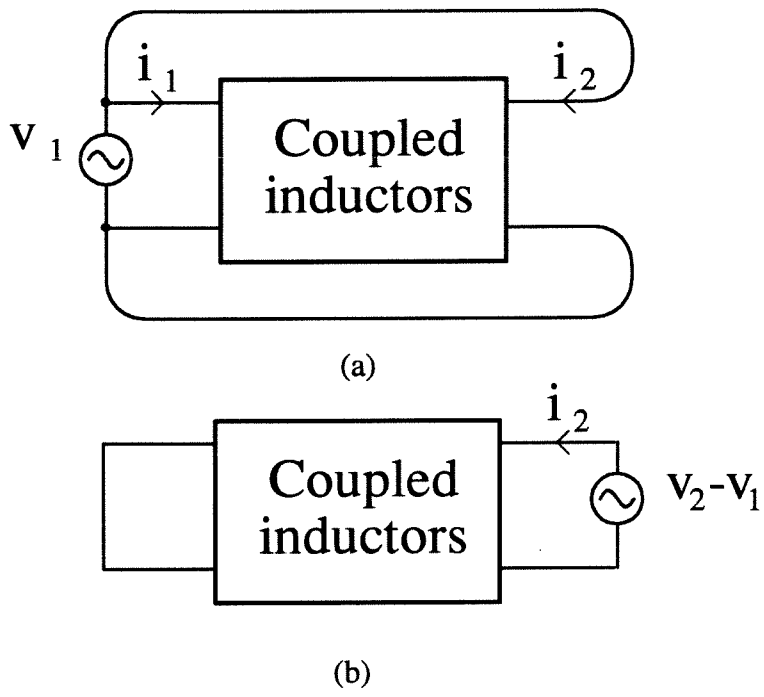

Figure 8.2: Residual ripple is divided into two components: residual ripple due to zero ripple condition mismatch (a) and residual ripple due to applied voltage mismatch (b).

$$L_{x2} = \frac{N_1^2}{\mathcal{R}_{x2}}$$
$$L_l = \frac{N_1^2}{\mathcal{R}_l}$$

The two applied voltages v_1 and v_2 are not identical due to the voltage mismatch described in the previous section. In order to evaluate current i_2, the Thévenin equivalent of the circuit to the left of points A-B is calculated as shown in Fig. 8.4a.

In Fig. 8.4b the primary is scaled by the turns ratio and reflected to the secondary side. The two voltage sources can be combined together as

$$v_{eq} = v_2 - k_1 \frac{N_2}{N_1} v_1$$

This voltage source can be divided in two components representing zero ripple condition mismatch (v_{eq1}) and applied voltage mismatch (v_{eq2}).

$$v_{eq} = \underbrace{v_1 \left(1 - k_1 \frac{N_2}{N_1}\right)}_{v_{eq1}} + \underbrace{v_2 - v_1}_{v_{eq2}}$$

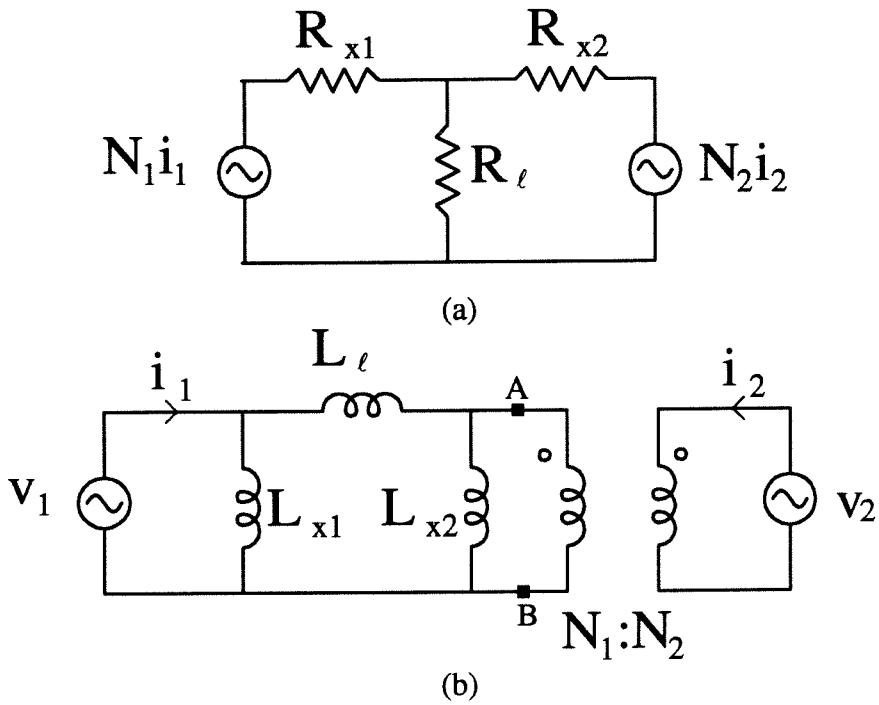

Figure 8.3: Reluctance model for standard UI cores (a) and inductance model obtained by duality (b).

Inductance L_{eq} is

$$L_{eq} = \frac{N_2^2}{\mathcal{R}_l + \mathcal{R}_{x2}} \tag{8.1}$$

The value of inductance L_{eq} is dominated by leakage reluctance $\mathcal{R}_l$ because in a normal design it is $\mathcal{R}_l > \mathcal{R}_{x2}$.

The residual ripple current i_2 is

$$i_2 = \frac{1}{L_{eq}} \int v_{eq}\, dt \tag{8.2}$$

The residual ripple due to zero ripple condition mismatch and applied voltage mismatch can be estimated from 8.2.

From (8.2) it is evident that increasing the value of L_{eq} reduces the residual ripple i_2. In other words it can be said that a coupled-inductor structure with high leakage has less *sensitivity* of the zero ripple condition to nonidealities. The same conclusion has been reached in chapter 4.

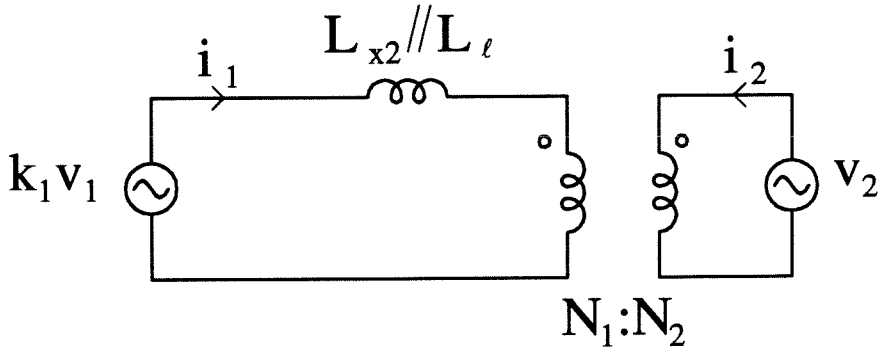

(a)

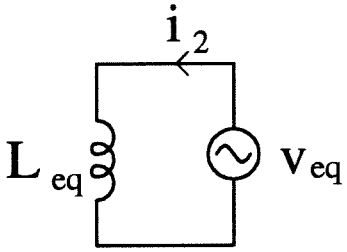

$$v_{eq} = v_2 - k_1 \frac{N_2}{N_1} v_1$$

$$L_{eq} = \frac{N_2^2}{\mathcal{R}_{x2} + \mathcal{R}_l}$$

(b)

Figure 8.4: Simplifications of the model of the previous figure to calculate residual ripple i_2.

8.2 New Core Structure

A new core structure for zero current ripple with same number of turns on the two windings is introduced here. The simplification in the design resulting from the fact that no adjustment of number of turns is needed for zero ripple is paid for in terms of zero ripple condition mismatch bigger than the one obtainable with other structures. It is shown, however, that the sensitivity to applied voltage mismatch is approximately the same as in other structures. Since applied voltage mismatch is always present in switching converter applications, the zero ripple performance of the new structure can be comparable to that of conventional structures.

From the zero ripple condition

$$k_1 = \frac{N_1}{N_2} \tag{8.3}$$

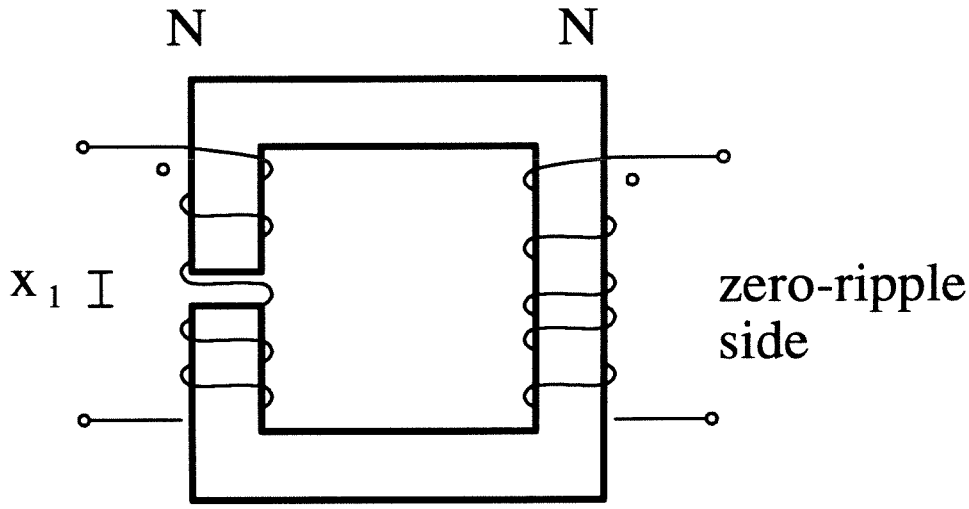

Figure 8.5: New structure gives zero current ripple on secondary side with equal number of turns in two windings.

it is evident that the same number of turns can be used for the two windings if primary coupling coefficient k_1 is unity. From the reluctance model of Fig. 8.3a, it is

$$k_1 = \frac{\mathcal{R}_l}{\mathcal{R}l + \mathcal{R}_{x2}}$$

Therefore, if $\mathcal{R}_{x2} = 0$, i.e., no gap on the secondary leg, coupling coefficient is unity and the zero ripple condition (8.3) becomes $N_1 = N_2$, identical number of turns on the two windings.

It should be remembered however that the reluctance model of Fig. 8.3a was obtained by neglecting two leakage reluctances, namely $\mathcal{R}_{l1}$ and $\mathcal{R}_{l2}$, directly in parallel with the *mmf* sources (see section 5.4.1). Due to these reluctances, in the case of primary leg gap, coupling coefficient k_1 is less than unity. It can be easily seen that k_1 will be very close to unity if neglected reluctance $\mathcal{R}_{l1}$ is much bigger than primary side reluctance $\mathcal{R}_{x1}$. Therefore, a core structure with a big value of leakage reluctance $\mathcal{R}_{l1}$ is preferable for this application. From Table 5.3 it appears that a UU-type core satisfies this requirement better than a UI-type core. The suggested core structure for zero current ripple with identical number of turns is shown in Fig. 8.5.

8.2.1 Sensitivity of New Structure

The proposed structure exhibits almost ideal coupling between primary and secondary when driven from the primary side ($k_1 \simeq 1$). In the past this kind of structure was not used for fear of high sensitivity of the zero ripple condition due to the good coupling between the two windings. It is therefore natural to question the sensitivity of the zero ripple condition in this case. The question may be asked in the following terms:

> *Given a certain magnetic core, zero current ripple coupled inductors can be realized using different gap arrangements. For example, primary gap, secondary gap and spacer gap may be used. The primary gap case is the new structure proposed here. The question is: is the zero ripple condition sensitivity for this case worse than for the other gap arrangements?*

As explained in section 8.1, the sensitivity of the zero ripple condition depends on the value of inductance L_{eq} in Fig. 8.4b, which limits the residual ripple. This inductance is given by equation (8.1). Since reluctance $\mathcal{R}_l$ is constant for a given core and does not depend on gap arrangement as shown in section 5.4, inductance L_{eq} will be approximately the same for the three gap arrangements. Therefore, the answer to the question above on sensitivity is:

> *the sensitivity of the zero ripple condition is as good as for conventional gap arrangements.*

This statement seems to be contradicted by the fact that the structure of Fig. 8.5 has a primary coupling coefficient k_1 approximately unity, but in reality this means only that if the primary winding is driven, there is no leakage flux. The fact is that *leakage needed for low sensitivity is all on the secondary side.* In fact, the secondary coupling coefficient is far from unity. This can also be seen from the inductance model of Fig. 8.3b with $L_{x2} = \infty$ (no secondary gap). This model is identical to the usual transformer model with no primary leakage inductance, magnetizing inductance equal to L_{x1} and secondary leakage inductance equal to L_l.

8.2.2 Advantages and Disadvantages of the New Structure

One advantage and one disadvantage of the new structure have already been discussed above. The advantage is that design is simplified by the fact that the two windings have the same number of turns. The disadvantage is that zero ripple condition mismatch is bigger than for other gap arrangements.

Another disadvantage is that this structure is inherently less efficient than, for example, a secondary leg gap structure in the following sense. For the same design requirements in terms of primary inductance L_1 and same DC currents I_1 and I_2, the new structure always has bigger DC flux than a secondary leg gap structure realized using the same core and the same number of primary turns N_1. This fact is proved in chapter 9.

This structure, however, has a definite advantage in the case of a design with very small number of turns (e.g., a design with big DC currents in which minimization of copper losses is important) because it avoids the "integer number of turns" problem discussed in section 9.4. This problem will be illustrated with an example.

Assume a primary number of turns $N_1 = 2$ appears adequate for the design. The secondary number of turns must satisfy zero ripple condition (8.3) and must also be an integer number. If coupling coefficient k_1 is less than unity, then N_2 must be bigger than N_1 and possible integer values for N_2 are

$$N_2 = 3, 4, 5 \ldots$$

The smallest possible number of turns is $N_2 = 3$. Zero ripple condition (8.3) requires $k_1 = 2/3$. This means that one third of the flux generated by the primary must be leakage flux. The only way to achieve this is to put a big gap to reduce the permeance of the flux path in the core. Notice that gap size is dictated by the zero ripple condition and not by DC saturation. As a result inductance L_1 will be much smaller than it could be based on DC flux saturation and the design will be rather inefficient. Increasing secondary number of turns N_2 makes the problem even worse.

No such problem exists with the new structure because N_2 is equal to N_1.

8.2.3 Experimental Verification of New Structure Sensitivity

In order to compare the new structure with other structures, the following three zero ripple coupled inductors are built using a UU60 core. In order to simplify comparison, the primary number of turns N_1 and the total gap are the same in the three cases. Number of turns is adjusted for zero ripple on the secondary side. Characteristics of the three designs are:

- New structure $N_1 = 30$ $N_2 = 30$ $x_1 = 0.55mm$ $x_2 = 0$
- Secondary gap $N_1 = 30$ $N_2 = 41$ $x_1 = 0$ $x_2 = 0.55mm$
- Primary gap $N_1 = 30$ $N_2 = 36$ $x_1 = 0.27mm$ $x_2 = 0.27mm$

The two types of residual ripple of Fig. 8.2 are considered separately and measurements are shown in Table 8.1. The residual ripple due to zero ripple condition mismatch is quantified by the ripple rejection ratio i_1/i_2 measured under the conditions of Fig. 8.2a. This ratio represents the ripple reduction due to the coupled inductors. As expected the ripple rejection ratio is worse for the new structure due to the non-perfect coupling. The residual ripple due to applied voltage mismatch is quantified by inductance L_{eq} that limits it. This inductance is the secondary inductance measured with short-circuited primary (see Fig. 8.2b). Notice that this inductance is in the same range in the three cases verifying the claim made above that the new structure has zero ripple condition sensitivity as good as the other structures normally used. Differences are due to different secondary number of turns and to the $\mathcal{R}_{x2}$ term in equation (8.1). Inductance L_{eq} can be calculated since leakage reluctance $\mathcal{R}_l$ for a UU60 core has been measured (see Table 5.3). The agreement between measurements and predictions is very good. A comparison of the performance of these three coupled-inductor structures in a switching-converter application is presented in section 9.4.

	i_1/i_2	L_{eq} $[\mu H]$	
		meas.	*pred.*
New Structure	13	0.16	0.17
Secondary Gap	64	0.23	0.23
Primary Gap	95	0.19	0.20

Table 8.1: Comparison of three magnetic structures. Ripple rejection ratio i_1/i_2 and inductance L_{eq} that limits residual ripple are measured for the three gap arrangements.

Chapter 9

Design of Coupled Inductors

In this chapter a design procedure for zero ripple coupled inductors is given based on the reluctance model of chapter 5.

In section 9.1, design equations for arbitrary gaps are presented.

In section 9.2, three special cases of practical interest are considered and design procedures are presented. One of the special cases is the new coupled-inductor structure introduced in chapter 8.

In section 9.3, a method to estimate core cross-section needed for a given design is described.

In section 9.4, the three design procedures are applied to a practical coupled-inductor design. The coupled inductors are then built and their performance compared.

9.1 Design-Oriented Analysis of Two-Winding Gapped UI Cores: General Case of Arbitrary Air Gaps in the Two Legs

The design problem for coupled inductors can be defined as follows. The coupled-inductor structure considered here is shown in Fig. 9.1a and its reluctance model is shown in Fig. 9.1b. Gap reluctances are given by

$$\begin{aligned} \mathcal{R}_{x1} &= \frac{x_1}{\mu_0 S} \\ \mathcal{R}_{x2} &= \frac{x_2}{\mu_0 S} \end{aligned} \tag{9.1}$$

where S is the core cross-section. In the case of big gaps, a correction for fringing reluctance can be introduced as described in section 5.5. The inductance model obtained by duality from the reluctance model is shown in Fig.9.1c. Inductances in this model are

given by

$$\begin{aligned} L_{x1} &= \frac{N_1^2}{\mathcal{R}_{x1}} \\ L_{x2} &= \frac{N_2^2}{\mathcal{R}_{x2}} \\ L_l &= \frac{N_1^2}{\mathcal{R}_l} \end{aligned} \tag{9.2}$$

It is assumed that the magnetic core has already been chosen and its cross-section S, leakage reluctance $\mathcal{R}_l$ and maximum allowable flux density B_M are known. From the converter design specifications, peak currents I_1 and I_2 in the coupled inductors are known. These currents determine peak flux in the core as shown in Fig. 3.1. Zero ripple current in the secondary is desired. There are four degrees of freedom in the design: primary and secondary number of turns N_1 and N_2, primary and secondary gap thicknesses x_1 and x_2.

Design specifications are as follows:

1. Zero current ripple condition on the secondary must be satisfied.
2. Primary inductance L_1 must have specified value. L_1 is designed to give desired current ripple in the primary.
3. Flux density everywhere in the core must be below saturation value B_M. This means that fluxes ϕ_1 and ϕ_2 on both core legs must be below saturation level.

9.1.1 Zero Ripple Condition

The zero ripple condition (3.4) is

$$k_1 = \frac{N_1}{N_2} \tag{9.3}$$

Coupling coefficient k_1 is the ratio of secondary flux ϕ_2 and primary flux ϕ_1 under the condition of open-circuited secondary. This condition is equivalent to shorting the *mmf* source $N_2 i_2$ in the reluctance model. From the reluctance model it follows that

$$k_1 = \frac{\mathcal{R}_l}{\mathcal{R}_l + \mathcal{R}_{x2}} \tag{9.4}$$

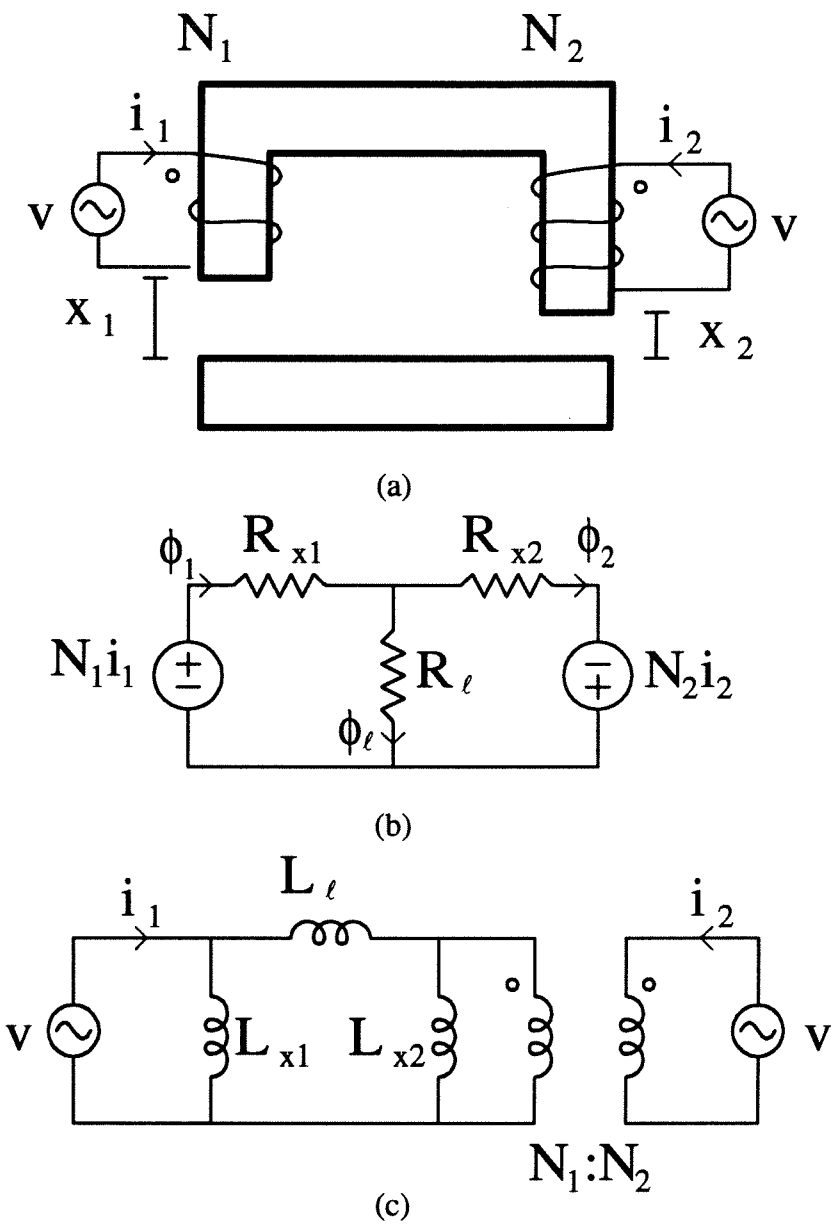

Figure 9.1: Two-winding UI core with different gaps on the two legs (a), its reluctance model (b) and its inductance model (c).

From (9.3) and (9.4) the zero ripple condition is

$$\frac{N_1}{N_2} = \frac{\mathcal{R}_l}{\mathcal{R}_l + \mathcal{R}_{x2}} \tag{9.5}$$

9.1.2 Primary Inductance L_1

Primary inductance L_1 can be obtained from the inductance model of Fig. 9.1c

$$L_1 = L_{x1} \| (L_{x2} + L_l) \tag{9.6}$$

Substituting (9.2) into (9.6)

$$L_1 = \frac{N_1^2}{\mathcal{R}_{x1} + \mathcal{R}_{x2} \| \mathcal{R}_l} \tag{9.7}$$

9.1.3 Saturation Condition

From the reluctance model peak fluxes in the two legs can be calculated (using, for example, superposition) as

$$\phi_1 = \frac{N_1 I_1}{\mathcal{R}_{x1} + \mathcal{R}_{x2} \| \mathcal{R}_l} + \frac{N_2 I_2}{\mathcal{R}_{x2} + \mathcal{R}_{x1} \| \mathcal{R}_l} \frac{\mathcal{R}_l}{\mathcal{R}_l + \mathcal{R}_{x1}} \tag{9.8}$$

$$\phi_2 = \frac{N_1 I_1}{\mathcal{R}_{x1} + \mathcal{R}_{x2} \| \mathcal{R}_l} \frac{\mathcal{R}_l}{\mathcal{R}_l + \mathcal{R}_{x2}} + \frac{N_2 I_2}{\mathcal{R}_{x2} + \mathcal{R}_{x1} \| \mathcal{R}_l} \tag{9.9}$$

In appendix B it is shown that for a generic coupled inductor structure it is

$$\phi_1 = \frac{L_1}{N_1} \left(I_1 + k_1 \frac{N_2}{N_1} I_2 \right) \tag{9.10}$$

This result is completely general and is valid for any two-winding coupled-inductor structure. The only assumption made is that the structure is a linear reciprocal two-port. If the zero ripple condition (9.3) is satisfied, (9.10) becomes

$$\phi_1 = \frac{L_1}{N_1} (I_1 + I_2) \tag{9.11}$$

This equation can be used instead of equation (9.8). The advantage is that equation (9.11) contains a single unknown, primary number of turns N_1. This equation was derived in the past [5] for a specific reluctance model and was the key that allowed to obtain design equations for coupled inductors in closed form.

Another observation is that no such simple equation exists for secondary flux ϕ_2. It is possible to write an equation similar to (9.10) by making an index substitution 1→2, 2→1, but the resulting equation

$$\phi_2 = \frac{L_2}{N_2}\left(I_2 + k_2\frac{N_1}{N_2}I_1\right)$$

is not useful because it is in terms of the secondary side inductance L_2 and the secondary coupling coefficient k_2, both unknown.

In order to avoid core saturation, peak fluxes must satisfy conditions

$$\begin{aligned}\phi_1 &\leq B_M S \\ \phi_2 &\leq B_M S\end{aligned} \tag{9.12}$$

In order to fully utilize the core material, these equations can be taken as equalities for the design.

9.1.4 General Design Problem

At this point, the design problem for coupled inductors can be summarized as follows:

- Unknowns: N_1, N_2, x_1, x_2
- Equations:
  - zero ripple condition (9.5)
  - inductance condition (9.7)
  - two saturation conditions: equations (9.12) with peak fluxes given by equations (9.8) and (9.9). Equation (9.8) can be substituted by equation (9.11).

These equations are rewritten here for convenience:

$$\frac{N_1}{N_2} = \frac{\mathcal{R}_l}{\mathcal{R}_l + \mathcal{R}_{x2}} \tag{9.13}$$

$$L_1 = \frac{N_1^2}{\mathcal{R}_{x1} + \mathcal{R}_{x2}\|\mathcal{R}_l} \tag{9.14}$$

$$B_M S \geq \phi_1 = \frac{N_1 I_1}{\mathcal{R}_{x1} + \mathcal{R}_{x2}\|\mathcal{R}_l} + \frac{N_2 I_2}{\mathcal{R}_{x2} + \mathcal{R}_{x1}\|\mathcal{R}_l}\,\frac{\mathcal{R}_l}{\mathcal{R}_l + \mathcal{R}_{x1}} \tag{9.15}$$

$$or \quad \phi_1 = \frac{L_1}{N_1}(I_1 + I_2)$$

$$B_M S \geq \phi_2 = \frac{N_1 I_1}{\mathcal{R}_{x1} + \mathcal{R}_{x2} \| \mathcal{R}_l} \frac{\mathcal{R}_l}{\mathcal{R}_l + \mathcal{R}_{x2}} + \frac{N_2 I_2}{\mathcal{R}_{x2} + \mathcal{R}_{x1} \| \mathcal{R}_l} \tag{9.16}$$

The design problem becomes well-defined if we take the two inequalities (9.15) and (9.16) as equalities, so that there are four conditions and four unknowns. As mentioned earlier, these conditions guarantee full core utilization.

9.2 Design Procedure for Special Gap Arrangements

It should be pointed out that the core structure of Fig. 9.1a with greatly different gaps on the two legs is rather impractical. Special cases of practical importance are

1. secondary leg gap $\Rightarrow x_1 = 0$
2. primary leg gap $\Rightarrow x_2 = 0$
3. spacer gap $\Rightarrow x_1 = x_2$

The second case is the new coupled-inductor structure proposed in chapter 8. In all these cases a degree of freedom in the design is lost because the two gaps cannot be independently chosen. Therefore, it is not possible to satisfy both (9.15) and (9.16) saturation equations as equalities. One of the two legs will have an higher flux density and the best core utilization is obtained when this leg reaches the maximum flux density B_M. Only one of the saturation equations is satisfied as an equality. It is important to apply the saturation condition to the leg with higher flux density. If the wrong leg is chosen, the other leg will saturate. In the following sections design equations (9.13), (9.14), (9.15) and (9.16) are specialized for the three gap arrangements listed above. It is then determined which leg saturates first and finally closed-form design equations are given.

9.2.1 Secondary Leg Gap

For the case of gap concentrated on the secondary leg as in Fig. 9.2, it is

$$x_1 = 0 \quad \Rightarrow \quad \mathcal{R}_{x1} = 0 \tag{9.17}$$

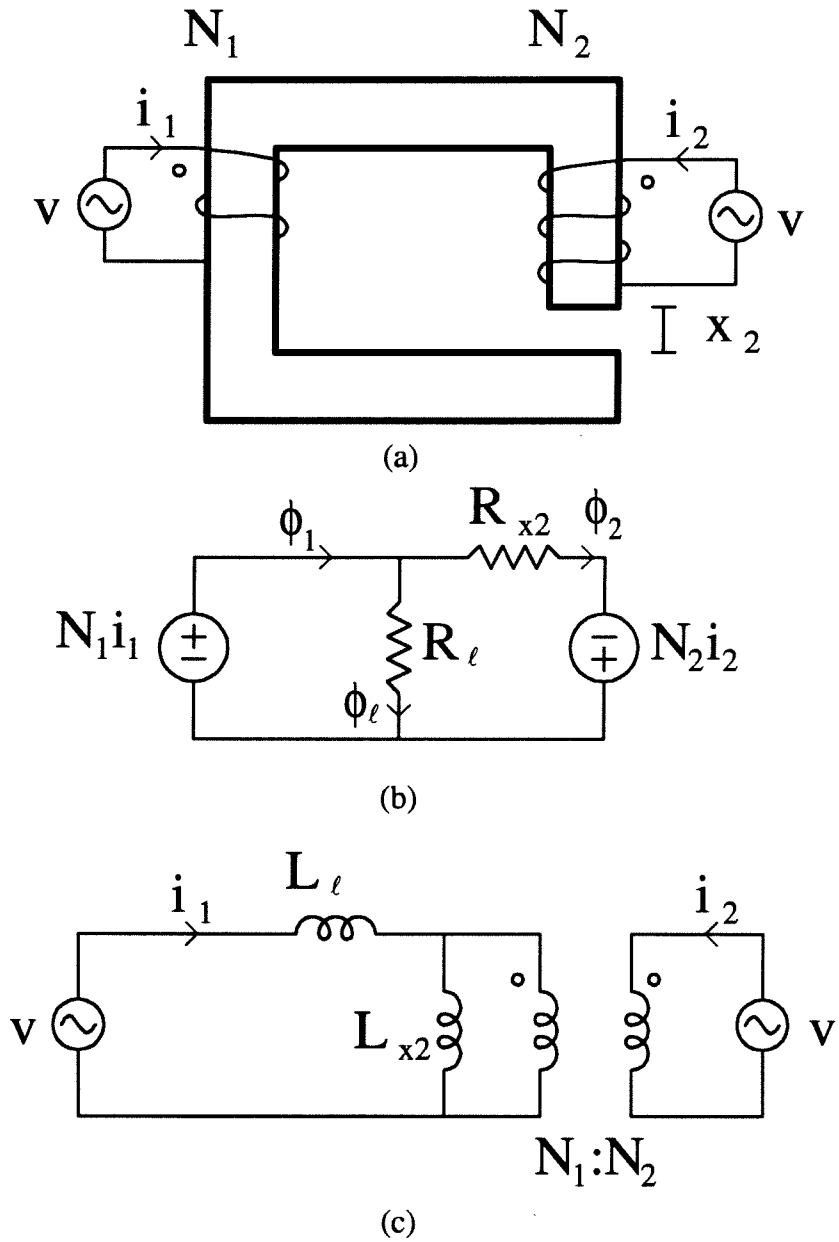

Figure 9.2: Two-winding UI core with secondary leg gap (a), its reluctance model (b) and its inductance model (c).

Equation (9.17) is substituted into design equations (9.13), (9.14), (9.15) and (9.16), giving

$$\frac{N_1}{N_2} = \frac{\mathcal{R}_l}{\mathcal{R}_l + \mathcal{R}_{x2}} \tag{9.18}$$

$$L_1 = \frac{N_1^2}{\mathcal{R}_{x2} \| \mathcal{R}_l} \tag{9.19}$$

$$B_M S \geq \phi_1 = \frac{N_1 I_1}{\mathcal{R}_{x2} \| \mathcal{R}_l} + \frac{N_2 I_2}{\mathcal{R}_{x2}} \tag{9.20}$$

$$or \quad \phi_1 = \frac{L_1}{N_1}(I_1 + I_2) \tag{9.21}$$

$$B_M S \geq \phi_2 = \frac{N_1 I_1}{\mathcal{R}_{x2} \| \mathcal{R}_l} \frac{\mathcal{R}_l}{\mathcal{R}_l + \mathcal{R}_{x2}} + \frac{N_2 I_2}{\mathcal{R}_{x2}} \tag{9.22}$$

From inspection of equations (9.20) and (9.22), it is evident that inequality (9.20) is more restrictive. This means that the primary leg always saturates first. This fact can also be seen from Fig. 9.2b because fluxes are positive in the directions shown and primary leg flux ϕ_1 is the sum of secondary leg flux ϕ_2 and leakage flux ϕ_l. Therefore, the saturation design equation to be used is equation (9.21) taken as an equality.

At this point, closed-form design equations can be derived from (9.18), (9.19) and (9.21).

Design Procedure for Secondary Leg Gap

1. Primary number of turns N_1 is calculated using (9.21).

$$N_1 = \frac{L_1(I_1 + I_2)}{B_M S} \tag{9.23}$$

2. Secondary leg reluctance $\mathcal{R}_{x2}$ is calculated from (9.19).

$$\mathcal{R}_{x2} = \frac{1}{L_1/N_1^2 - 1/\mathcal{R}_l} \tag{9.24}$$

From $\mathcal{R}_{x2}$ the gap thickness x_2 can be calculated using (9.1).

3. Finally, the secondary number of turns N_2 can be calculated from (9.18).

$$N_2 = N_1 \frac{\mathcal{R}_l + \mathcal{R}_{x2}}{\mathcal{R}_l} \tag{9.25}$$

9.2.2 Primary Leg Gap

For the case of gap concentrated on the primary leg as in Fig. 9.3, it is

$$x_2 = 0 \quad \Rightarrow \quad \mathcal{R}_{x2} = 0 \tag{9.26}$$

Equation (9.26) is substituted into design equations (9.13), (9.14), (9.15) and (9.16), giving

$$N_1 = N_2 \tag{9.27}$$

$$L_1 = \frac{N_1^2}{\mathcal{R}_{x1}} \tag{9.28}$$

$$B_M S \geq \phi_1 = \frac{N_1 I_1}{\mathcal{R}_{x1}} + \frac{N_2 I_2}{\mathcal{R}_{x1} \| \mathcal{R}_l} \frac{\mathcal{R}_l}{\mathcal{R}_l + \mathcal{R}_{x1}} \tag{9.29}$$

$$or \quad \phi_1 = \frac{L_1}{N_1} (I_1 + I_2) \tag{9.30}$$

$$B_M S \geq \phi_2 = \frac{N_1 I_1}{\mathcal{R}_{x1}} + \frac{N_2 I_2}{\mathcal{R}_{x1} \| \mathcal{R}_l} \tag{9.31}$$

From inspection of equations (9.29) and (9.31), it is evident that inequality (9.31) is more restrictive than (9.29), which means that the secondary leg always saturates first. This fact can also be seen from Fig. 9.3b because fluxes are positive in the directions shown and it is

$$\phi_2 = \phi_1 + \phi_l \tag{9.32}$$

Therefore, the saturation design equation to be used is equation (9.31) taken as an equality.

A couple of steps are needed to put this equation in a form suitable for design. First of all, equation (9.27) is substituted into equation (9.31) to eliminate N_2. Equation (9.31) can then be rewritten in the form of equation (9.32) as

$$\underbrace{B_M S}_{\phi_2} = \underbrace{\frac{N_1(I_1 + I_2)}{\mathcal{R}_{x1}}}_{\phi_1} + \underbrace{\frac{N_1 I_2}{\mathcal{R}_l}}_{\phi_l} \tag{9.33}$$

Substituting (9.30) into (9.33)

$$\underbrace{B_M S}_{\phi_2} = \underbrace{\frac{L_1}{N_1}(I_1 + I_2)}_{\phi_1} + \underbrace{\frac{N_1 I_2}{\mathcal{R}_l}}_{\phi_l} \tag{9.34}$$

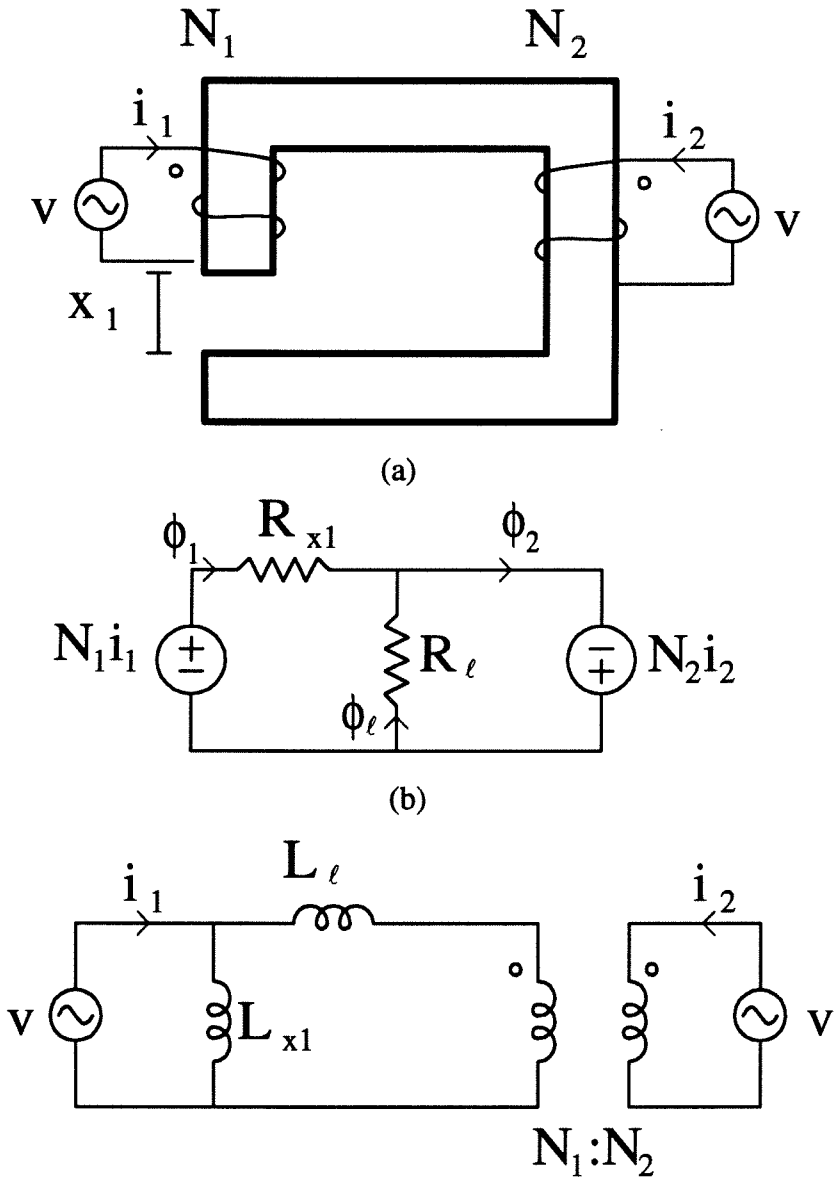

Figure 9.3: Two-winding UI core with primary leg gap (a), its reluctance model (b) and its inductance model (c).

Notice that equation (9.34) is a second-order equation in N_1. It can be easily checked that the two solutions are both positive. Therefore, it is not immediately evident which one should be chosen. It turns out that the solution with the *smaller number of turns* gives a more efficient design.

To understand what happens it can be helpful to plot equation (9.34) as a function of N_1 as shown in Fig. 9.4. The horizontal line is the saturation flux $B_M S$. The two solutions are the intersections of the two curves, which are $N_1 = 2.8$ and $N_1 = 78$. In Fig. 9.5 the two components ϕ_1 and ϕ_l are plotted separately. Their sum gives the total flux ϕ_2. It can be seen that for $N_1 = 3.1$ coupling flux ϕ_1 is much bigger than leakage flux ϕ_l. On the other hand, for $N_1 = 78$ leakage flux ϕ_l is much bigger than coupling flux ϕ_1 and a big number of turns is needed to obtain the desired inductance L_1. The second design with such a big number of turns is very inefficient due to copper losses in the windings. For this reason, the solution with smaller number of turns should always be chosen.

Design Procedure for Primary Gap

1. Primary number of turns N_1 is calculated from the second-order equation (9.34). As explained above, the smaller solution is chosen.

$$N_1 = \frac{B_M S \mathcal{R}_l}{2I_2} - \sqrt{\left(\frac{B_M S \mathcal{R}_l}{2I_2}\right)^2 - L_1 \mathcal{R}_l \left(1 + \frac{I_1}{I_2}\right)} \tag{9.35}$$

2. Primary leg reluctance $\mathcal{R}_{x1}$ is calculated from (9.26).

$$\mathcal{R}_{x1} = \frac{N_1^2}{L_1} \tag{9.36}$$

   From $\mathcal{R}_{x1}$ the gap thickness x_1 can be calculated using (9.1).

3. Secondary number of turns N_2 is identical to primary number of turns N_1.

9.2.3 Comparison of Secondary Leg Gap and Primary Leg Gap Design

A comparison of coupled-inductor design with secondary leg gap and with primary leg gap can now be performed. To distinguish between the two cases, an index p is used for the primary leg case and an index s is used for the secondary leg case. Let us assume

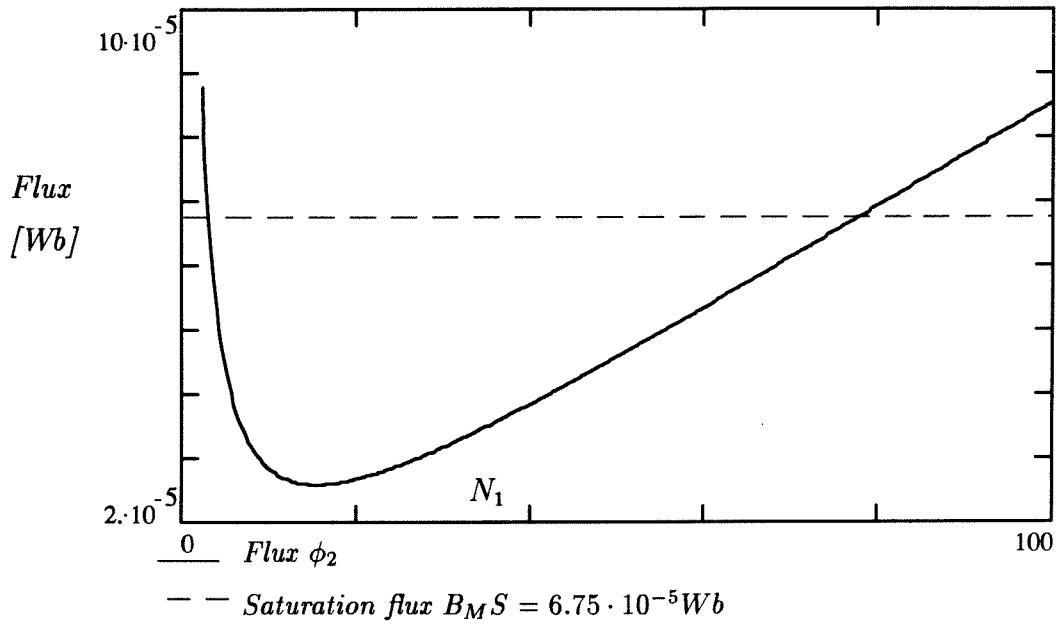

Figure 9.4: Flux ϕ_2 and saturation flux $B_M S$ as a function of primary number of turns N_1. The following numerical values are used: $I_1 = I_2 = 5A$, $\mathcal{R}_l = 6\ [1/\mu H]$ and $L_1 = 20\ \mu H$. There are two possible solutions with different number of turns given by the intersections of the two curves.

that an inductance L_1 is desired and the same primary number of turns N_1 is used. Equations (9.28) and (9.19) give

Primary leg gap	Secondary leg gap
$L_1 = \dfrac{N_1^2}{\mathcal{R}_{x1p}}$	$L_1 = \dfrac{N_1^2}{\mathcal{R}_{x2s} \| \mathcal{R}_l}$

(9.37)

In order to have the same inductance L_1 it must be

$$\mathcal{R}_{x1p} = \mathcal{R}_{x2s} \| \mathcal{R}_l \tag{9.38}$$

Substituting (9.27) into (9.31) and (9.18) into (9.20), the following expressions for the peak fluxes in the two cases are obtained

Primary leg gap	Secondary leg gap

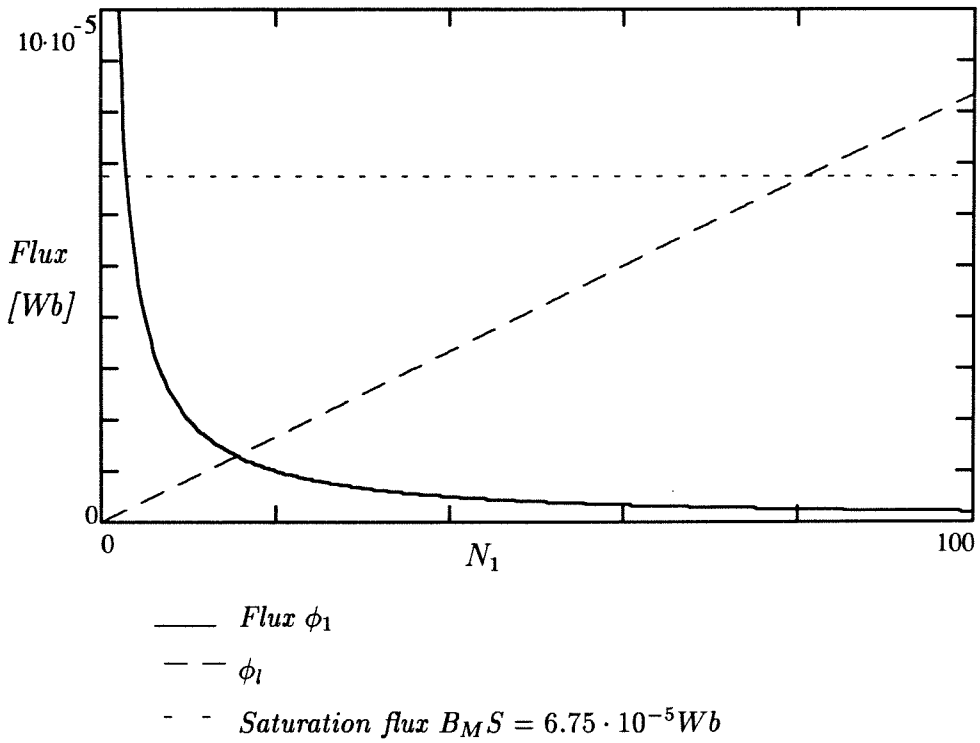

Figure 9.5: The two components of flux ϕ_2, namely flux ϕ_1 and flux ϕ_l, are plotted separately to show that the solution with bigger number of turns is undesirable because leakage flux ϕ_l is much bigger than coupling flux ϕ_1.

$$\phi_{2p} = \frac{N_1(I_1 + I_2)}{\mathcal{R}_{x1p}} + \frac{N_1 I_2}{\mathcal{R}_l} \qquad \phi_{1s} = \frac{N_1(I_1 + I_2)}{\mathcal{R}_{x2s} \| \mathcal{R}_l} \tag{9.39}$$

From equations (9.38) and (9.39) it follows that

$$\phi_{2p} = \phi_{1s} + \frac{N_1 I_2}{\mathcal{R}_l}$$

Therefore, it is always $\phi_{2p} \geq \phi_{1s}$, i.e., the primary leg gap design has bigger peak flux, which means that for the same design specifications, a bigger core is needed in this case. The conclusion is that the primary leg gap design is inherently less efficient than the secondary leg gap design. Intuitively, this can be explained looking at equations (9.37): in the case of secondary leg gap the leakage reluctance contributes to inductance L_1, whereas in the other case it does not. However, in both cases leakage flux ϕ_l contributes to the saturation flux.

9.2.4 Spacer Gap

The third and last special case considered is the case of spacer gap. For this case it is

$$x_1 = x_2 \quad \Rightarrow \quad \mathcal{R}_{x1} = \mathcal{R}_{x2} = \mathcal{R}_x \tag{9.40}$$

Equation (9.40) is substituted into design equations (9.13), (9.14), (9.15) and (9.16), giving

$$\frac{N_1}{N_2} = k_1 = \frac{\mathcal{R}_l}{\mathcal{R}_l + \mathcal{R}_x} \tag{9.41}$$

$$L_1 = \frac{N_1^2}{\mathcal{R}_x + \mathcal{R}_x \| \mathcal{R}_l} \tag{9.42}$$

$$B_M S \geq \phi_1 = \frac{N_1 I_1}{\mathcal{R}_x + \mathcal{R}_x \| \mathcal{R}_l} + \frac{N_2 I_2}{\mathcal{R}_x + \mathcal{R}_x \| \mathcal{R}_l} \frac{\mathcal{R}_l}{\mathcal{R}_l + \mathcal{R}_x} \tag{9.43}$$

$$or \quad \phi_1 = \frac{L_1}{N_1}(I_1 + I_2) \tag{9.44}$$

$$B_M S \geq \phi_2 = \frac{N_1 I_1}{\mathcal{R}_x + \mathcal{R}_x \| \mathcal{R}_l} \frac{\mathcal{R}_l}{\mathcal{R}_l + \mathcal{R}_x} + \frac{N_2 I_2}{\mathcal{R}_x + \mathcal{R}_x \| \mathcal{R}_l} \tag{9.45}$$

As in the previous cases, it is necessary to determine which one of conditions (9.43) and (9.45) is more restrictive. Substituting (9.41) into (9.43) and (9.45) we get

$$\phi_1 = \frac{N_1}{\mathcal{R}_x + \mathcal{R}_x \| \mathcal{R}_l}(I_1 + I_2) \tag{9.46}$$

$$\phi_2 = \frac{N_1}{\mathcal{R}_x + \mathcal{R}_x \| \mathcal{R}_l}\left(k_1 I_1 + \frac{I_2}{k_1}\right) \tag{9.47}$$

From these equations it is clear that $\phi_1 > \phi_2$ if

$$I_1 + I_2 > k_1 I_1 + \frac{I_2}{k_1}$$

This condition can be rewritten as

$$k_1 > \frac{I_2}{I_1} \tag{9.48}$$

Therefore there are two cases, i.e.,

$$\begin{aligned} &\text{Case 1} \quad k_1 > \frac{I_2}{I_1} \quad \Rightarrow \quad \text{primary leg saturates first} \\ &\text{Case 2} \quad k_1 < \frac{I_2}{I_1} \quad \Rightarrow \quad \text{secondary leg saturates first} \end{aligned} \tag{9.49}$$

In the first case, equation (9.44) can be used and a closed-form solution found. In the second case, no simple closed-form solution was found. This is due to the fact that no simple equation like (9.44) relating flux to number of turns exists in the case of secondary leg flux. In fact, equation (9.44) can be directly derived substituting (9.42) into (9.46), but the analogous substitution of (9.42) into (9.47) for the secondary leg flux gives

$$\phi_2 = \frac{L_1}{N_1}\left(k_1 I_1 + \frac{I_2}{k_1}\right) \tag{9.50}$$

This formula still has two unknowns, namely k_1 and N_1, and cannot be solved by itself.

A method to overcome this problem is to estimate the value of k_1, plug it into (9.50) and determine primary number of turns N_1.

Estimation of k_1

Coupling coefficient k_1 can be estimated as follows. Equation (9.42) is divided by equation (9.47) squared to eliminate N_1. The result is

$$\frac{L_1}{\phi_2^2} = \frac{\mathcal{R}_x + \mathcal{R}_x \| \mathcal{R}_l}{(k_1 I_1 + I_2/k_1)^2} \tag{9.51}$$

This equation still has two unknowns, namely $\mathcal{R}_x$ and k_1, but from (9.41) gap reluctance can be expressed in terms of k_1 as

$$\mathcal{R}_x = \frac{1 - k_1}{k_1}\,\mathcal{R}_l \tag{9.52}$$

Equation (9.52) can be used to eliminate $\mathcal{R}_x$ from (9.51). The result is

$$\frac{L_1}{\phi_2^2} = \frac{\mathcal{R}_l(1/k_1 - k_1)}{(k_1 I_1 + I_2/k_1)^2} \tag{9.53}$$

If flux ϕ_2 is taken to be equal to saturation flux ϕ_{2sat}, this equation has only one unknown, k_1, but it is a fourth order equation.

It can be useful to plot equation (9.53) as shown in Fig. 9.6. For this plot arbitrary values for $\mathcal{R}_l$, I_1 and I_2 are chosen, but it turns out that the plot shape is always the same for all practical choices of these quantities. The solid-line plot of Fig. 9.53 represents the right hand side of equation (9.53). From design specifications the desired value of L_1/ϕ_2^2 can be determined and results in the horizontal dotted line of Fig. 9.6. Intersections between the two lines determine values of k_1 that satisfy design specifications. From this

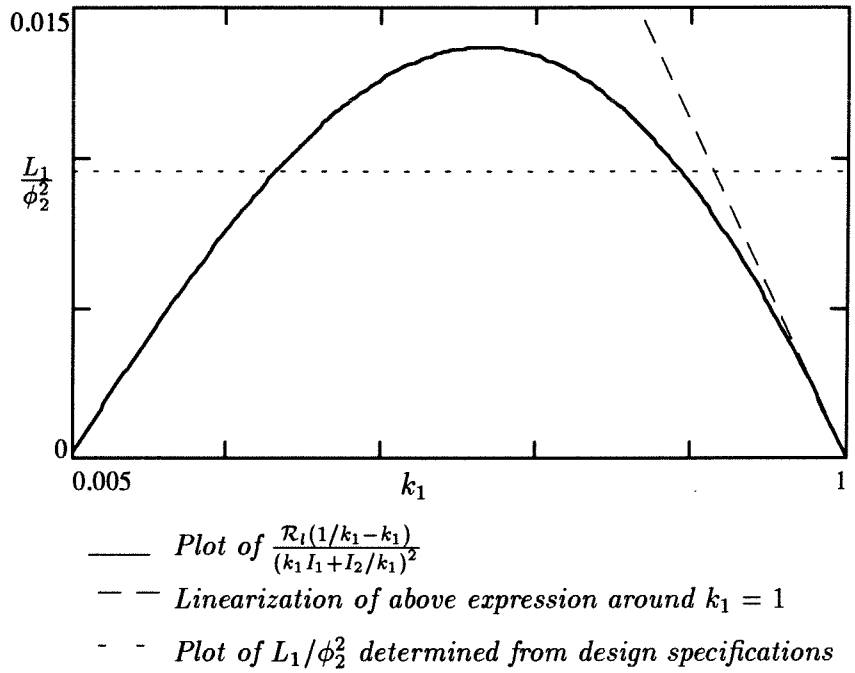

Figure 9.6: Plot of L_1/ϕ_2^2 as a function of k_1 for arbitrary values of $\mathcal{R}_l$, I_1 and I_2.

figure it is apparent that there are either two solutions for k_1 or no solution. In the case of no solution, the desired inductance L_1 cannot be obtained from the given core without exceeding specified flux ϕ_2. In the case of two solutions, the one with k_1 closer to unity should be chosen, so that the secondary number of turns N_2 will be close to the primary number of turns N_1, minimizing copper losses.

Instead of solving equation (9.53) graphically, it is more practical to linearize it in the region of interest. Since solutions with k_1 close to unity are sought, equation (9.53) can be linearized around $k_1 = 1$. The result is

$$\frac{L_1}{\phi_2^2} = \frac{2\mathcal{R}_l}{(I_1 + I_2)^2}(1 - k_1) \tag{9.54}$$

The right hand side of (9.54) is the dashed line of Fig. 9.6. Once k_1 is estimated using (9.54), equation (9.50) can be used to calculate primary number of turns N_1.

Design Procedure for Spacer Gap

In the design procedure it is necessary to distinguish between case 1 and case 2 defined in (9.49).

Case 1: $k_1 > I_2/I_1$

1. Primary number of turns N_1 is calculated using (9.44).

$$N_1 = \frac{L_1(I_1 + I_2)}{B_M S} \tag{9.55}$$

2. Leg reluctance $\mathcal{R}_x$ is calculated from (9.42).

$$\mathcal{R}_x = -\left(\mathcal{R}_l - \frac{N_1^2}{2L_1}\right) + \sqrt{\left(\mathcal{R}_l - \frac{N_1^2}{2L_1}\right)^2 + \frac{N_1^2}{L_1}\mathcal{R}_l}$$

   From $\mathcal{R}_x$ the gap thickness x can be calculated using (9.1).

3. Finally, the secondary number of turns N_2 can be calculated from (9.41).

$$N_2 = N_1 \frac{\mathcal{R}_l + \mathcal{R}_x}{\mathcal{R}_l} \tag{9.56}$$

Case 2: $k_1 < I_2/I_1$

1. Estimation of k_1 is done using (9.54).

$$k_1 \simeq 1 - \frac{L_1(I_1 + I_2)^2}{2\mathcal{R}_l(B_M S)^2}$$

2. Primary number of turns N_1 is calculated using (9.50).

$$N_1 = \frac{L_1}{B_M S}(k_1 I_1 + I_2/k_1)$$

3. Leg reluctance $\mathcal{R}_x$ is calculated from (9.42).

$$\mathcal{R}_x = -\left(\mathcal{R}_l - \frac{N_1^2}{2L_1}\right) + \sqrt{\left(\mathcal{R}_l - \frac{N_1^2}{2L_1}\right)^2 + \frac{N_1^2}{L_1}\mathcal{R}_l}$$

   From $\mathcal{R}_x$ the gap thickness x can be calculated using (9.1).

4. Finally, the secondary number of turns N_2 can be calculated from (9.41).

$$N_2 = N_1 \frac{\mathcal{R}_l + \mathcal{R}_x}{\mathcal{R}_l}$$

Remark about case 2 In case 2 there is an approximation in the first step of the design procedure. Notice, however, that step 3 guarantees that inductance L_1 has the desired value and step 4 guarantees that the zero ripple condition is met. The approximation is in the remaining design specification, i.e., saturation flux density $\phi_{2sat} = B_M S$. Flux ϕ_2 will be somewhat bigger than the desired value, and in some cases a design iteration may be needed with an increased value of N_1.

9.3 Choice of Core: Estimation of Core Cross-Section

In the design procedures described above, it is assumed that the magnetic core has already been chosen and its cross-section S and leakage reluctance $\mathcal{R}_l$ are known. Therefore, some method for the sizing of the magnetic core is needed. In this section a procedure to determine required core cross-section is given. Once this value is determined, the designer can pick a core with a cross-section close to the value so calculated and use the design procedures described in the previous section.

The estimation of cross-section is done for the spacer gap case, but it is intended to be used regardless of the gap arrangement in the final design. Since only an approximate result is needed, it is felt that there is no need for separate procedures for different gap arrangements. The procedure is as follows.

First of all, a leakage parameter ℓ is defined for a given core according to the equation

$$\mathcal{R}_l = \frac{\ell}{\mu_0 S} \tag{9.57}$$

Since $\mathcal{R}_l$ is constant for a given core, so is leakage parameter ℓ. It is a measure of how "leaky" a certain core is. This quantity has already been defined in [5], where it was found that for many standard cores it has an approximately constant value $\ell \approx 2$mm. This value will also be assumed in the following.

The procedure starts by picking a value for k_1, usually in the range $0.6 \div 0.9$. Using (9.49) it is possible to see whether primary leg or secondary leg saturates first (case 1 and case 2 respectively). Substituting (9.57) and (9.1) into (9.41) we get

$$k_1 = \frac{\ell/(\mu_0 S)}{(\ell + x)/(\mu_0 S)} = \frac{\ell}{\ell + x}$$

From this equation gap x can be calculated as

$$x = \frac{1 - k_1}{k_1}\ell$$

The quantity $N_1 S$ is calculated next. In case 1 from (9.44)

$$N_1 S = \frac{L_1(I_1 + I_2)}{B_M} \tag{9.58}$$

and in case 2 from (9.50)

$$N_1 S = \frac{L_1\,(k_1 I_1 + I_2/k_1)}{B_M} \tag{9.59}$$

From equation (9.42) the core cross-section S is

$$S = \frac{\mu_0 (N_1 S)^2}{L_1(x + x\|\ell)}$$

Note that $N_1 S$ is known and is given by (9.58) or (9.59).

9.4 Experimental Verification of Coupled-Inductor Design Procedures

Three coupled-inductor designs using the three design procedures described above are realized for the same converter specifications. This is done for two reasons: the first reason is to verify the design procedures and give a practical design example, the second reason is to compare the performances of the three coupled-inductor structures for the same design.

In the design process, an *"integer number problem"* is encountered, due to the fact that windings can have only integer number of turns.

The design process consists of the following steps:

- Extraction of coupled-inductor specifications from converter specifications.
- Measurement of leakage and fringing reluctance for the core used in the design.
- Application of design procedures given above.

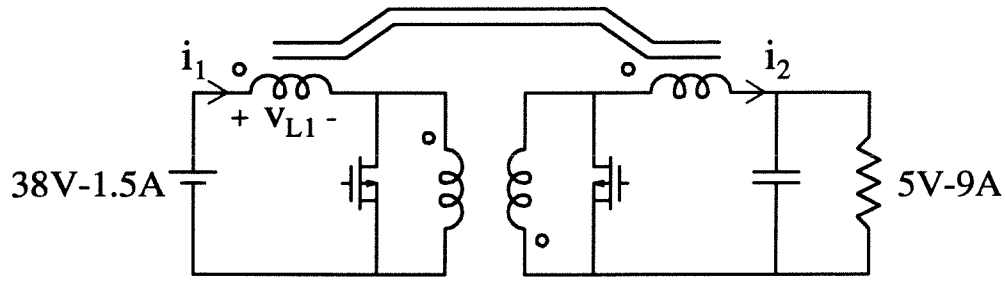

Figure 9.7: Soft-switching Ćuk converter prototype.

9.4.1 Extraction of Coupled-Inductor Specifications from Converter Specifications

The converter used for this experiment is a soft-switching isolated Ćuk converter shown in Fig. 9.7. We want to couple input and output inductors and have zero current ripple on the output inductor.

Converter specifications are:

$$\begin{aligned} \textit{Input voltage} \quad & V_g = 38\,V \\ \textit{DC input current} \quad & I_{1\,DC} = 1.5\,A \end{aligned} \tag{9.60}$$

$$\begin{aligned} \textit{Output voltage} \quad & v_0' = 5\,V \\ \textit{Output current} \quad & I_2' = 9\,A \\ \textit{Isolation transformer} \quad & 3:1 \\ \textit{Reflected output voltage} \quad & v_0 = 15\,V \\ \textit{Reflected output current} \quad & I_2 = 3\,A \\ \textit{Switching frequency} \quad & f_s = 175\,kHz \end{aligned} \tag{9.61}$$

The input current is calculated by imposing an input-output power balance assuming 80% converter efficiency.

The current in the switches is the sum of input inductor and output inductor currents (neglecting the isolation transformer magnetizing inductance). Therefore, the DC switch current is 4.5 A (sum of (9.60) and (9.61)). In order to ensure soft-switching, the switch current must change sign at every cycle, which means that the switch current AC

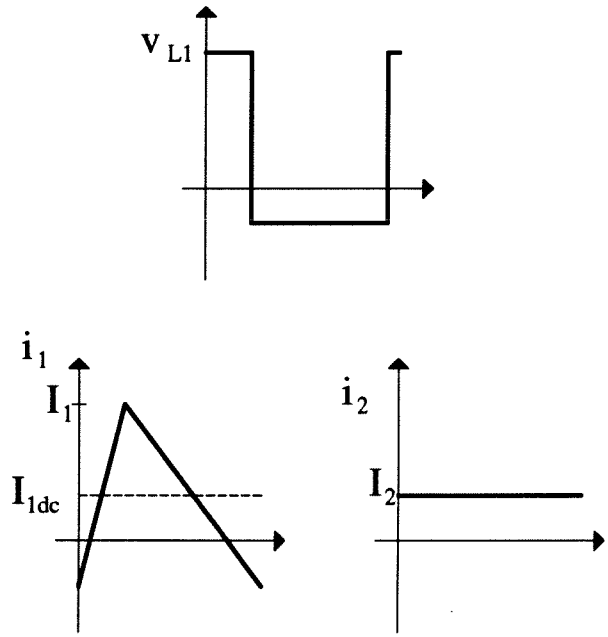

Figure 9.8: Inductor voltages and currents.

component must be bigger than the DC component.

The switch AC current is due to the input inductor only, because the output inductor is designed for zero current ripple. Considering that some contribution to the switch current ripple comes from the transformer magnetizing current, an input inductor ripple amplitude $I_{1\,ripple} = 4.7\,A$ is considered sufficient to ensure soft-switching at full load.

From the waveforms of Fig. 9.8 it is clear that

$$L_1 = \frac{\int_0^{D\,T_s} v_{L1}\,dt}{2I_{1\,ripple}} = \frac{V_g D}{2I_{1\,ripple}\,f_s} = 6.5\mu H$$

and that peak input current is

$$I_1 = I_{1\,DC} + I_{1\,ripple} = 6.2A$$

Summarizing, the design requires

$$\begin{aligned} I_1 &= 6.2A \\ I_2 &= 3A \\ L_1 &= 6.5\mu H \end{aligned} \tag{9.62}$$

The small value of inductance L_1 makes accurate modelling of leakages a prerequisite for successful coupled-inductor design.

9.4.2 Measurement of Leakage and Fringing Reluctance for the Core Used in the Design

The core used for all designs is a UU13 core, which has a cross-section $S = 23\ mm^2$. A saturation flux density $B_M = 0.33T$ is used.

In order to perform the design, it is necessary to determine leakage reluctance $\mathcal{R}_l$ and fringing reluctance $\mathcal{R}_{fring}$. A coupled-inductor structure with nine turns per winding and a spacer gap $x = 0.24\,mm$ is built. Open-circuit inductance is measured to be $L_1 = 8.3\,\mu H$ and short-circuit inductance $L_{1\,short} = 3.9\,\mu H$. From the reluctance model of Fig. 9.1b, it is

$$\begin{aligned} L_1 &= \frac{N^2}{\mathcal{R}_x + \mathcal{R}_x \| \mathcal{R}_l} \\ L_{1\,short} &= \frac{N^2}{\mathcal{R}_x + \mathcal{R}_l} \end{aligned} \tag{9.63}$$

As explained in section 5.5, reluctance $\mathcal{R}_x$ is the parallel combination of the ideal gap reluctance (9.1) and fringing reluctance $\mathcal{R}_{fring}$. From equations (9.63) it is $\mathcal{R}_l = 16\ [1/\mu H]$ and $\mathcal{R}_{fring} = 60\ [1/\mu H]$.

9.4.3 Application of Design Procedures

Finally, the three design procedures are applied to the design specifications of (9.62). Notice that, after the design procedures are completed, the secondary must be reflected back through the 3:1 transformer. Therefore, secondary number of turns N_2 must be a multiple of 3, so that $N_2/3$ is an integer number.

Primary Gap Design In the primary gap case, equation (9.35) gives $N_1 = 10.85$ and for primary gap it is $N_2 = N_1$. The closest integer multiple of 3 is chosen. Therefore,

$$N_1 = N_2 = 12$$

Gap reluctance is calculated from (9.36): $\mathcal{R}_{x1} = 22.1\ [1/\mu H]$. Taking into account fringing reluctance, the required gap is found to be $x_1 = 1\,mm$.

Secondary Gap Design Primary and secondary number of turns are calculated from (9.23) and (9.25) respectively: $N_1 = 7.95$, $N_2 = 20.21$. The closest acceptable numbers are $N_1 = 8$ and $N_2 = 21$ (multiple of 3). Gap reluctance is calculated from (9.24): $\mathcal{R}_{x2} = 25.6\,[1/\mu H]$. After correction for fringing flux, gap is found to be $x_2 = 1.33\,mm$.

Spacer Gap Design To start the spacer gap design it is necessary to determine whether primary or secondary leg saturates first. From condition (9.49), it follows that primary leg saturates first if

$$k_1 > \frac{I_2}{I_1} = \frac{3}{6.2} = 0.48 \tag{9.64}$$

We can assume that primary leg saturates first, complete the design and then check if condition (9.64) is satisfied.

Equation (9.55) and (9.56) give $N_1 = 7.95$ and $N_2 = 10.71$. The closest acceptable numbers are $N_1 = 8$ and $N_2 = 12$.

Since the adjustment of secondary number of turns is substantial, it is possible that zero ripple condition be met with an inductance L_1 significantly different from the desired value. The problem is that the zero-ripple coupled-inductor design is completely determined by N_1 and N_2. With small integer number of turns, inductance L_1 can take only a finite number of values, and in some cases it may be impossible to get the desired inductance. This *"integer number problem"* exists for secondary and spacer gap but not for primary gap, because in that case $N_1 = N_2$.

For the case of spacer gap, the *"integer number problem"* can be clearly seen in the following way. From equations (9.41) and (9.42), it follows that

$$L_1 = \frac{N_1^2\, k_1}{\mathcal{R}_l(1 - k_1^2)} \tag{9.65}$$

with $k_1 = N_1/N_2$.

We can use equation (9.65) to find out which values of inductance L_1 can be obtained using integer number of turns. For $N_1 = 8$ and $N_2 = 12$ it is $L_1 = 4.7\,\mu H$. Primary current ripple would be 38% bigger than the desired value. This design does not appear acceptable due to high AC copper losses.

We could try increasing the primary number of turns to $N_1 = 9$. Equation (9.65) gives $L_1 = 8.68\,\mu H$. This time, primary current ripple would be 75% of the desired value

	Primary Gap	*Sec. Gap*	*Spacer Gap*
N_1	12	8	10
N_2	12	21	15
$N_2' = \frac{N_2}{3}$	4	7	5
gap	$x_1 = 1\ mm$	$x_2 = 1.33\ mm$	$x = 0.27\ mm$

Table 9.1: Summary of three coupled-inductor designs.

and the converter would not operate in soft switching at full load. This also appears unacceptable.

We can try increasing the secondary number of turns to $N_2 = 15$ (closest number multiple of 3). If we pick $N_1 = 10$ we have $k_1 = 0.66$ and equation (9.65) gives $L_1 = 7.5\,\mu H$. This value appears acceptable.

Notice that condition (9.64) is satisfied and therefore primary leg saturates first. Equation (9.43) can be used to calculate peak flux density, which is found to be $B_M = 0.27\,T$, below the value ($B_M = 0.33\,T$) we were designing for.

Equation (9.41) gives gap reluctance $\mathcal{R}_x = 8\ [1/\mu H]$ and after fringing flux correction gap is found to be $x = 0.27\,mm$.

9.4.4 Comparison of Three Design Performance

The three realized designs are summarized in Table 9.1.

Primary windings are realized using two *AWG* 22 wires in parallel with a total cross-section of $0.77\,mm^2$, and secondary winding using a square-cross-section wire with $2.9\,mm^2$ cross-section. The large secondary cross-section is chosen because at full load secondary DC current is $9\,A$.

Table 9.2 shows experimental results with the three designs.

Inductance L_1 is very close to predicted values (max error 10.6%) even if inductance values are fairly small and leakage has a significant role in determining inductance value.

As explained in section 8.2, residual ripple is higher for the primary leg case, where no turns ratio adjustment is made. Another reason for the higher ripple is that the primary

		Primary Gap	*Sec. Gap*	*Spacer Gap*
L_1 $[\mu H]$	*Theory*	6.5	6.46	7.5
	Exp.	6.9	5.9	6.7
	Error	6%	8%	10.6%
Pk-to-Pk Res. Ripple [A]		1.5	0.8	0.8
No-Load losses [W]		10.2	12.2	9.5
Full-Load Efficiency		77%	77%	80%
Radiated Noise [V]		12	125	70

Table 9.2: Comparison of performance of three coupled-inductor designs.

gap design has a smaller secondary number of turns and leakage inductance (that limits residual ripple) increases with the square of the number of turns.

Fig. 9.9 shows main switch voltage and currents i_1 and i_2 for the secondary gap case measured with an AC current probe. Notice that residual ripple current i_2 is mainly due to a fast variation at the turn-off transition. We can conclude that residual ripple is mainly due to *"applied voltage mismatch"* (see section 8.1). The zero ripple condition is met as demonstrated by the fact that current is almost constant for the rest of the switching cycle.

The no-load converter losses and full-load converter efficiency for the three cases are comparable. The primary gap design has bigger primary number of turns and consequently higher AC copper losses. Secondary gap design is suboptimal due to the *"integer number problem"* that forced us to increase number of turns.

Radiated noise was measured moving a phone pickup at a constant distance from the core and recording the highest induced voltage. Radiated noise appears to be the biggest difference among the three design performances. Primary leg gap gives the lowest radiated noise, and secondary gap gives the highest, as expected (see section 5.2).

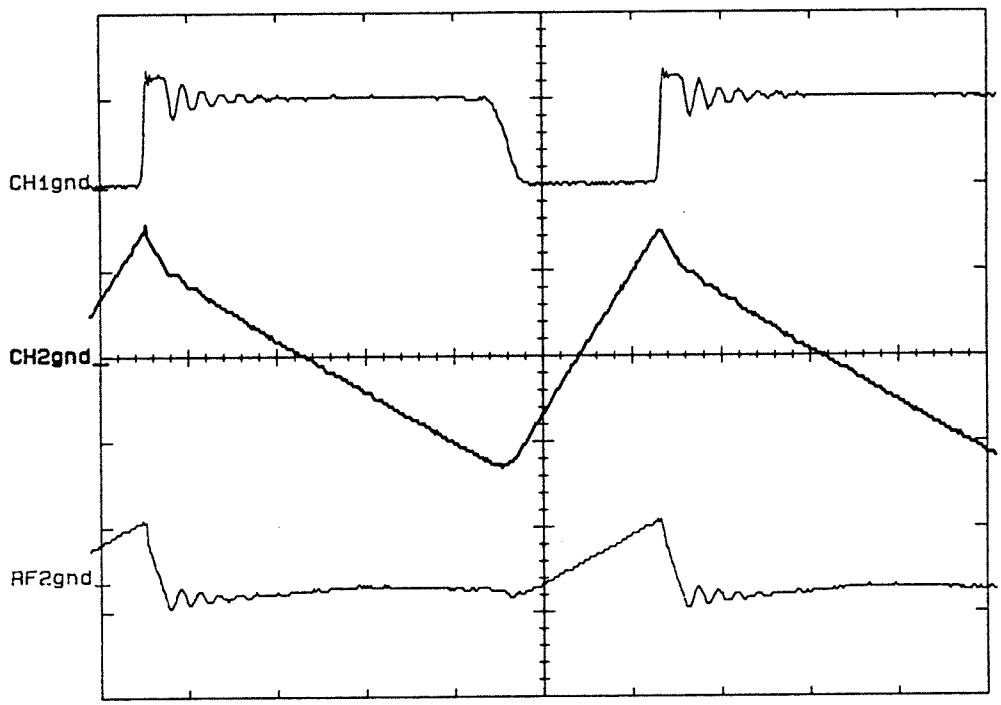

Figure 9.9: Digital scope measurement of main switch voltage and coupled-inductor currents for the secondary gap design. Upper trace: v_{switch}, 50V/div. Medium trace: i_1, 4A/div. Lower trace: i_2, 1A/div. Time scale: 1 μs/div.

Chapter 10

Estimation of Leakage Permeance

In chapter 5 a new reluctance model for coupled-inductor structures was introduced. The model has a single leakage reluctance, constant for a given core. A method to estimate this reluctance based on core geometry is given here. Detailed derivation of the approximate formulas used is given in appendix C.

10.1 Introduction

In chapter 5 it was shown that a UI core with windings on different legs has the reluctance model shown in Fig. 5.3. This model has two gap reluctances, $\mathcal{R}_{x1}$ and $\mathcal{R}_{x2}$, and three leakage reluctances $\mathcal{R}_{l1}$, $\mathcal{R}_{l2}$ and $\mathcal{R}_{l}$. Notice that the reluctance model does not depend on core material. The assumption is that core material relative permeability is so high that the reluctance of flux paths in the core material can be neglected with respect to gap reluctances. In other words core permeability is assumed to be infinite.

Measurements on various cores showed that $\mathcal{R}_{l}$ is usually an order of magnitude smaller than $\mathcal{R}_{l1}$ and $\mathcal{R}_{l2}$. Therefore, these two reluctances were neglected without introducing significant errors. The simplified model is shown in Fig. 5.4b. This model has a single leakage reluctance $\mathcal{R}_{l}$, which is independent of gap arrangement. This reluctance is like a fingerprint for a given core, and it is a function of core geometry only. Once the value of this reluctance is known for a given core, the reluctance model can be used for analysis and design of coupled inductors using that core.

The value of reluctance $\mathcal{R}_{l}$ can be determined from a single set of measurements with any gap arrangements. However, sometimes it may be desirable to obtain an approximate value for this reluctance without a direct measurement. A method to estimate the leakage reluctance $\mathcal{R}_{l}$ from core geometry is described here. This method can be useful

in different ways:

- It can be used for a first-cut design of a coupled-inductor or integrated-magnetics structure.
- It can be used to estimate leakage permeance of custom-designed cores before they are actually built.
- It can be used to better understand the distribution of leakage flux in air. Leakage flux is present in all free space surrounding a core. A natural question to ask is where most of the leakage flux is. This method gives some answer to this question because it breaks up the free space surrounding the core in different regions and estimate leakage flux in each region.

10.2 Estimation Method

For convenience, the leakage flux will be expressed in terms of permeance rather than reluctance. Permeance is the reciprocal of reluctance in the same way as conductance is the reciprocal of resistance. It seems more convenient to use permeances because the estimation method gives the contributions of different regions to the total leakage. In order to find the total leakage, these contributions must be combined together. If reluctances are used, the combined reluctance is equal to the parallel combination of the reluctances of each region, whereas the total permeance is equal to the sum of the permeances of each region.

A brief description of the method is given here. A generic UI core is shown in Fig. 10.1a. Leakage permeance $\mathcal{P}_l$ represents flux linking one of the windings, crossing the gap and closing in air without linking the other winding. Legs AD and BC are covered by windings of highly conducting material that act as shields and prevent flux from leaking through the windings. The approximation is made that legs act as perfect shields so that the same flux links each turn of a winding (notice also that part of the leakage flux through the windings would be more correctly modeled by reluctances $\mathcal{R}_{l1}$ and $\mathcal{R}_{l2}$ of Fig. 5.3, which are neglected here). As a consequence leakage flux is the flux in air between the I piece A–B and the upper part C–D of the U piece. Therefore,

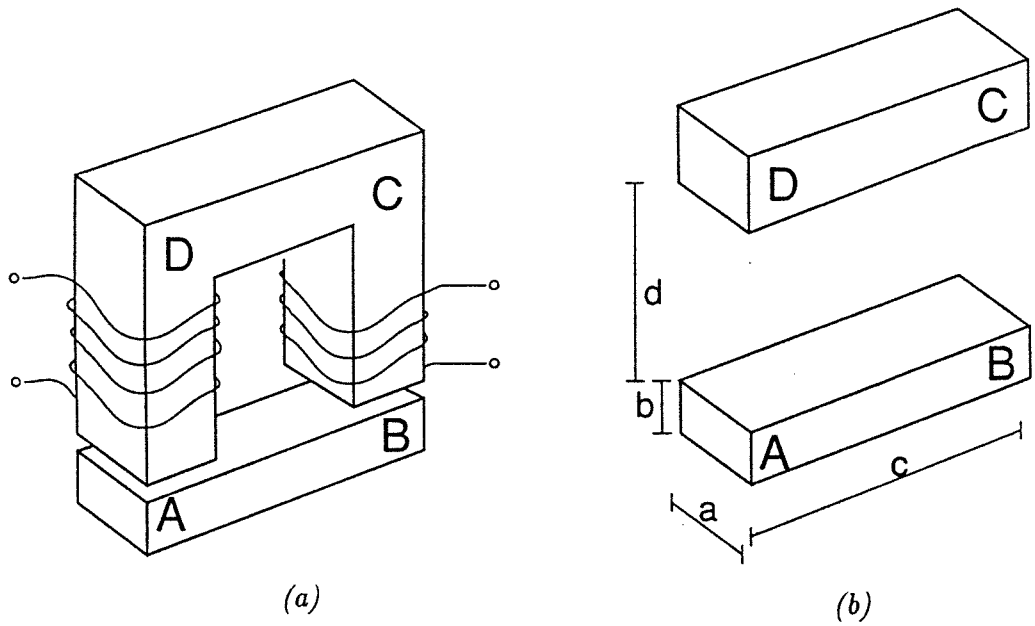

Figure 10.1: To calculate leakage flux a UI core is approximated by two right prisms corresponding to the I piece and the top part of the U piece.

the two legs can be eliminated and leakage flux can be approximated as the flux in air between the two prisms of Fig. 10.1b. The assumption of infinite core permeability implies that each of the prisms of Fig. 10.1b is at a constant magnetic potential. The problem of determining the leakage permeance for the core of Fig. 10.1a is reduced to the problem of determining the permeance of the flux paths between the two prisms of Fig. 10.1b (a minor point: regions physically corresponding to legs AD and BC should not be considered, because there is no leakage flux there).

A method to do this has been proposed by Roters [6] and is also described in Boast [7]. In the following a brief description of this method and the formulas needed for the estimation are given. The formulas are derived in appendix C. The method is called "estimation of the permeance of probable flux paths." The space between and around the two prisms is divided in regions of simple shape. Assumptions are made on the geometry of flux lines in these regions. Approximate formulas for the permeance of these flux paths are found. Adding up the permeances of the different regions gives the total leakage permeance. Fig. 10.2 shows a top view of the prisms of Fig. 10.1b. Only the

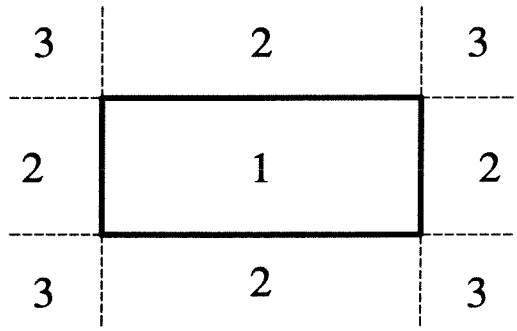

Figure 10.2: Top view of prisms. The free space surrounding the prisms is divided into three regions.

upper face of the upper prism is visible. Region 1 is the space between the prisms. The space surrounding the prisms is divided into region 2 and region 3. The permeances of the different regions are

$$\begin{aligned} &\text{Region 1} \quad \mathcal{P}_1 = \mu_0 \frac{a \cdot c}{d} \\ &\text{Region 2} \quad \mathcal{P}_2 = \mu_0 \left[0.26 + \frac{1}{\pi} \ln \left(1 + \frac{2b}{d} \right) \right] \cdot length \\ &\text{Region 3} \quad \mathcal{P}_3 = \mu_0 (0.308d + b) \end{aligned} \tag{10.1}$$

Dimensions a,b,c,d are shown in Fig. 10.1b. The formula for region 1 is the usual formula for the permeance of a gap. The variable "length" is equal to the perimeter of the rectangle of Fig. 10.2 and its value is 2a+2c.

10.3 Validation of Estimation Method

Finite element simulations To validate this estimation method, finite element simulations were used to calculate permeance of regions 1-2-3. A two-dimensional finite element program called GE2D was used. Finite element simulations of different cross-sections of the core were performed following the approach suggested in [13]. Comparison of estimation, finite element simulations and measurements for a UI60 core are shown in Table 10.1. There is a good agreement between estimation and simulation. This result shows that the estimation method gives a good description of the spatial distribution of leakage flux. It is also interesting to notice that most of the leakage is in region 2. The flux in region 1 accounts for only 20% of the total. That means that most of the leakage

Region	*Estimation* nH	*Simulation* nH	*Measurement* nH
1	37.7	29	213
2	115	110	
3	24.7	33	
Total	177.4	172	213

Table 10.1: Comparison of estimation, finite element simulation and measurement of leakage permeance for the three different regions.

Core	*Estimation* *[nH]*	*Measurement* *[nH]*
EI30	63.4	81
EI40	84.5	107
EI50	105.4	120
EI60	119	141
UU60	146	175
UI45	142	143

Table 10.2: Estimated and measured values of leakage permeance for various standard cores.

flux goes between side surfaces of the core (regions 2 and 3) and not directly from top to bottom (region 1).

Calculation of permeance of standard cores The estimation method is also applied to other cores and comparison with measurements is given in Table 10.2.

Design of custom cores with high or low leakage The estimation method gives leakage permeance as a function of core dimensions. It can be applied to existing core geometries to estimate their leakage or can be used to determine a core geometry that minimizes or maximizes leakage flux. The custom cores that were designed and built are

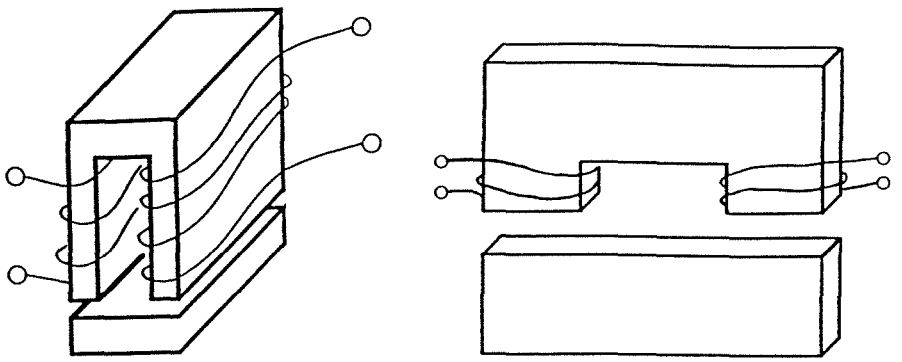

Figure 10.3: Core geometries designed for high leakage permeance (core 1) and low leakage permeance (core 2).

shown in Fig. 10.3. In order to make a fair comparison, the cores had the same cross-section and window area of a UI33 core. Core 1, which was designed for high leakage, is short and fat and core 2, which was designed for low leakage, is tall and skinny. Values of estimated and measured permeances are shown in Table 10.3. The estimation method correctly predicts that core 1 has the highest leakage, and core 2 has the lowest leakage with UI33 core in between. The estimation method appears less precise for these "extreme geometries" than for the standard cores of Table 10.2. However, it correctly predicts that core 1 has the highest leakage, and core 2 has the lowest leakage with UI33 core in between.

	Estimation nH	*Measurement* nH
Core 1	167.7	210
UI33	89.3	130
Core 2	60.6	110

Table 10.3: Estimated and measured values of leakage permeance for custom-designed cores. Core 1 was designed for high leakage, and core 2 was designed for low leakage.

Chapter 11

Conclusions

The goal of this work is to improve understanding of coupled-inductor structures and leakages. Improved leakage models for magnetic structures with air gaps are presented and experimentally verified for the case of two-winding and multiple-winding structures.

It is found that air gap position has a dramatic effect on coupling and on the effective inductances of magnetic structures. This effect is explained and, for the magnetic structures more commonly used in coupled-inductor applications, i.e., UI and UU cores with windings on separate legs, a general model valid for any gap arrangement is presented.

The success of this model is attributed to the fact that it is a "physical model" and it accurately represents fluxes in the magnetic structure. This approach is generalized and a procedure to determine the physical model of any gapped magnetic structure is given. The method is applied to various cases of practical interest and experimentally verified.

A new magnetic structure for coupled inductors is proposed that achieves quasi-zero current ripple without the need for turns ratio adjustment. An additional advantage of this structure is greatly reduced radiated noise.

Design procedures for the most practical zero-current-ripple coupled-inductor structures are presented.

In order to use the reluctance models presented in this work, leakage reluctance values must be determined. A first method to do that is to *measure* them. Another method is to *estimate* them. A simple approximate estimation method is presented and its accuracy is verified through finite element simulations.

Part II

One-Cycle Control of Switching Converters

Chapter 12

Introduction

One-Cycle control is a new control technique that has recently been proposed.

In chapter 13, this control technique is briefly reviewed and application of this technique to Buck, Boost and Ćuk converters is discussed. In the rest of this work the case of a Ćuk converter (a fourth-order system) is considered.

In chapter 14, it is shown that this control technique is particularly advantageous for converters with Buck-like output stage (e.g., Buck converter with input filter, Ćuk converter). In the case of a Ćuk converter, it decouples the output stage from the input stage, allowing their independent design and ensuring rejection of line voltage perturbations. Moreover, by proper design of the output stage, a very fast dynamic response can be achieved. It is also pointed out that the control works in discontinuous conduction mode as well.

In chapter 15 the problem of internal stability of the One-Cycle controlled Ćuk converter is discussed. No previous analytical stability analysis was available. It is shown that the system is stable if some parasitic resistances are in a certain range.

For a typical design the resistances required for stability can be too large to allow an efficient design. Therefore, a modification of the control law that guarantees stability regardless of the value of parasitics is proposed in chapter 16. The dynamics of this control are studied through numerical simulations, and it is found that the modified control has a more damped response, which is a desirable feature.

A disadvantage of this control technique is that the output voltage is only indirectly controlled, so that there is a steady-state error due to parasitics. A solution for this problem is suggested in chapter 17.

Chapter 13

Review of One-Cycle Control

In this chapter One-Cycle control is briefly reviewed. Application of this control technique to Buck, Boost and Ćuk converters is described.

13.1 Control of Switching Converters

DC-DC switching converters are used to convert power from one DC level to another DC level in a controllable way. Different *converter topologies* like Buck, Boost, Buck-Boost and Ćuk converters are used. All these converters have two switches: an active switch S and a passive switch D.

By proper control of the state (open or closed) of the active switch, it is possible to control the power conversion process. In particular, it is often desired to control the output voltage of a converter, and the purpose of the *control circuit* is to control the state of the active switch in such a way to force the output voltage to be equal to a reference value. The active switch is alternatively turned ON and OFF, and the time interval between two successive turn ON (or turn OFF) transitions is called switching period T_s. For various reasons it is desirable to operate a converter at a constant switching period.

Switching period T_s can be divided in two subperiods, ON period and OFF period, characterized by the state of the active switch. *Duty cycle* d is defined as the ratio of ON period over total switching period T_s, and it can have any value between zero (switch always OFF) and one (switch always ON).

The nominal operation of a switching converter involves a *periodic steady-state* with period equal to the switching period.

The control must satisfy both *steady-state* and *dynamic* requirements. In case of output voltage control, the main steady-state requirement is that output voltage be

equal to reference voltage. Since a converter is subjected to inevitable disturbances, such as supply voltage variations and load variations, that cause circuit operation to deviate from nominal, control must guarantee a well-behaved dynamic evolution leading back to the desired steady-state condition.

In this work a control method called One-Cycle Control (OCC) is described. In the next section a brief review of this method is presented.

13.2 One-Cycle Control

One-Cycle Control has been introduced in [18] and [19]. This research effort is a continuation of that work.

In DC-DC converters, whether in steady-state or not, each switch has some average voltage and current through it at each switching cycle. The main idea behind One-Cycle Control is to control the average voltage or current in a switch cycle by cycle, forcing it to be equal to some desired value. It is easier to understand OCC through some example.

Notation To simplify notation all equations in the following will be written for the switching period 0-T_s, with the understanding that the time origin is shifted to the beginning of the period of interest. For example, in this notation the expression

$$\text{Switch } S \text{ ON for } \quad 0 < t < dT_s$$

means

$$\text{Switch } S \text{ ON for } \quad nT_s < t < nT_s + dT_s \qquad n = -\infty, \ldots, -1, 0, 1, \ldots, +\infty$$

13.2.1 Steady-State Operation of a Buck Converter and One-Cycle Control

Steady-state operation of a Buck converter As a first simple example, a Buck converter is discussed. Steady-state voltage waveforms for this converter are shown in Fig. 13.1. Supply voltage V_g is constant. The active switch is turned ON and OFF at a constant duty cycle d. When the active switch is OFF, passive switch D turns on to ensure continuity of inductor current (a different mode of operation called *discontinuous*

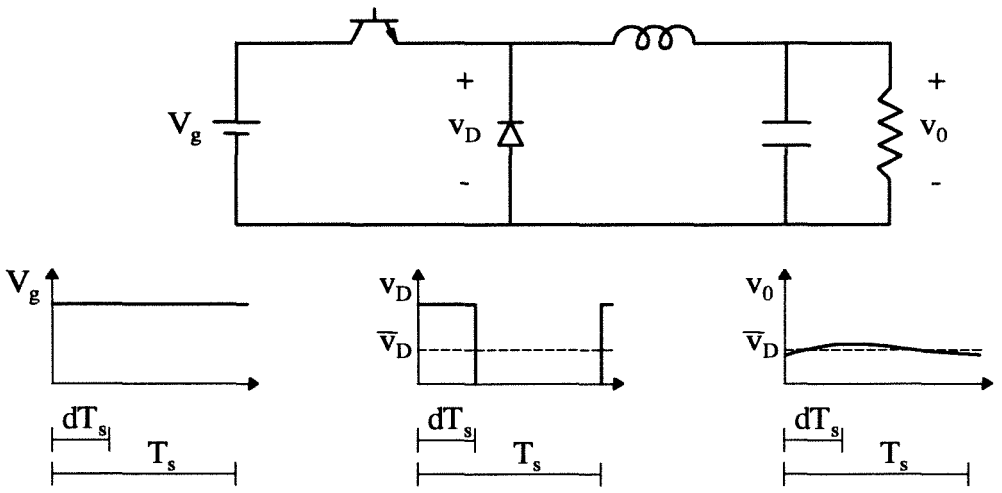

Figure 13.1: Steady-state voltage waveforms in a Buck converter.

conduction mode is discussed in section 14.3.2). As a result of this switching action, diode voltage $v_D(t)$ is

$$v_D(t) = \begin{cases} V_g & 0 < t < dT_s \quad ON\ period \\ 0 & dT_s < t < T_s \quad OFF\ period \end{cases}$$

In steady state the inductor current is the same at the beginning and at the end of a period. This means that the average voltage applied to the inductor in a period is zero (this is called the *volt-second balance condition* and it is used to characterize steady-state of switching converters). Therefore, output voltage v_0 is equal to the average diode voltage, i.e.,

$$v_0 = \overline{v}_D = \frac{1}{T_s}\int_0^{T_s} v_D(t)\,dt = \frac{1}{T_s}\int_0^{dT_s} V_g\,dt = V_g d \tag{13.1}$$

One-Cycle control of a Buck converter Equation (13.1) shows that steady-state output voltage v_0 is equal to the average diode voltage and therefore it can be indirectly controlled by controlling the average diode voltage. In One-Cycle control diode voltage is controlled cycle by cycle and its average value is forced to be equal to the desired output voltage V_{ref} in each cycle. This is done at all times, even if the converter is not in steady-state. A One-Cycle controlled Buck converter is shown in Fig. 13.2. Switch

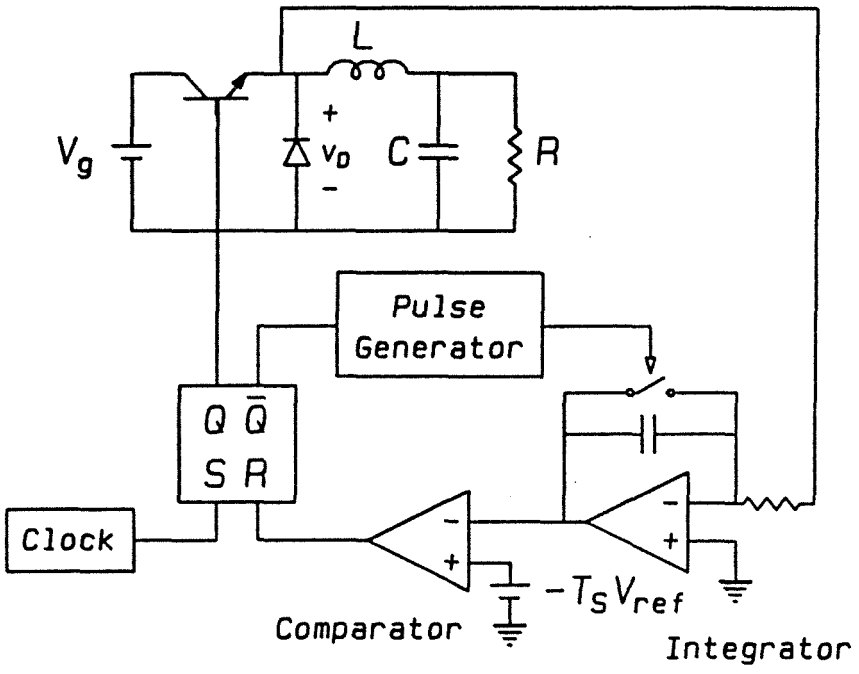

Figure 13.2: One-Cycle controlled Buck converter.

turn-on is decided by a clock, so that switching period T_s is constant. When the switch is on, the line voltage V_g is applied to the diode. The integrator integrates this voltage. When the integral reaches the desired value $V_{ref}T_s$, the comparator switches state and the controller turns off the switch. At the same time the controller sends an impulse to reset the integrator. During the turn-off interval the diode conducts and ideally there is zero voltage across it. The control law is

$$V_{ref} = \frac{1}{T_s}\int_0^{T_s} v_D(t)\,dt = V_g d \tag{13.2}$$

where d is the duty cycle, V_{ref} the reference voltage and v_D the diode voltage. This control law should be interpreted in the sense that the control imposes a value of duty cycle d that satisfies equation (13.2).

Notice that this control is very similar to a standard PWM control with line voltage feed-forward (see however section 14.3.2 for a discussion of One Cycle control in discontinuous conduction mode). The ramp with slope proportional to line voltage V_g used in line voltage feed-forward is in effect an integral of the line voltage. This ramp starts

from zero each cycle in the same way as the integration in One-Cycle control. In both controls the turn-off instant is decided by a comparator which compares the integral with a reference. Similarities with conventional control techniques, however, disappear when One-Cycle control is applied to other converters or even to a Buck converter with input LC filter.

13.2.2 One-Cycle Control of a Boost Converter

The case of a Boost converter is now considered. In steady-state the diode voltage is equal to the difference of output and input voltage. Therefore, the control law is

$$V_{ref} - V_g = \frac{1}{T_s}\int_0^{T_s} v_D(t)\,dt = v_0 d \tag{13.3}$$

As before, the meaning of this control law is that the control selects a duty cycle d that satisfies equation (13.3). Notice that there is a slight abuse of notation in this expression, because output voltage v_0 is not a constant and it cannot be taken out of the integral. However, in a well-designed converter output voltage ripple in one switching cycle is small. The control implementation, shown in Fig. 13.3, is the same as for the Buck converter. The only difference is that the diode is not referred to ground and its voltage must be measured differentially.

13.2.3 One-Cycle Control of a Ćuk Converter

One-Cycle Control can be applied to any other DC-DC converter. However, the control has special advantages in the case of converters with Buck-like output stages, like a Buck converter with input filter and a Ćuk converter. A One-Cycle controlled Ćuk converter is examined here.

A One-Cycle controlled Ćuk converter is shown in Fig. 13.4. This converter has an input filter (or input stage) L_1–C_1 and an output filter (or output stage) L_2–C. During the on-period the energy-transferring capacitor voltage v_{C1} is applied to the diode. Therefore, the control law is

$$V_{ref} = \frac{1}{T_s}\int_0^{T_s} v_D(t)\,dt = v_{C1} d \tag{13.4}$$

The same observations made about control law (13.3) can be repeated here.

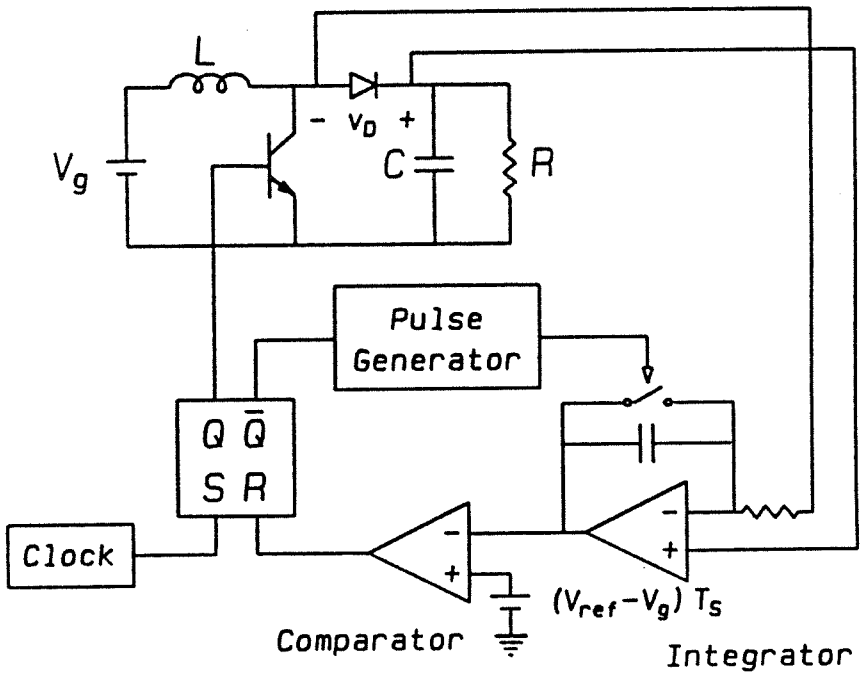

Figure 13.3: One-Cycle controlled Boost converter.

In the rest of this work, One-Cycle control of a Ćuk converter will be studied in detail. An equivalent dynamical model for the output stage of this system is shown in Fig. 13.5. It consists of a controllable voltage source V_{ref} that drives the output filter of the converter. The voltage ripple on the diode can be neglected due to the L_2–C lowpass filter that is designed to reduce this ripple. Notice that the input stage of the converter does not have any effect on the output voltage dynamics. In fact, this dynamical model is identical to the dynamical model for a One-Cycle controlled Buck converter. This is true as long as the input filter dynamics are reasonably well-behaved. If, for example, the energy-transferring capacitor voltage v_{C1} starts oscillating, the control may be unable to apply the desired average voltage to the diode. This internal stability issue will be discussed in chapter 15.

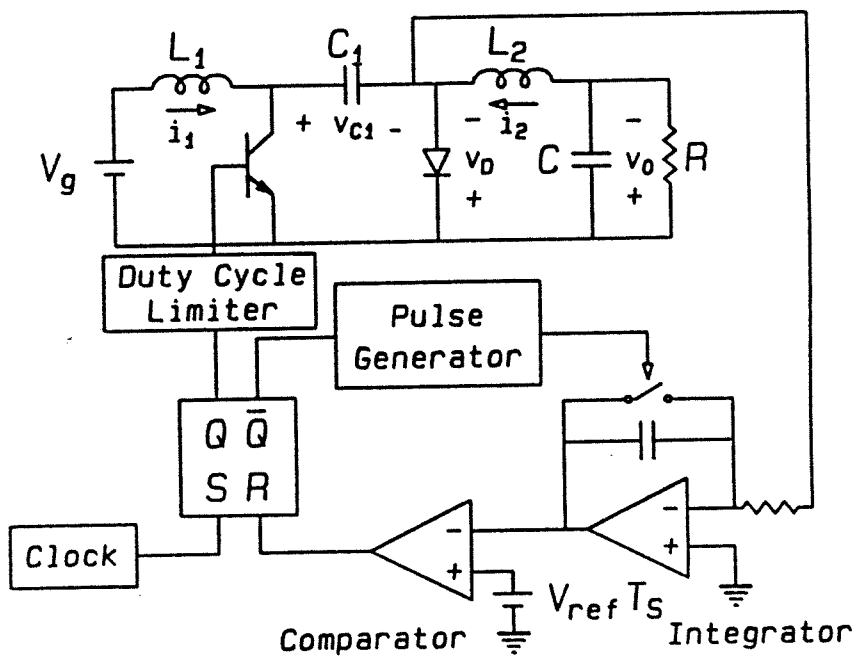

Figure 13.4: One-Cycle controlled Ćuk converter.

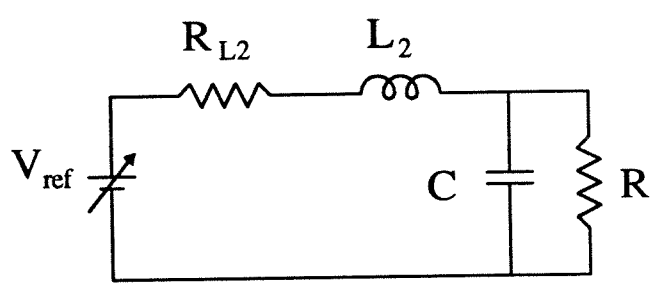

Figure 13.5: Dynamical model for a One-Cycle controlled Ćuk converter.

Chapter 14

Properties of a One-Cycle Controlled Ćuk Converter

In the first section of this chapter some additional interpretation of One-Cycle control applied to a Ćuk converter is given.

In the second section advantages and disadvantages of this control technique are discussed.

In the third section some observations on the implementation of this control technique are presented.

14.1 Interpretations of One-Cycle Control Applied to a Ćuk Converter

Two different interpretations of this control technique can be given.

1. Decoupling. The control decouples the input stage from the output stage of the Ćuk converter. Regardless of what happens in the input stage, the desired average voltage is applied to the diode at each cycle.

2. Partial linearization. A Ćuk converter is a fourth order time-varying system and is described by the following *averaged model* [21]

$$\begin{cases} L_1 \frac{di_1}{dt} = -(1-d)v_{c1} + V_g \\ C_1 \frac{dv_{c1}}{dt} = (1-d)i_1 - d \cdot i_2 \\ L_2 \frac{di_2}{dt} = d \cdot v_{c1} - v_0 \\ C \frac{dv_0}{dt} = i_2 - \frac{1}{R} v_0 \end{cases} \tag{14.1}$$

where duty cycle d is the control variable and it can assume any value between 0 and 1. Notice that in these equations there are three nonlinear terms, $d \cdot v_{c1}$, $d \cdot i_1$

and $d \cdot i_2$. In an averaged sense One-Cycle control imposes the condition

$$v_{c1} d - V_{ref} = 0$$

as shown in equation (13.4). Therefore, the nonlinear term $d \cdot v_{c1}$ in the first and the third equation of (14.1) is forced to be a constant. The control *linearizes* this term. Only the second equation of (14.1) remains nonlinear.

14.2 Advantages and disadvantages of One-Cycle control

At this point, advantages and disadvantages of One-Cycle control are discussed with reference to a Ćuk converter.

A first advantage is that it gives greater freedom in the converter design. If a conventional control technique is used, the input and output filter corner frequencies must be well-separated in order to avoid a very fast 360 degree phase change that would make compensation difficult. No such design constraint exists in the case of One-Cycle control, because this control decouples input and output filter dynamics. This fact was verified in [19].

Another advantage of this control technique is rejection of input line voltage perturbation in one switching cycle. Regardless of perturbations in line voltage, the average voltage applied to the diode each cycle is equal to the reference voltage. Refer to [19] for an extensive discussion and experimental verification of this fact.

Still another advantage is that switching frequency is constant. In other control techniques, like sliding mode control, switching frequency depends on the operating point.

Finally, a very fast dynamic response can be obtained with this control technique. As shown in the dynamical model of Fig. 13.5, the dynamics are solely determined by the converter output filter, which can be designed for fast response. In a conventional control, compensation needed to stabilize the system usually slows down the dynamics of the system.

A disadvantage of One-Cycle control is that in general there is a steady-state output voltage error. This is due to the fact that output voltage is controlled only indirectly by controlling diode voltage. Inductor L_2 of Fig. 13.5 has some parasitic series resistance R_{L2} that causes a DC voltage drop and therefore a load-dependent output voltage error.

Another potential problem is evident from Fig. 13.5. In an efficient design the lowpass filter L_2–C has a high quality factor Q that can cause overshoot and lightly damped oscillations in the dynamic response. This problem is particularly severe at light load.

14.3 Implementation of One-Cycle control

Implementation of One-Cycle control for a Ćuk converter is shown in Fig. 13.4. The flip-flop that controls the switch is set by a clock signal and reset when the integral of the diode voltage reaches the desired value. When this happens, the pulse generator sends a short pulse to reset the integrator. The flip-flop output does not directly drive the converter switch, but goes through a *duty cycle limiter*. It is worth discussing the reasons for the introduction of the duty cycle limiter and for the use of impulsive reset of the integrator (the *pulse generator* of Fig. 13.4 is not strictly necessary: it could be replaced by a short keeping the integrator output at zero for the entire OFF period).

14.3.1 Duty Cycle Limiter

The duty cycle limiter ensures a minimum OFF time in each cycle. This is needed for the following reason. At startup, capacitor voltage v_{c1} is zero. Therefore, when the clock turns on the transistor, no voltage is applied to the diode. The integrator output cannot reach the reference value and, if there is no duty cycle limitation, the transistor never turns off. Energy is stored in the input inductor, but is never delivered to the output.

14.3.2 Impulsive Reset of Integrator and Discontinuous Conduction Mode

The pulse generator allows instantaneous reset of the integrator at the beginning of the off-period. Integration restarts immediately after the pulse and ideally (for infinitely short pulses) it continues for the entire period until another reset pulse arrives. If, for example, the pulse generator were replaced by a short, the integrator would be off for the entire off-period.

Using a pulse generator gives the following advantages:

1. It gives complete decoupling between input and output stages.

2. It ensures proper control in discontinuous conduction mode.

These advantages are briefly discussed here.

1. **Decoupling of input and output stages.** A real diode has some voltage drop during conduction. This voltage is taken into account by the control if the integration continues on during the off-period also. If this voltage drop is not taken into account, the diode resistance, which has the current $i_1 + i_2$ during the off-period, introduces a coupling between input and output stages.

2. **Discontinuous conduction mode.** Fig. 14.1a-b shows the diode voltage waveform in Continuous Conduction Mode (CCM) and Discontinuous Conduction Mode (DCM) respectively. In CCM (Fig. 14.1a) the voltage during the off-period is zero (or very close to zero), and therefore changes little if the pulse generator is replaced by a short. In DCM (Fig. 14.1b) when the diode current drops to zero, the diode stops conducting and the output voltage v_0 (dashed line) appears across the diode (the oscillatory waveform during interval d_3 is a more realistic representation of converter behavior in DCM, and it is due to oscillation between diode capacitance and the parallel combination of inductors L_1 and L_2). The output voltage is equal to the average diode voltage over the entire period. In this case, if the pulse generator is replaced by a short, the control causes an output voltage error, as shown in Fig. 14.1b, because only the diode voltage during the on-period is integrated and taken into account by the control. This is experimentally verified in Fig. 14.2. The upper trace shows the diode voltage and the lower trace shows the integrator output. The dotted line shows the output of the integrator without the pulse generator and the shaded area shows the voltage that would not be integrated in that case.

   The necessity of integrating the diode voltage during the entire period in discontinuous conduction mode has already been discussed in [19].

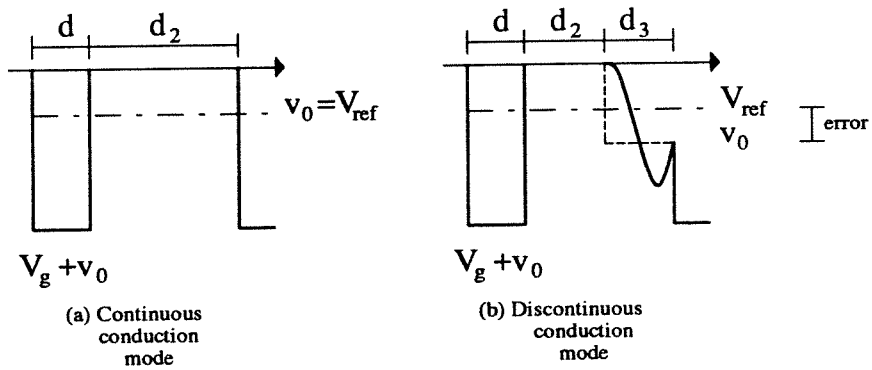

Figure 14.1: Diode voltage waveform (a) in continuous conduction mode and (b) in discontinuous conduction mode.

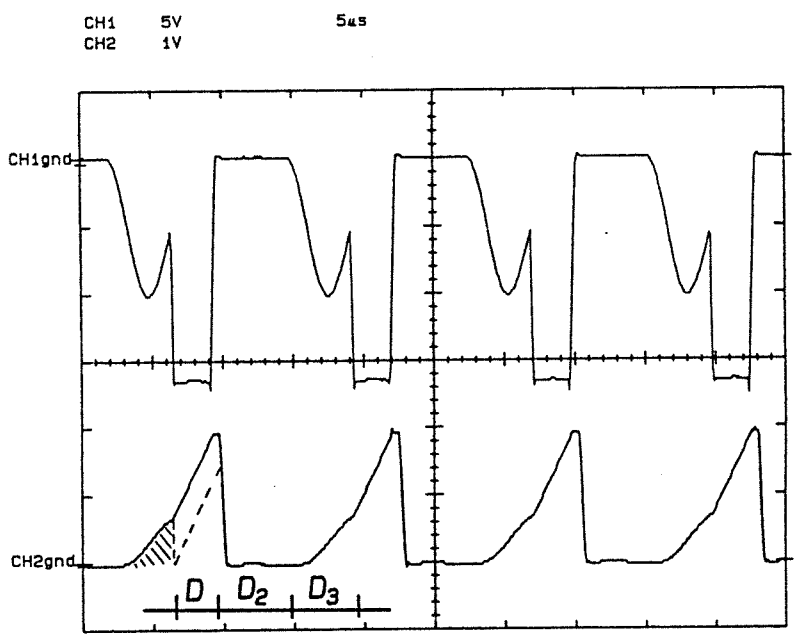

Figure 14.2: Measurement of diode voltage (upper trace) and integrator output (lower trace).

14.4 Experimental Prototype

The prototype Ćuk converter used for experiments has the following component values:

$$\begin{array}{lll} L_1 = L_2 = 2700\mu H & C_1 = 60\mu F & C = 1000\mu F \\ R = 20\Omega & R_{L1} = 0.33\Omega & R_{L2} = 0.33\Omega \\ R_{C1} = 0.24\Omega & V_g = 10V & f_s = 60KHz \end{array} \tag{14.2}$$

Chapter 15

Stability Analysis of One-Cycle Control

Until now, no quantitative stability analysis of One-Cycle control was available. The output stage, whose dynamic model is shown in Fig. 13.5, is always stable, since it is a passive filter driven by a controllable voltage source. On the contrary, it is not clear if the input stage is stable. If the input stage is unstable, One-Cycle control may be unable to reject oscillations in the energy-transferring capacitor voltage, which may show up in the output.

The small-signal stability analysis presented here follows the lines of State-Space Averaging [20].

15.1 Small-Signal Stability Analysis of One-Cycle Control

The averaged dynamical model of a Ćuk converter is described by the following differential equations

$$\begin{vmatrix} \frac{di_1}{dt} \\ \frac{dv_{C1}}{dt} \\ \frac{di_2}{dt} \\ \frac{dv_0}{dt} \end{vmatrix} = \begin{vmatrix} \frac{-R_{L1}-R_{C1}(1-d)}{L_1} & -\frac{1-d}{L_1} & 0 & 0 \\ \frac{1-d}{C_1} & 0 & -\frac{d}{C_1} & 0 \\ 0 & \frac{d}{L_2} & \frac{-R_{L2}-R_{C1}d}{L_2} & -\frac{1}{L_2} \\ 0 & 0 & \frac{1}{C} & -\frac{1}{RC} \end{vmatrix} \begin{vmatrix} i_1 \\ v_{C1} \\ i_2 \\ v_0 \end{vmatrix} + \begin{vmatrix} \frac{V_g}{L_1} \\ 0 \\ 0 \\ 0 \end{vmatrix} \tag{15.1}$$

where R_{C1} is the parasitic series resistance of energy-transferring capacitor C_1 and R_{L1} and R_{L2} are the parasitic series resistances of input and output inductor respectively. These equations are identical to (14.1) with the only difference that parasitic resistances R_{C1}, R_{L1} and R_{L2} are introduced. The reason why these second-order terms are considered will become apparent as the analysis unfolds. Taking into account the parasitics,

control law (13.4) becomes

$$(v_{C1} - R_{C1} i_2) d - V_{ref} = 0 \tag{15.2}$$

The analysis follows the following steps:

1. Equations (15.1) and (15.2) are perturbed. DC quantities are represented by capital letters and perturbed quantities are written as low-case with a hat. For example, perturbed duty cycle is

$$d = D + \hat{d}$$

2. The resulting equations are divided in DC and AC (dynamic) parts. The DC equations determine the operating point, and the AC equations represent dynamic behavior around the operating point.

3. Dynamic equations are nonlinear due to the presence of terms containing the product of AC terms. Under a small-signal assumption, these terms are neglected resulting in linear equations.

4. In this analysis parasitic resistances are supposed to be small, so terms proportional to these quantities are neglected when compared to terms coming from the "ideal" converter. Moreover, steady-state currents and voltages are expressed as a function of steady-state duty cycle D, load resistance R and supply voltage V_g.

As an example, this procedure is applied to control equation (15.2).

1. Perturbation gives

$$[(V_{C1} + \hat{v}_{C1}) - R_{C1}(I_2 + \hat{i}_2)](D + \hat{d}) - V_{ref} = 0$$

2. DC and AC equations are

$$\begin{aligned} &(V_{C1} - R_{C1} I_2) D - V_{ref} = 0 && \textit{DC equation} \\ &(V_{C1} - R_{C1} I_2)\hat{d} + D\hat{v}_{C1} + \hat{v}_{C1}\hat{d} - D R_{C1}\hat{i}_2 - R_{C1}\hat{i}_2\hat{d} = 0 && \textit{AC equation} \end{aligned} \tag{15.3}$$

3. Equation (15.3) is linearized, giving

$$(V_{C1} - R_{C1} I_2)\hat{d} + D\hat{v}_{C1} - D R_{C1}\hat{i}_2 = 0 \tag{15.4}$$

4. In equation (15.4) the term $R_{C1}I_2$ is neglected with respect to V_{C1}. For the DC equations obtained from equations (15.1), it follows that DC voltage V_{C1} is written as $V_{C1} = V_g/(1-D)$. With these two changes, equation (15.4) becomes

$$\frac{V_g}{1-D}\hat{d} + D\hat{v}_{C1} - DR_{C1}\hat{i}_2 = 0 \tag{15.5}$$

This is the AC small-signal control equation.

At the end of this procedure we have algebraic equation (15.5) and four small-signal differential equations obtained from (15.1).

Equation (15.5) is then substituted into the other four perturbed equation to eliminate perturbed duty cycle $\hat{d}$. The resulting equations are

$$\begin{vmatrix} \frac{d\hat{i}_1}{dt} \\ \frac{d\hat{v}_{C1}}{dt} \\ \frac{d\hat{i}_2}{dt} \\ \frac{d\hat{v}_0}{dt} \end{vmatrix} = \underbrace{\begin{vmatrix} -\frac{R_{L1}+R_{C1}(1-D)}{L_1} & -\frac{1}{L_1} & \frac{R_{C1}D}{L_1} & 0 \\ \frac{1-D}{C_1} & \frac{1}{C_1}\frac{D^2}{(1-D)R} & -\frac{D}{C_1} & 0 \\ 0 & 0 & \frac{-R_{L2}}{L_2} & -\frac{1}{L_2} \\ 0 & 0 & \frac{1}{C} & -\frac{1}{RC} \end{vmatrix}}_{A} \begin{vmatrix} \hat{i}_1 \\ \hat{v}_{C1} \\ \hat{i}_2 \\ \hat{v}_0 \end{vmatrix} \tag{15.6}$$

As mentioned above, this procedure is similar to State-Space Averaging. Notice, however, that equations (15.6) describe the small-signal *closed-loop* behavior of the One-Cycle controlled Ćuk converter.

At this point, an interesting observation can be made. The system matrix A can be partitioned in four 2x2 matrices

$$A = \begin{vmatrix} A_{11} & A_{12} \\ A_{21} & A_{22} \end{vmatrix}$$

Notice that $A_{21} = 0$. Therefore, the eigenvalues of A are simply the eigenvalues of A_{11} and A_{22}. This is just a consequence of the decoupling of input and output stages performed by One-Cycle control. The eigenvalues of A_{22} are the poles of the output filter. The control has no effect on them. This is consistent with the dynamical model of Fig. 13.5.

Defining parasitic equivalent resistance R_p as

$$R_p = R_{L1} + R_{C1}(1-D)$$

the eigenvalues of A_{11} are the roots of the equation

$$\lambda^2 + \lambda\left(\frac{R_p}{L_1} - \frac{1}{C_1}\frac{D^2}{1-D}\frac{1}{R}\right) + \left(\frac{1-D}{L_1C_1} - \frac{1}{L_1C_1}\frac{D^2}{1-D}\frac{R_p}{R}\right) = 0 \qquad (15.7)$$

Routh criterion says that the roots of the second order equation above are in the left half plane if and only if the two terms in parenthesis are positive. Defining the characteristic impedance of the input filter as

$$R_n = \sqrt{\frac{L_1}{C_1}}$$

the stability conditions are

$$R_p < \frac{(1-D)^2}{D^2}R \qquad (15.8)$$

$$R_p > \frac{D^2}{1-D}\frac{R_n^2}{R} \qquad (15.9)$$

At this point some important observations can be made. First of all, inequality (15.8) is satisfied in a normal design: parasitic resistance R_p is smaller than the reflected load resistance. Therefore, attention can be focused on inequality (15.9). Notice that this condition is not satisfied in the ideal case (R_p=0). An ideal 100% efficient Ćuk converter *is always unstable* under One-Cycle control. However, in a real-life converter R_p has a non-zero value. Since $D^2/(1-D)$ is a monotonically increasing function for $0 < D < 1$, condition (15.9) puts an upper limit on the duty cycle for a given value of R_{L1} and R_{C1}. As a practical example, let us take

$$L_1 = 100\mu H \quad R = 1\Omega$$
$$C_1 = 10\mu F \quad D = 0.5$$

The stability condition (15.9) becomes

$$R_{L1} + 0.5R_{C1} > 5\Omega$$

Such a big value of parasitic resistance may be unacceptable for efficiency reasons. Therefore, it is desirable to find a way to stabilize the system regardless of the value of R_p. This is discussed in chapter 16.

In the previous analysis, parasitic resistances of the switches may also be introduced. Equations (15.1) and (15.2) would need to be modified. However, it turns out that they contribute only second-order terms to stability conditions (15.8) and (15.9), which remain correct to a first order.

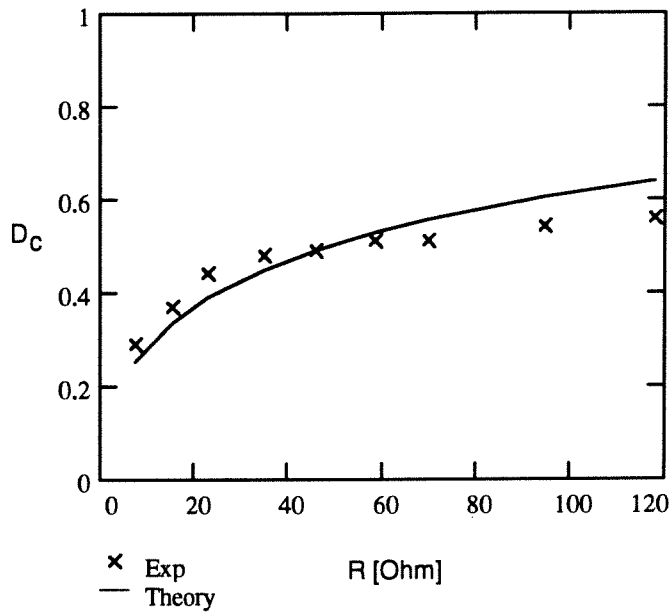

Figure 15.1: Critical duty ratio D_c as a function of load R: theoretical predictions and experimental results.

15.2 Experimental Verification of Stability Condition

Stability condition (15.9) is experimentally verified as follows. For a certain value of load R, equation (15.9) taken as an equality gives a critical duty cycle D_c that is at the boundary between stability and instability. This critical duty cycle is experimentally obtained by slowly increasing the reference voltage until instability occurs. This experiment is performed for different values of load R. Fig. 15.1 shows critical duty ratio D_c as a function of load resistance R. Continuous line represents theoretical predictions given by (15.9) and rectangles represent experimental measurements.

Chapter 16

Modified One-Cycle Control

In the previous chapter it was shown that a One-Cycle controlled Ćuk converter is unstable in the ideal case. In the nonideal case, the system is stable if the parasitic resistance R_p is in a certain range given by equation (15.9). The question arises whether it is possible to modify the control so that stability is guaranteed independently of the value of R_p. This can be accomplished if an additional term proportional to the input inductor current error is introduced in the control equation.

In the first section the modified control law is introduced and some sufficient stability conditions presented.

In the second section the dynamics of modified One-Cycle control are studied numerically.

In the third section some aspects of practical implementation of this modified control are discussed.

16.1 Modified One-Cycle Control Law and Sufficient Stability Conditions

The following modified control law is suggested:

$$v_{C1}d - V_{ref} + K_1(i_1 - I_{1ref}) = 0 \tag{16.1}$$

where i_1 is the input inductor current, I_{1ref} is the operating point input inductor current and K_1 is a constant gain. Control law (16.1) will be referred to as *modified One-Cycle control* and control law (13.4) as *standard One-Cycle control*. For this analysis the same procedure used in chapter 15 is followed. In this case, parasitic resistances are not included, because they are not needed for the stability analysis. The linearized equations

of the controlled system are

$$\begin{vmatrix} \frac{d\hat{i}_1}{dt} \\ \frac{d\hat{v}_{C1}}{dt} \\ \frac{d\hat{i}_2}{dt} \\ \frac{d\hat{v}_0}{dt} \end{vmatrix} = \underbrace{\begin{vmatrix} -\frac{K_1}{L_1} & -\frac{1}{L_1} & 0 & 0 \\ \frac{1}{C_1}\left(1-D+\frac{D}{1-D}\frac{K_1}{R}\right) & \frac{1}{C_1}\frac{D^2}{(1-D)R} & -\frac{D}{C_1} & 0 \\ -\frac{K_1}{L_2} & 0 & 0 & -\frac{1}{L_2} \\ 0 & 0 & \frac{1}{C} & -\frac{1}{RC} \end{vmatrix}}_{A} \begin{vmatrix} \hat{i}_1 \\ \hat{v}_{C1} \\ \hat{i}_2 \\ \hat{v}_0 \end{vmatrix} \tag{16.2}$$

Obviously equation (16.2) reduces to equation (15.6) for K_1=0. In the first equation of (16.2), K_1 acts as a resistance in series with inductor L_1. Moreover, there is a $-K_1\hat{i}_1/L_2$ term in the third row, so that the system cannot be broken up in two parts as (15.6). In order to study stability, the entire fourth-order system must be studied. This can be done using the Routh criterion. Unfortunately, the stability conditions are very complicated and do not give much useful information. However, the following fact can be proven by assuming K_1 big and neglecting all terms which do not contain K_1.

> **Fact:** Any Ćuk converter is stabilized by control law (16.1) for K_1 sufficiently big.

Proof of this fact is given in Appendix D.

This result provides two useful pieces of information. First of all, it says that any Ćuk converter with any component values can be stabilized by control law (16.1). Moreover, it says that increasing the gain K_1 improves stability.

In the case of a third order Ćuk converter (output capacitor C=0), the following sufficient stability condition can be derived

$$K_1 > \frac{D^2}{1-D}\frac{R_n^2}{R} \tag{16.3}$$

Proof of this fact is given in Appendix E. This condition is the same as the condition on R_{L1} in equation (15.9).

16.2 Dynamics of Modified One-Cycle Control

The introduction of the input inductor current term in control law (16.1) has a significant effect on the dynamics of the system. The equivalent model of Fig. 13.5 is not

valid any more, because the input inductor current is used in determining the control. Input and output stages are not decoupled any more and a perturbation of the line voltage has an effect on the output. Three main questions need to be answered:

1. How is the dynamics of the system modified?

2. It has been shown in the previous section that a minimum value of K_1 is needed for stability. How does an increase in K_1 modify the dynamics of the system?

3. How does the relative position of the input and output filter corner frequencies affect the dynamics?

Qualitative answers to these questions are obtained through numerical simulation. The converter specifications are the same as in (14.2) except that C_1=100μF.

1. Modified dynamics. Fig. 16.1 shows the simulated response to a step change in reference voltage. The output filter has a quality factor Q=9 and, therefore, in the case of standard One-Cycle control, the response would have an overshoot 80% of the step amplitude. On the contrary, the response of Fig. 16.1 is monotonic. The conclusion is that the new term in the control has a damping effect on the dynamics. This damping slows down somewhat the dynamic response of the system but has the positive effect of reducing overshoot and oscillations.

2. Effect of variation of K_1. Fig. 16.2 shows a plot of the rise time t_r versus K_1. The rise time increases from $16ms$ to $25ms$ as K_1 goes from 15 to 190. Notice that, as K_1 increases, the rise time approaches a constant value. This is due to the fact that, for K_1 big, equation (16.1) becomes approximately

$$i_1 \approx I_{1ref}$$

   When the step is applied, i_1 jumps to the new reference value and stays there for the entire transient.

3. Effect of variation of input filter corner frequency. The value of energy-transferring capacitor was varied between $0.1 \cdot C$ and $100 \cdot C$, where C is the output capacitor. Fig. 16.3 shows a plot of rise time versus C_1/C. Since $L_1 = L_2$ the quantity

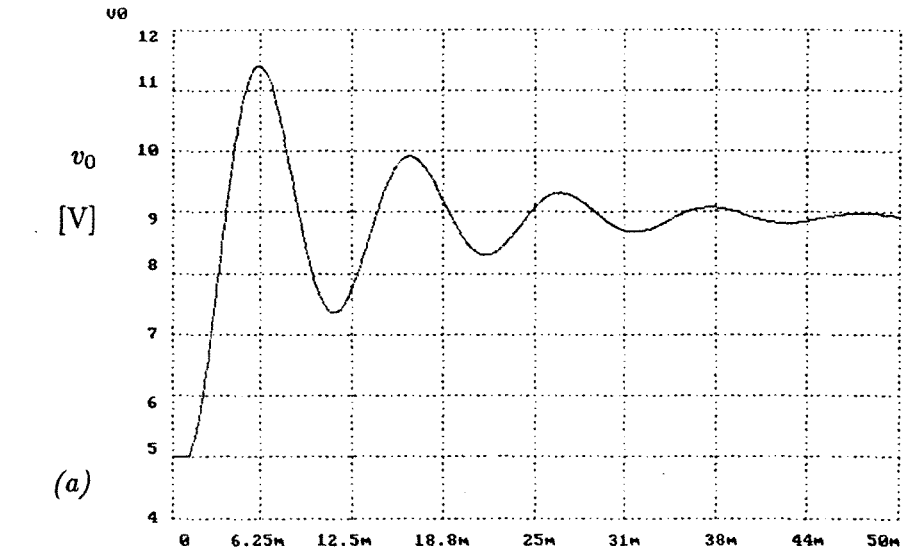

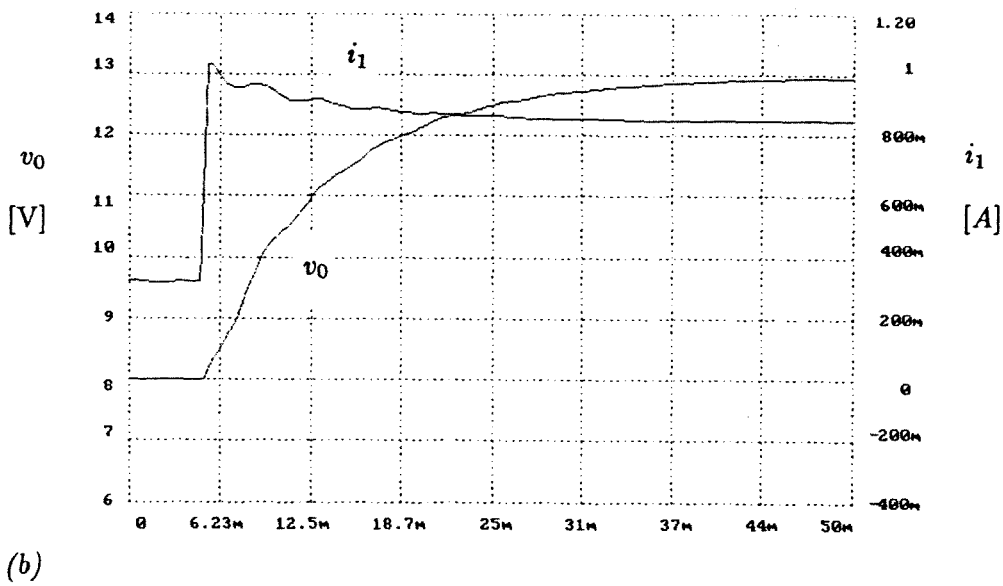

Figure 16.1: Response to load step change in reference voltage with conventional One Cycle control (a) and with modified One-Cycle control for K_1=30 (b). Notice that modified One Cycle control has a well-damped response, whereas standard One Cycle control has significant overshoot.

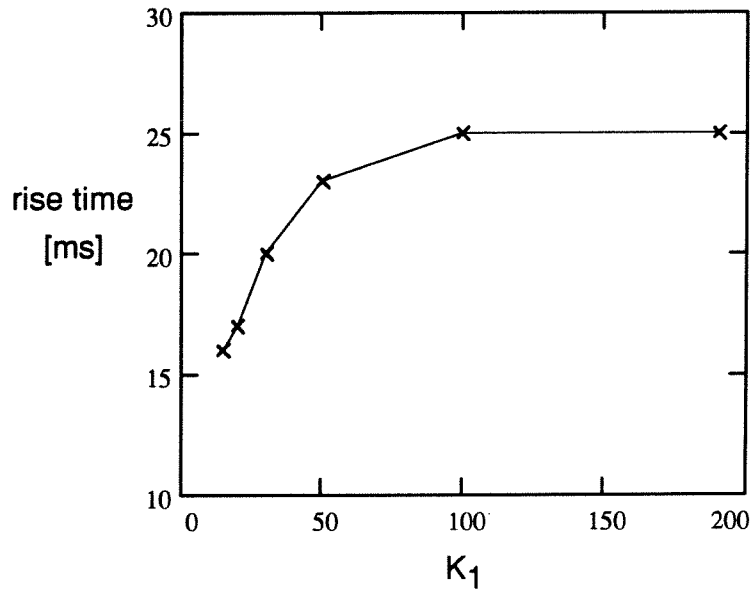

Figure 16.2: Rise time t_r versus gain K_1.

C_1/C gives a measure of the relative positions of input and output filter corner frequencies. As long as $C_1 < C$ (input filter "faster" than output filter), rise time is approximately constant. On the other hand, for $C_1 > C$ (input filter "slower" than output filter), rise time increases as C_1 increases.

16.3 Practical Realization of the Control: Highpass Filter for i_1

In a practical realization of control law (16.1), a problem arises because the desired input inductor current I_{1ref} is not known. It could be calculated from an input–output power balance as

$$I_{1ref} = \frac{v_0^2}{RV_g}$$

but such a calculation involving multiplications is complicated and expensive.

A solution is to use a highpass filter to get rid of the DC part of i_1. Control law (16.1) becomes

$$v_{C1}d - V_{ref} + K_1 \frac{sT}{1+sT} i_1 = 0 \tag{16.4}$$

In (16.4) there is a new free parameter T, which determines the corner frequency of the highpass filter. Too high a corner frequency will cause instability, and too low a value

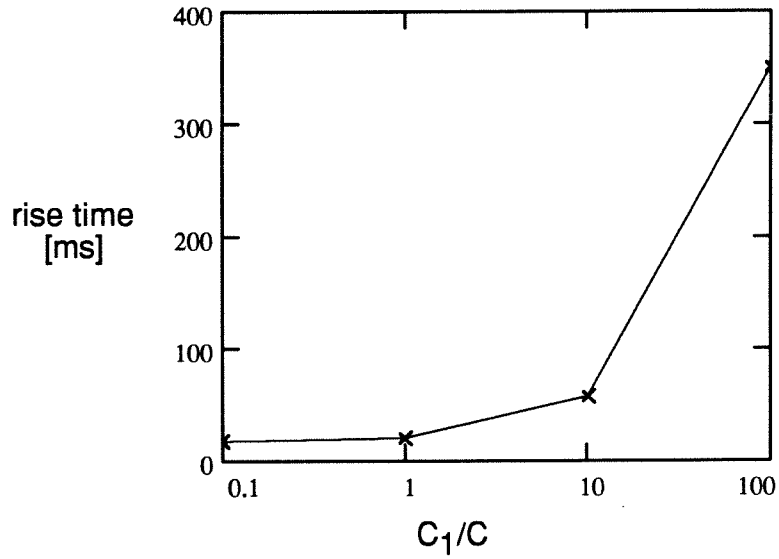

Figure 16.3: Rise time t_r versus C_1/C.

will slow down the response of the system with respect to control law (16.1). With an appropriate choice of filter corner frequency, control law (16.1) and control law (16.4) give very similar dynamic behavior of the controlled converter. To demonstrate this, experimental results using control law (16.4) are compared with simulations using control law (16.1). Output voltage v_0 and input inductor current i_1 are shown in Fig. 16.4 and 16.5 for a reference voltage step from $4V$ to $9V$. For both simulation and experiment, it was K_1=12. For the experiment, the corner frequency was chosen to be $30Hz$. Notice the similarity of the waveforms.

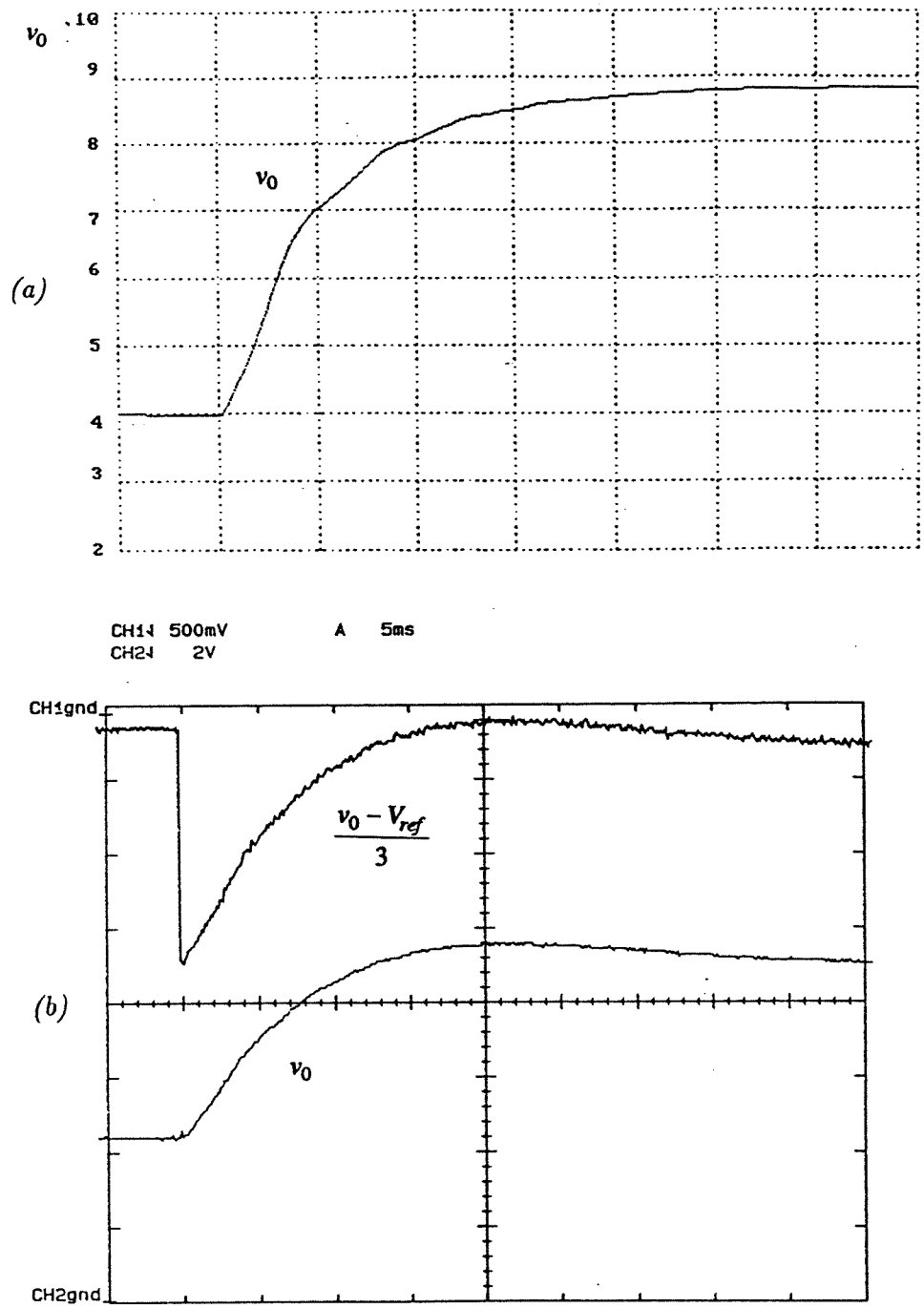

Figure 16.4: Output voltage response to step change in reference voltage, (a) simulation and (b) experiment.

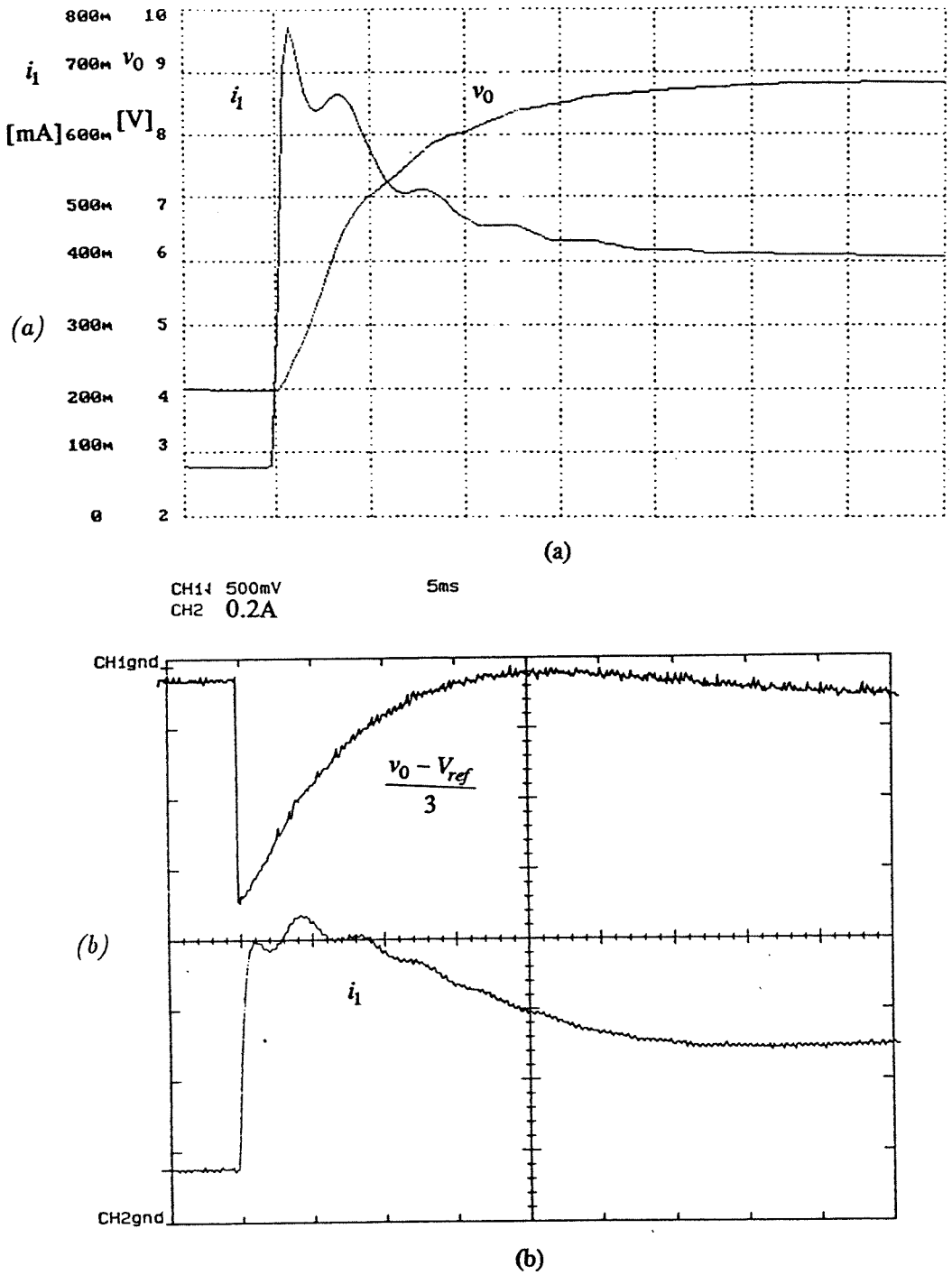

Figure 16.5: Input inductor current response to step change in reference voltage, (a) simulation and (b) experiment.

Chapter 17

Elimination of Steady-State Output Voltage Error

As explained in section 14, the parasitic inductor resistance R_{L2} causes a steady-state output voltage error. If Modified One-Cycle control is used, another possible cause of output voltage error is that the high-pass-filtered current term in control equation (16.4) may have a DC component due to noise.

Whatever the cause, this error can be corrected by introducing a term proportional to the integral of the output voltage error in the control law. Equation (16.4) becomes

$$v_{C1}d - V_{ref} + +K_1\frac{sT}{1+sT}i_1 + K\int(v_0 - V_{ref})\,dt = 0 \qquad (17.1)$$

where K is a constant. The value K can be chosen small enough so that the dynamic response is not affected. The practical implementation of this control law is straightforward. The same modification can be applied to One-Cycle control law (13.4).

Fig. 17.1a-b show the response to a load step change from 100Ω to 20Ω without and with the additional correction. The upper trace represents output voltage error (scaled by a factor of 3), and the lower trace represents the output inductor current. The *CH1 gnd* and *CH2 gnd* signs show the ground levels for channel 1 and channel 2 respectively. In Fig. 17.1a (control law (16.4)) the output voltage error before the transient is $45mV$ and after the transient is $100mV$. The increased error is due to the additional current through R_{L2}. In Fig. 17.1b (control law (17.1)) both before and after the transient, the output voltage error is zero. In this case, the value chosen for K (K=250) is big enough to have some effect on the system dynamics. The response is faster but more oscillatory. If a smaller value of K were chosen, the transient would be less affected, but output voltage error correction would take more time.

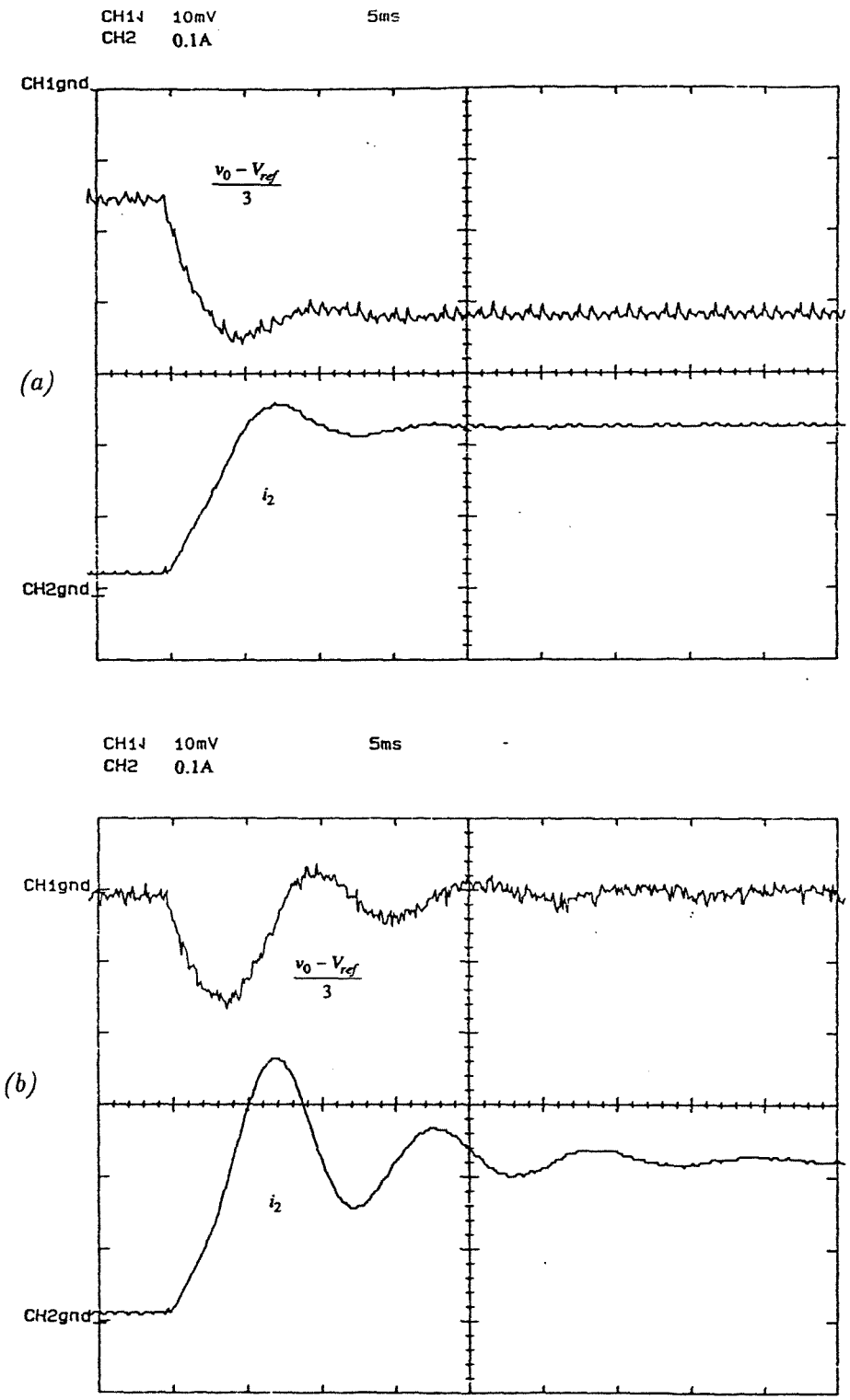

Figure 17.1: Load step change (a) without correction for output voltage error and (b) with correction.

Chapter 18

Conclusions

In this work issues regarding One-Cycle control of switching converters are discussed. The generality of this control technique is demonstrated by its application to Buck, Boost and Ćuk converters. Moreover, implementation of this control is fairly simple.

One-Cycle control gives complete rejection of line perturbation, decouples input and output stages, which can be designed independently, and gives fast dynamic response.

A method to eliminate output voltage error, which is a problem of this control method, is suggested.

A small-signal stability analysis is performed that shows that system stability depends on the value of some parasitic resistances. Since resistance values required for stability can be too large for an efficient design, a modified control is suggested that is stable regardless of the value of these resistances. The stabilization is achieved by feeding back the input inductor current. It is shown through numerical simulation that the modification has the beneficial effect of damping the dynamic response of the system.

Appendix A

Orthogonal Winding Coupling

In this appendix an unusual transformer structure is studied. Even if it is unclear whether this kind of structure could be of any practical use, this problem appears to be an interesting exercise in magnetic circuits that puts to a test one's understanding of coupled magnetic circuits and transformers.

The beauty of this problem lies in the fact that, although the structure is fairly simple, completely different answers can be given depending on the *way* one looks at it. People with diverse backgrounds tend to look at this problem differently and give surprisingly disparate answers. As a matter of fact, this project started from a controversy on the correct answer to this problem.

There is a strong similarity between this problem and the gapped coupled magnetic circuits studied in the first part of this thesis. In both cases it is of paramount importance to understand and model leakage fluxes, and in both cases the behavior of the structure is very "directional," i.e., it changes completely depending on whether the primary side or the secondary side is driven.

A.1 Problem Statement

The transformer structure is shown in Fig. A.1. It consists of two windings. The first winding, also called primary winding, has $N_1 = 100$ turns and is wound around a toroid in a solenoidal fashion. The toroid is made of non-magnetic material. The case of a toroid of high-permeability material will be considered later. The second winding, also called secondary winding, has a single turn and runs along the center of the toroid and is therefore "inside" the primary winding.

Suppose a signal v_1 is applied to the primary winding. The secondary winding is

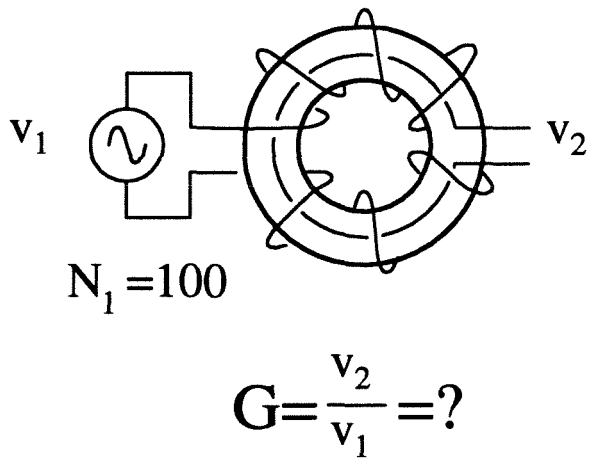

Figure A.1: The transformer structure under investigation. The one-turn secondary winding runs along the center of the toroid.

left open-circuited and the induced secondary voltage v_2 is measured. We can define the *primary voltage gain* as the ratio v_2/v_1.

The question we are interested in is

What is the "primary voltage gain" $G = \frac{v_2}{v_1}\Big|_{i_2=0}$?

A.2 Different Points of View Lead to Different Answers

It is possible to approach the problem from various points of view and obtain completely different answers. This situation is pictorially represented in Fig. A.2.

- An electrical engineering point of view could be to consider the structure a 100:1 transformer as in Fig. A.2a and say that "primary voltage gain" should be

$$G = \frac{1}{100}$$

- A physics approach would be to point out that flux generated by the primary winding flows along the toroid, and it is parallel to the secondary winding as in Fig. A.2b. As a result, there is no flux linking the secondary winding and the answer is

$$G = 0$$

- An antenna engineering point of view would be to consider the primary winding as an antenna. The 100-turn primary forms an equivalent one-turn winding parallel to the secondary winding and well-coupled to it, as shown in Fig. A.2c. Therefore, in some sense this is a one-to-one transformer and the answer is

$$G = 1$$

As you can see, different approaches lead to completely different answers.

NOTE: The three answers are called "electrical engineering," "physics" and "antenna engineering" approach just to show the different points of view and *not* to pass judgments on specialists of these disciplines. For example, the "electrical engineering" answer appears rather unsophisticated and clearly incorrect, since it completely disregards the physical structure of the problem under investigation. A good electrical engineer would definitely come up with a better answer than this. The author is himself an electrical engineer and obviously he is not trying to make bad publicity for his own specialty.

At this point it is appropriate to critically examine the three answers listed above.

The electrical engineering approach does not appear correct, because it does not take into account leakages and assumes perfect coupling between the two windings, which is quite far from the actual situation, as pointed out by the physics approach. This answer would be approximately correct if the geometry were different and the secondary winding were wound in the same way as the primary winding around the toroidal core. Such a configuration is indeed used in the realization of practical transformers, where maximum coupling is most desirable.

It is interesting to notice that the electrical engineering approach is the only one that gives an answer dependent on number of turns. The other two answers do not change if the number of turns changes. Since a dependence of "primary voltage gain" on number of turns is expected in a coupled-inductor structure, the other two answers appear suspect.

The physics approach appears an idealization of the real situation, and the "antenna engineering" observation that the 100-turn primary forms one equivalent turn coupled

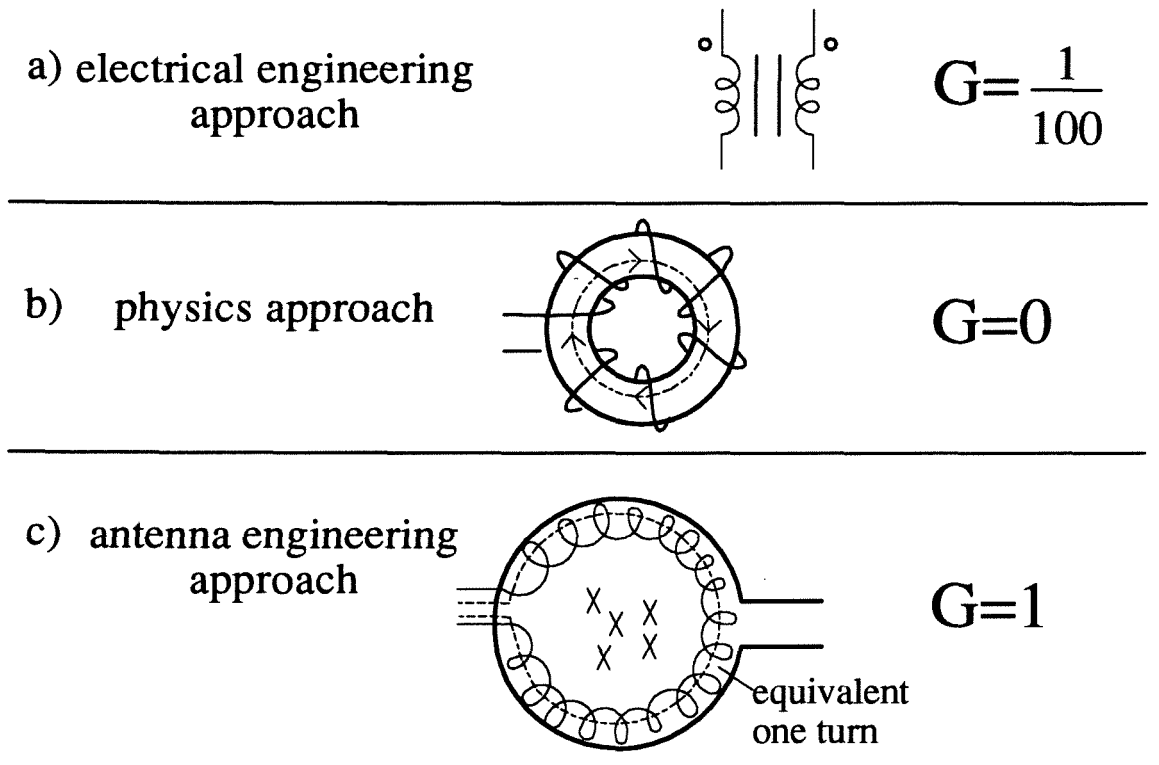

Figure A.2: Different approaches to this problem lead to different answers. The electrical engineering approach (a) considers the structure as a transformer, the physics approach (b) looks at flux geometry and the antenna engineering approach (c) looks at the structure as an antenna system.

with the secondary appears valid.

The antenna engineering answer suffers from the same problem of the electrical engineering answer: leakage is not taken into account.

In conclusion, all three answers appear unsatisfactory. In the next section an alternative answer is provided.

A.3 Analysis of Orthogonal Winding Structure

The way to analyze this structure is to construct a transformer model. It is clear that this system can be described by a transformer model. It is less clear what the turns ratio is, what the magnetizing and leakage inductances are. To clarify this, the transformer model is constructed piece by piece. The analysis is made in the general case of N_1 primary turns and N_2 secondary turns.

Turns ratio: the antenna engineering approach correctly pointed out that the N_1 primary turns form an equivalent one turn around the toroid that couples with the secondary as shown in Fig. A.1. In the general case of N_2 secondary turns, transformer turns ratio is $1{:}N_2$ as shown in Fig. A.2.

Magnetizing inductance: coupled flux ϕ_m is shown in Fig. A.3a. It is the flux that flows through the hole in the center of the core. Magnetizing inductance is the inductance of the equivalent one-turn primary winding.

Primary leakage inductance: primary leakage flux ϕ_{l1} is shown in Fig. A.3b. It is the flux that flows along the toroid. Notice that the usual analysis of a toroidal solenoid (see for example [11] pp. 408-409) considers only this flux component and neglects the flux component of Fig. A.3a. This is usually a good approximation, but in our case we are particularly interested in the coupled flux.

Secondary leakage inductance: to complete the model a secondary leakage inductance L_{l2} can be added as shown in Fig. A.3c. Notice, however, that this inductance has no effect on the value of G as long as there is no secondary current.

It is instructive to look at the current components that generate fluxes ϕ_m and ϕ_{l1}. If the individual turns are neglected and the current flowing on the toroid surface is considered, the toroid can be visualized as having a uniform sheet of current flowing on its surface. This sheet current has two orthogonal components: a primary leakage current $N_1 i_1$ and a magnetizing current i_1 as shown in Fig. A.4.

A.4 Estimation of Voltage Gain

From Fig. A.3c voltage gain is given by

$$G = \underbrace{\frac{L_m}{L_m + L_{l1}}}_{\text{"leakage loss"}} \cdot \underbrace{\frac{N_2}{1}}_{\substack{\text{turns} \\ \text{ratio}}} \tag{A.1}$$

where the first factor represents the effect of leakage, and the second term represents the turns ratio scaling.

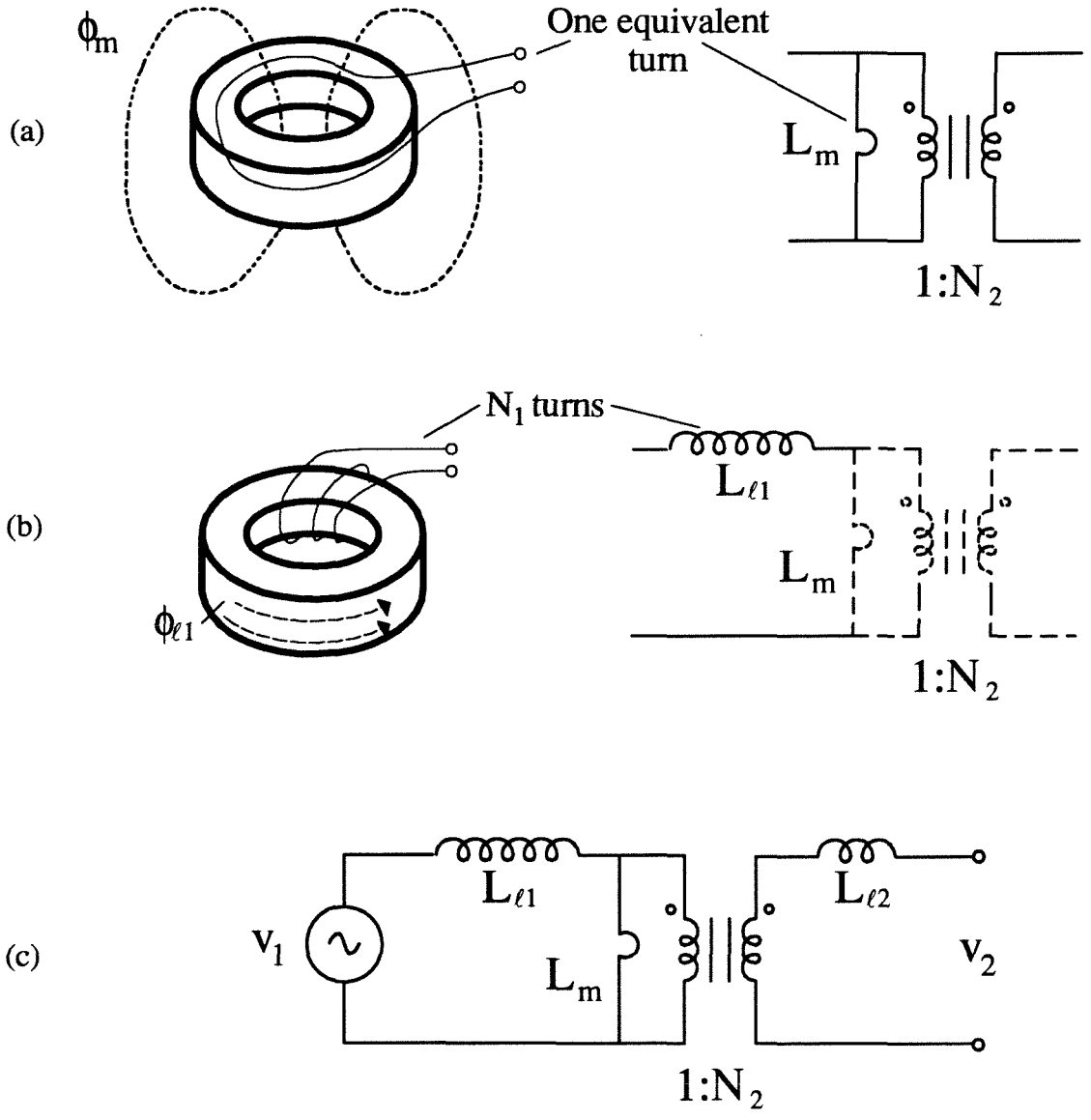

Figure A.3: Coupled flux ϕ_m (a) and primary leakage flux ϕ_{l1} (b). Complete transformer model (c).

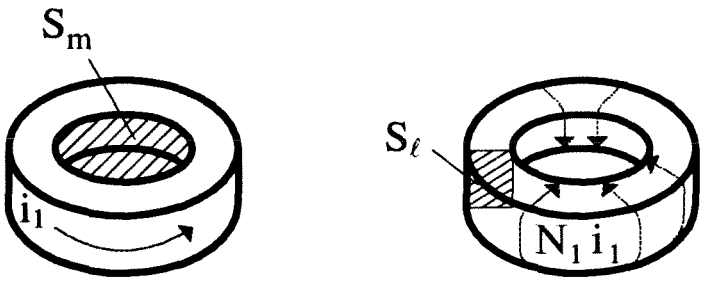

magnetizing current (a) leakage current (b)

Figure A.4: The two components of primary current.

Equation (A.1) is the correct answer with no approximation. In the following, some approximations are introduced to clarify the dependence of gain G on physical characteristics of the structure. The approximations are valid only if some additional assumptions on the system are made.

Inductances are proportional to the square of the number of turns, to permeability of the flux path and to the "cross-section" S of the flux path (shown in Fig. A.4). If we call μ_m the permeability of the mutual flux path and μ_l the permeability of the leakage flux path, then

$$L_m \propto \mu_m S_m$$

$$L_{l1} \propto N_1^2 \mu_l S_l$$

Using these expressions, equation (A.1) can be approximated as

$$G = \frac{L_m}{L_m + L_{l1}} \cdot N_2 \approx \frac{\mu_m S_m}{\mu_m S_m + N_1^2 \mu_l S_l} \cdot N_2 \qquad \text{(A.2)}$$

From this equation we can see that if $S_m \to 0$, then G approximates turns ratio N_2 (perfect coupling). This is reasonable because if cross-section S_l goes to zero, then the 100 turns "disappear" (see Fig. A.4) and the primary winding becomes a single turn well-coupled with the secondary.

If cross-sections S_m and S_l are comparable, it will be $L_{l1} \gg L_m$ and equation (A.2)

can be approximated as

$$G \approx \frac{L_m}{L_{l1}} \tag{A.3}$$

$$\approx \frac{N_2}{N_1^2} \cdot \frac{S_m}{S_l} \cdot \frac{\mu_m}{\mu_l} \tag{A.4}$$

This equation tells us that G is the product of three factors: a factor dependent on number of turns, a factor dependent on cross-sections and a factor dependent on permeabilities.

In the case of Fig. A.1, there is no high-permeability material and expression (A.4) simplifies to

$$G \approx \frac{N_2}{N_1^2} \cdot \frac{S_m}{S_l} \tag{A.5}$$

Since cross-sections are comparable, a further simplification leads to

$$G \approx \frac{N_2}{N_1^2} \tag{A.6}$$

For the structure of Fig. A.1, this approximate expression gives $G = 1/10\,000$.

A.5 Experimental Measurements

A prototype of the structure of Fig. A.1 is built using a standard Scotch tape roll as shown in the photo of Fig. A.5. It turns out that the groove present in Scotch tape rolls seems to be built expressly to host the one-turn secondary, as shown in Fig. A.5a. Primary turns can then be wound around the Scotch tape roll as shown in Fig. A.5b. The prototype has 136 primary turns.

Measured amplitude and phase plot of G as a function of frequency obtained using the HP3577A network analyzer are shown in Fig. A.6. There is a fair amount of noise at low frequency and peaking at high frequency due to self-resonance, but there is a mid-frequency range with constant gain

$$G = -72\ dB = \frac{1}{3\,980} \tag{A.7}$$

The figure is included mainly to show that the non-zero secondary voltage is real and not an artifact of measurement noise.

The measurement value is in reasonably good agreement with the value $G \approx 1/136^2 = 1/18\,496$ predicted by the simplified expression (A.6).

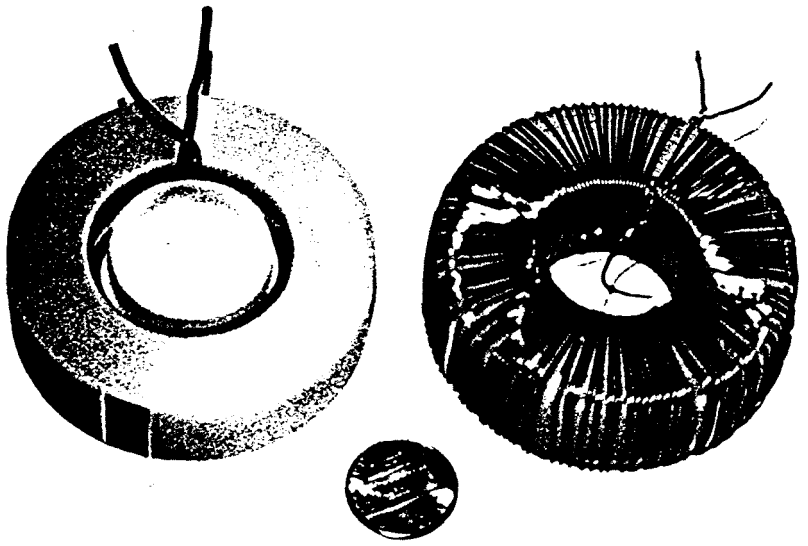

Figure A.5: Prototype and detail of secondary winding.

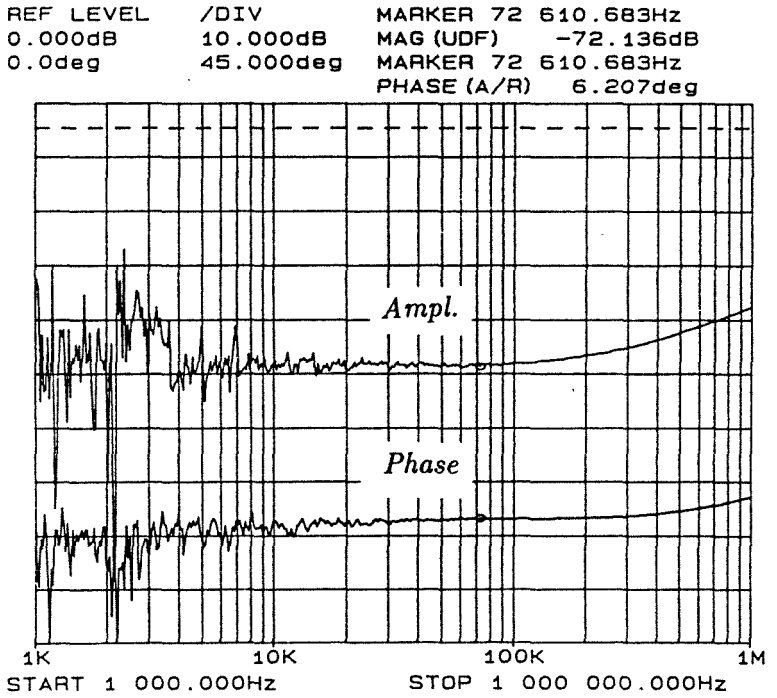

Figure A.6: Network analyzer plot of G as a function of frequency.

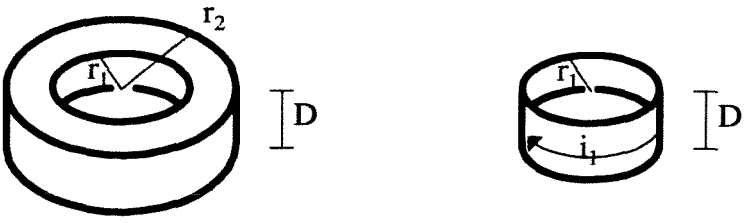

(a) (b)

Figure A.7: Definition of structure dimensions (a) and short solenoid approximation for L_m.

A.6 Model Refinement

A better prediction can be obtained directly from expression (A.1) without introducing the approximations of (A.6).

In order to use that formula, we need to evaluate inductances L_m and L_{l1}. Leakage inductance L_{l1} is the inductance of a toroidal solenoid and a formula is given, for example, in [11] (pp. 408–409)

$$L_{l1} = \frac{\mu_0 D \cdot N_1^2}{2\pi} \ln(\frac{r_2}{r_1}) = 66\,\mu H \tag{A.8}$$

where r_1, r_2, D are shown in Fig. A.7a. The measured total primary inductance (approximately equal to L_{l1}) is $L_1 = 71\ \mu H$, in good agreement with the value calculated here.

Magnetizing inductance is harder to evaluate accurately given the strange geometry. However, we can consider the sheet current of Fig. A.4 and make the approximation that all this current flows on the inner surface of the toroid, as shown in Fig. A.7b. This approximation appears reasonable since the mutual flux we are trying to model mostly flows through the hole in the middle of the toroid as in Fig. A.3b. An approximate formula for the inductance of the short solenoid of Fig. A.4b can be found in [10] pg. 192. Using this formula

$$L_m = \frac{\mu_0 \pi r_1^2}{D + 0.9 r_1} = 19.7\,nH \tag{A.9}$$

Using these inductance values equation (A.1) gives

$$G = \frac{1}{3\,350}$$

with a 19% error with respect to the measured value.

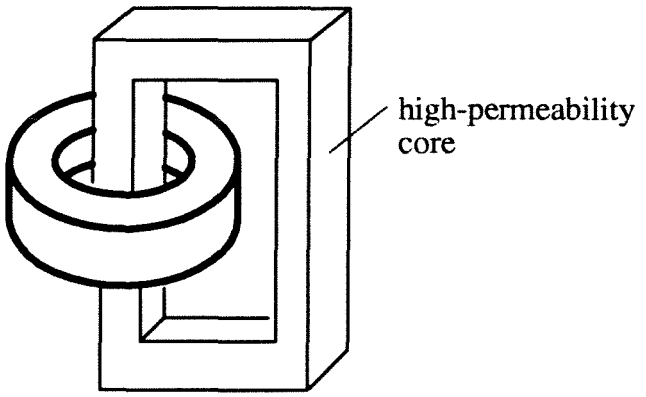

Figure A.8: A high-permeability core is used to increase the permeability of the coupled flux path.

A.7 Two More Orthogonal Winding Structures: Changing the Permeability of Flux Paths

Equation (A.4) shows that measured voltage gain is proportional to the ratio of permeabilities of the two flux paths. To verify this, two more experiments are performed varying the permeability of the flux paths.

In the first experiment the same Scotch-tape structure is used, but the permeability of the coupled flux path is increased by putting a UU60 core with a 0.5 mm gap through the center hole of the toroid as shown in Fig. A.8. Leakage inductance is unchanged and magnetizing inductance is

$$L_m = \frac{1^2}{\mathcal{R}_x} = \frac{\mu_0 S}{x} = 565\ nH$$

where $\mathcal{R}_x$ is gap reluctance, S is core cross-section and x is gap thickness. Calculated voltage gain from equation (A.1) is 1/118 and measured voltage gain is 1/130 with a 9% error.

In the second experiment the permeability of the leakage flux path was increased by using a high-permeability toroid. Two toroids manufactured by Magnetics, order number 2 55585-D4, with relative permeability $\mu_{rel} = 125$, were stacked with the one-turn secondary sandwiched between them. Physical dimensions are different from the

air-core toroid used so far and primary number of turns is $N_1 = 103$. A smaller voltage gain is expected because permeability of the leakage flux path is increased.

The measured voltage gain is

$$G = -91.6\ dB = \frac{1}{38\,326}$$

and the value predicted using (A.1), (A.8) and (A.9) is

$$G = \frac{1}{53\,548}$$

In this case the error is 40%.

A.8 Secondary Voltage Gain

Until this point, only the "primary voltage gain" has been studied. The primary is driven and the induced secondary voltage is measured. It seems natural to look at the voltage gain in the opposite direction, i.e., the "secondary voltage gain"

$$G' = \left.\frac{v_1}{v_2}\right|_{i_1=0}$$

where the secondary is driven and the induced primary voltage is measured.

An attempt was made at measuring this voltage gain for the magnetic structure of Fig. A.5. The result is shown in Fig. A.9. Amplitude and phase of gain G' vary with frequency, and there is no frequency range over which the gain is constant like in the "primary voltage gain" plot of Fig. A.6.

This behavior cannot be explained by the model of Fig. A.3c. Qualitatively, the plot can be explained by introducing secondary parasitic resistance R_2 and parasitic capacitance C in the transformer model, as shown in Fig. A.10.

Like in every transformer, resistance R_2 dominates at low frequency and is responsible for the $+20$ *dB/dec* slope of the magnitude plot of G'. At high frequency, the parasitic capacitance C self resonates with the secondary inductance, and that explains the peaking appearing in the magnitude plot of G'.

The difference is that in a conventional transformer between the low-frequency and the high-frequency regions, there is a mid-frequency region with constant gain. That is

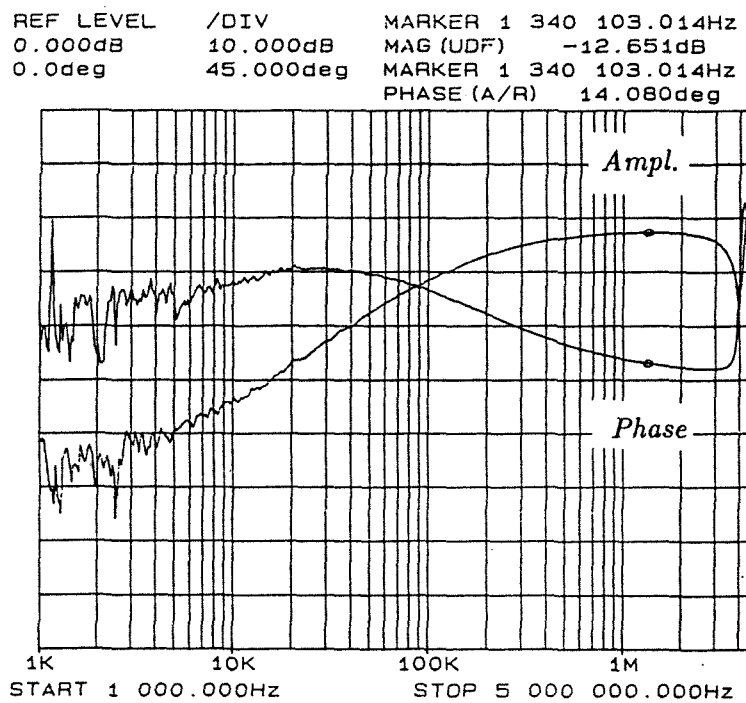

Figure A.9: Network analyzer plot of G' as a function of frequency.

the range of frequencies where both R_2 and C can be neglected. The operating frequency of a conventional transformer is in this mid-frequency range.

Notice that this constant gain region is practically non-existent in the plot of Fig. A.9. To understand why this happens, we need to remember that the secondary is a one-turn loop in air. It is hard to say whether it is an inductor, a resistor or a capacitor. Our lumped model fails, and probably a distributed model would be an appropriate way to describe this system.

From this discussion it seems that our model would work if we could boost the secondary inductance above the level of parasitics. This can be done by increasing the permeability of the mutual flux path as shown in Fig. A.8.

Looking at the transformer model of Fig. A.3c, it is

$$G' = \left.\frac{v_1}{v_2}\right|_{i_1=0} = \frac{L_m}{L_m + L_{l2}}$$

Given the presence of the high-permeability core, we can safely assume that $L_m \gg L_{l2}$ and, therefore, it should be $G' \approx 1$, i.e., perfect coupling. A value of $G' = 0.9$ was

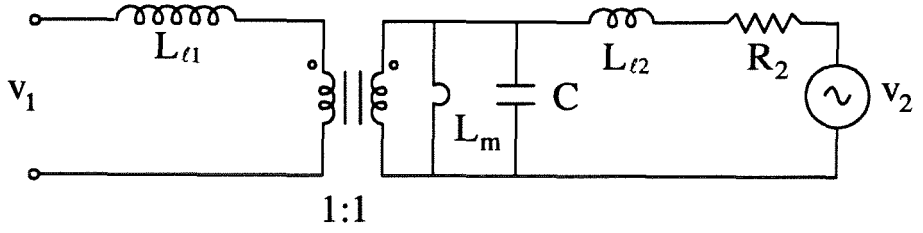

Figure A.10: Transformer model with parasitics.

measured.

A.9 Conclusions

The orthogonal winding structure puts to a test one's physical understanding of coupled magnetic structures. The dependence on physical paramenters such as numbers of turns, permeability and structure geometry is verified by experiments that very closely match theoretical predictions.

Appendix B

Derivation of Important Result for Coupled-Inductor Design

In this appendix a formula useful for coupled-inductor design is derived.

Suppose we have a generic coupled-inductor structure with N_1 primary turns and N_2 secondary turns. It is a reciprocal two-port and it can be represented in complete generality by the black-box reluctance model of Fig. B.1. Coupling coefficient k_1 and inductance L_1 are defined as usual. For convenience, definitions are repeated here. Coupling coefficient is defined as

$$k_1 \triangleq \frac{\phi_2}{\phi_1}\bigg|_{I_2=0} \tag{B.1}$$

and inductance L_1 is

$$L_1 \triangleq \frac{N_1^2}{\mathcal{R}_{eq}} \tag{B.2}$$

where $\mathcal{R}_{eq}$ is the equivalent reluctance seen from the primary with secondary *mmf* source $N_2 I_2$ shorted (which means open-circuited secondary). This is illustrated in Fig. B.2.

We want to prove the following result:

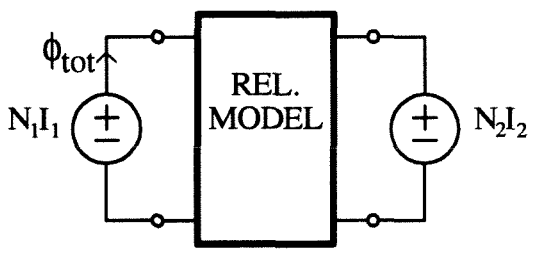

Figure B.1: Generic coupled-inductor structure represented by its reluctance model.

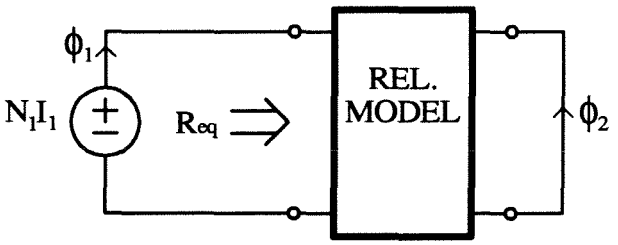

Figure B.2: Definition of reluctance $\mathcal{R}_{eq}$.

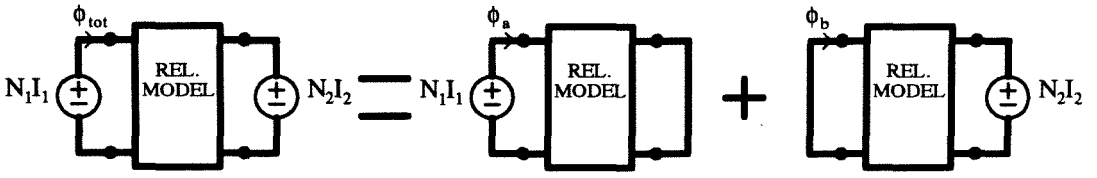

Figure B.3: Superposition is used to calculate ϕ_{tot}.

Statement *The coupled-inductor structure shown in Fig. B.1 is considered. The assumption is made that reciprocity holds. Primary flux ϕ_{tot} is given by the expression*

$$\phi_{tot} = \frac{L_1}{N_1}\left(I_1 + k_1\frac{N_2}{N_1}I_2\right) \tag{B.3}$$

Flux ϕ_{tot} can be calculated by applying superposition as shown in Fig. B.3 and it is given by

$$\phi_{tot} = \phi_a + \phi_b \tag{B.4}$$

Flux ϕ_a can immediately be calculated from Fig. B.2 as

$$\phi_a = \frac{N_1 I_1}{\mathcal{R}_{eq}} \tag{B.5}$$

In order to calculate flux ϕ_b, the reciprocity theorem can be used. This theorem can be stated in the following form:

Reciprocity Theorem *Given a linear time-invariant two-port consisting of resistors only, consider the following two situations shown in Fig. B.4. Connect a voltage source*

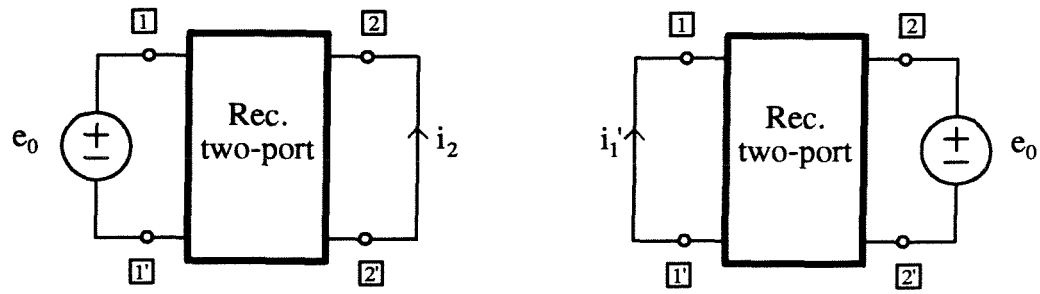

Figure B.4: Reciprocity theorem says that $i_2 = i_1'$.

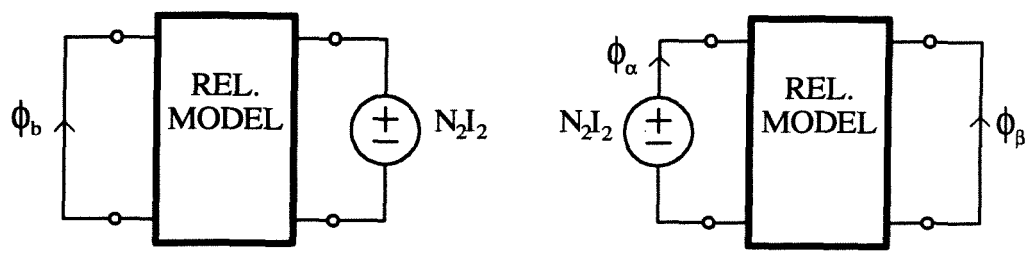

Figure B.5: Reciprocity applied to the reluctance model says that flux ϕ_b *is equal to flux* ϕ_β.

e_0 *at terminals* 1-1', *short terminals* 2-2' *and measure current* i_2. *Next connect the same voltage source to terminals* 2-2', *short terminals* 1-1' *and measure current* i_1'. *The reciprocity theorem states that it is*

$$i_1' = i_2$$

Applying this theorem to the two-port of Fig. B.3c, we can interchange the short and the *mmf* source as shown in Fig. B.5 and it is

$$\phi_\beta = \phi_b$$

From the definitions of k_1 given by equation (B.1), it follows that

$$\phi_\beta = k_1 \phi_\alpha$$

and ϕ_α is

$$\phi_\alpha = \frac{N_2 I_2}{\mathcal{R}_{eq}}$$

Therefore, it is

$$\phi_b = \phi_\beta = k_1 \phi_\alpha = k_1 \frac{N_2 I_2}{\mathcal{R}_{eq}} \tag{B.6}$$

Putting together equations (B.4), (B.5) and (B.6)

$$\phi_{tot} = \frac{1}{\mathcal{R}_{eq}} (N_1 I_1 + k_1 N_2 I_2) \tag{B.7}$$

Substituting (B.2) into (B.7) we get the final result

$$\phi_{tot} = \frac{L_1}{N_1} \left(I_1 + k_1 \frac{N_2}{N_1} I_2 \right)$$

Importance of derived result Equation (B.3) has been demonstrated in a very general case. The only assumption made is that the coupled-inductor structure is reciprocal. The importance of this result is that it simplifies significantly if zero ripple condition on the secondary side is satisfied. The zero current ripple condition for the secondary is

$$k_1 = \frac{N_1}{N_2} \tag{B.8}$$

In that case equation (B.3) becomes

$$\phi_{tot} = \frac{L_1}{N_1} (I_1 + I_2) \tag{B.9}$$

This equation has been derived in [3] for a specific reluctance model (Π-type reluctance model), and it was the key to obtaining closed-form design equations for coupled inductors, because primary number of turns N_1 can be immediately calculated from (B.9) by setting ϕ_{tot} equal to the desired maximum flux in the core.

We would also like to stress the similarity of equation (B.9) with the design equation for a conventional inductor. In the design of an inductor L with peak current I, the following equation is used

$$\phi_{SAT} = \frac{LI}{N}$$

Notice that this equation has the same form of equation (B.9). Therefore, for a given value of inductance L_1 and maximum allowable flux ϕ_{SAT}, the primary number of turns N_1 of a coupled-inductor structure is identical to the number of turns N that would be used in the design of a conventional inductor that carries a DC current $I = I_1 + I_2$.

Appendix C

Estimation of Leakage Permeance from Core Geometry

In chapter 10 it was stated that under certain simplifying assumptions the leakage permeance of a UI core is approximately equal to the permeance between two right prisms of infinite permeability immersed in a material of permeability μ_0. The goal of this appendix is to derive the approximate formulas for this permeance as a function of prism geometry given in equations (10.1). The method used is described in [6] and [7].

Fig. C.1a shows the two right prisms. An *mmf* source ψ applies a magnetic potential difference between the two prisms and causes a flux ϕ to flow between them. The permeance $\mathcal{P}$ is given by

$$\mathcal{P} = \frac{\phi}{\psi}$$

In a region with no currents, the magnetic field H is curl-free and there is an equivalence between magnetic field equations and electric field equation. The equivalent electric field problem is shown in Fig. C.1b. An *emf* source V applies an electric potential difference between the two prisms and causes a current I to flow between them. Conductance $\mathcal{G}$ is given by

$$\mathcal{G} = \frac{I}{V}$$

Since the equations describing the magnetic and electric field problem are identical (except for scaling factors μ_0 and σ_0, see section 2.2), permeance and conductance are related as follows:

$$\frac{\mathcal{P}}{\mu_0} = \frac{\mathcal{G}}{\sigma_0}$$

The problem of Fig. C.1a-b is still a complex three-dimensional field problem. However, the flux path geometry in different regions can be approximated by simple geomet-

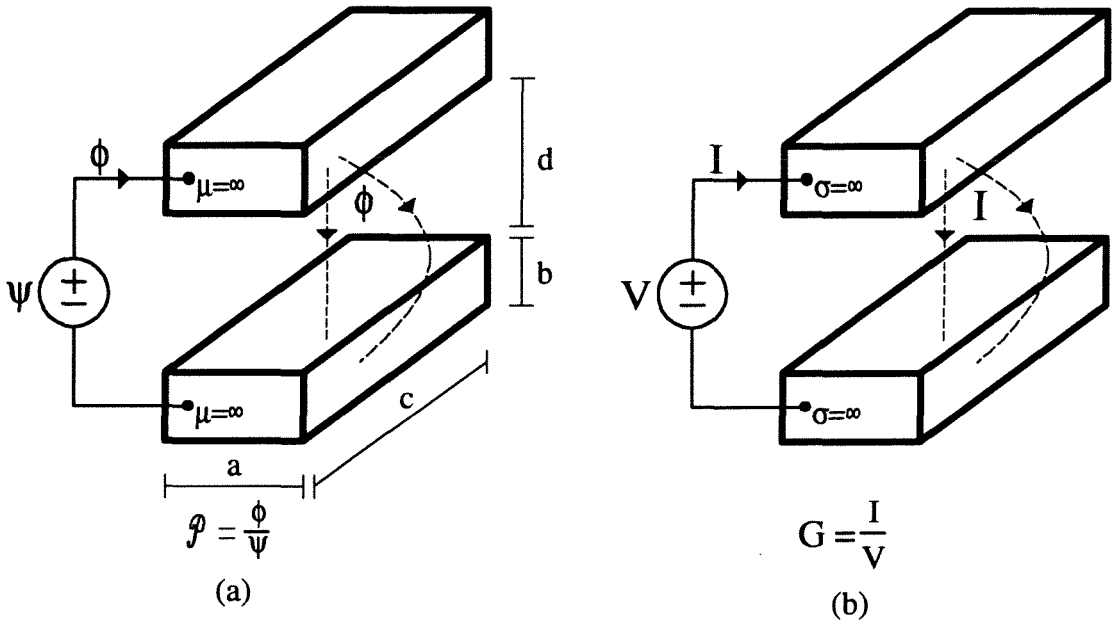

Figure C.1: The magnetic field problem of determining permeance $\mathcal{P}$ between two prisms of infinite permeability is equivalent to the problem of determining conductance $\mathcal{G}$ between two prisms of infinite conductivity.

ric shapes, and approximate formulas for the permeance of these regions can be found. Adding together the contributions of all the flux paths gives the total permeance.

The first step is to divide the space around the prisms in different regions. This is shown in Fig. C.2. Region 1 is the space between the two prisms. Regions 2 and 3 represent space around the prisms.

The second step is to consider each region separately and estimate probable flux paths. This estimate is somewhat arbitrary, but the following guidelines should be kept in mind:

- Flux lines at the prism surface are always perpendicular to the surface due to the infinite permeability of the prisms.

- Flux paths in air between any two surfaces always arrange themselves in such a manner that the maximum possible flux will be produced for a given magnetomotive force.

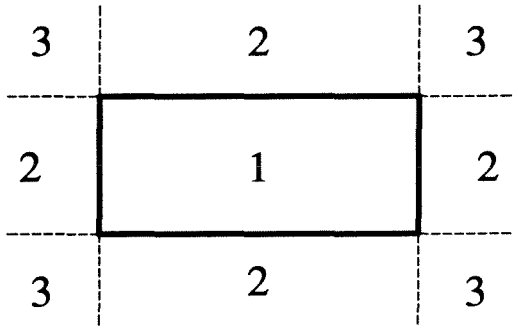

Figure C.2: Top view of the prisms. The free space surrounding the prisms is divided into three regions.

C.1 Permeance of Region 1

Region 1 is a rectangular parallelepiped region. Fig. C.3 illustrates this region. The flux field is assumed to be parallel and uniform, and it flows from the top to the bottom surfaces S. The flux is therefore equal to flux density B multiplied by top surface area.

$$\phi = B \cdot a \cdot c$$

The magnetic potential is given by magnetic field intensity multiplied by the distance between the two prisms.

$$\psi = H \cdot d$$

The permeance of the region is then

$$\mathcal{P} = \frac{\phi}{\psi} = \frac{B \cdot a \cdot c}{H \cdot d} = \mu_0 \frac{a \cdot c}{d} \tag{C.1}$$

Notice that this expression is identical to the expression for the permeance of an air gap of width d between two surfaces of area $a \cdot c$.

C.2 Permeance of Region 2

Region 2 can be divided in two subregions as shown in Fig. C.4. The two subregions have the shape of a semicircular cylinder and a half annulus. Notice that Region 2 extends to infinity, but the two subregions are finite. The approximation is made that flux further outside the two subregions is small and can be neglected.

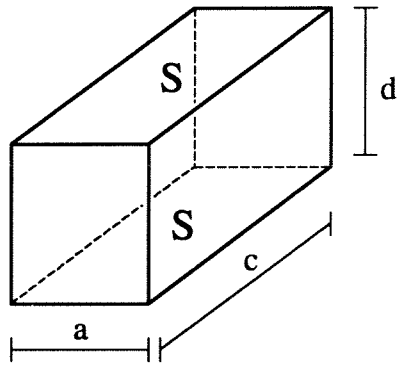

Figure C.3: Region 1. Flux lines are vertical and go from top to bottom surfaces.

Half annulus Flux paths in the half annulus are approximately semicircles as shown in Fig. C.5. The length of a flux path is πr and the magnetic field is

$$B = \frac{\mu_0 \psi}{\pi r}$$

Flux is

$$\phi = length \cdot \int B \, dr = length \cdot \frac{\mu_0 \psi}{\pi} \int_{d/2}^{b+d/2} \frac{dr}{r} = \frac{\mu_0 \psi}{\pi} \ln\left(1 + \frac{2b}{d}\right) \cdot length$$

Permeance is

$$\mathcal{P} = \frac{\phi}{\psi} = \frac{\mu_0}{\pi} \ln\left(1 + \frac{2b}{d}\right) \cdot length$$

Semicircular cylinder The permeance of this subregion is not as easy to calculate as the other regions considered this far. An approximate method can be devised by looking at equation (C.1). That equation shows that the permeance is given by

$$\mathcal{P} = \mu_0 \frac{[\ cross\text{-}section\ of\ flux\ path\ ]}{[\ length\ of\ flux\ path\ ]} \tag{C.2}$$

In the case of a non-uniform path, a mean length and a mean cross-section can be considered.

$$\mathcal{P} = \mu_0 \frac{[\ mean\ cross\text{-}section\ of\ flux\ path\ ]}{[\ mean\ length\ of\ flux\ path\ ]} \tag{C.3}$$

(C.4)

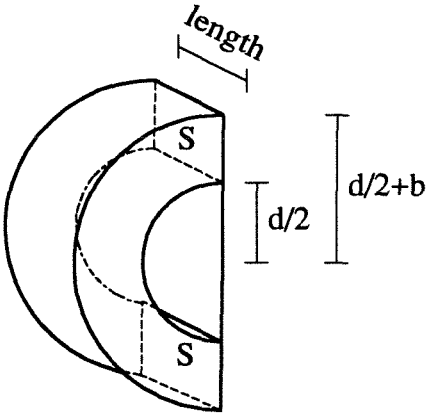

Figure C.4: Region 2 can be divided into two subregions: a semicircular cylinder and a half annulus.

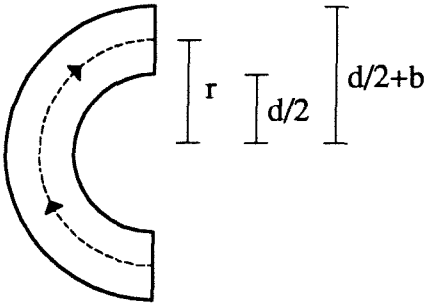

Figure C.5: Side view of the half annulus subregion with dashed flux lines.

In some cases mean cross-section will be evaluated by dividing the volume of the region by the mean length of flux path. Equation (C.2) becomes

$$\mathcal{P} = \mu_0 \frac{[\ \textit{volume of region}\ ]}{[\ \textit{mean length of flux path}\ ]^2} \tag{C.5}$$

In the case of a semicircular cylinder, the mean length of the flux path can be considered to be equal to the length of a line drawn midway between the diameter and the semicircumference of Fig. C.6, and by graphical measurement it can be found to be approximately $1.22d$. The volume of the region is $\pi d^2/8 \cdot \textit{length}$, so the permeance is

$$\mathcal{P} = \mu_0 \frac{\pi d^2/8}{(1.22d)^2} \cdot \textit{length} = 0.26\mu_0 \cdot \textit{length}$$

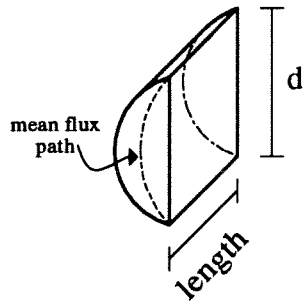

Figure C.6: Semicircular cylinder subregion with dashed lines representing the mean flux path.

C.3 Permeance of Region 3

This region can be divided in two subregions, a spherical quadrant and a quadrant of spherical shell.

Spherical quadrant The spherical quadrant is shown in Fig. C.7. The mean length of the flux path now is different from that shown in Fig. C.6, and it can be approximated to be $1.3d$. From (C.5) the permeance is

$$\mathcal{P} = \mu_0 \frac{\frac{1}{3}\pi \left(\frac{d}{2}\right)^3}{(1.3d)^2} = 0.077\mu_0 d$$

Quadrant of spherical shell The quadrant of a spherical shell is shown in Fig. C.8. The mean length is

$$\frac{\pi}{2}(b+d)$$

The maximum cross-section of the flux path will be

$$\frac{\pi \left(b+\frac{d}{2}\right)^2}{4} - \frac{\pi}{4}\left(\frac{d}{2}\right)^2 = \frac{\pi}{4}b(b+d)$$

The average area of the path may be considered to be $\pi/8\ b(b+d)$. From (C.3) permeance is

$$\mathcal{P} = \mu_0 \frac{\frac{\pi}{4}b(b+d)}{\frac{\pi}{2}(b+d)} = \mu_0 \frac{b}{4}$$

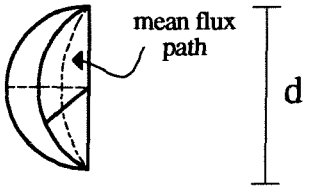

Figure C.7: Spherical quadrant subregion with dashed line representing mean flux path.

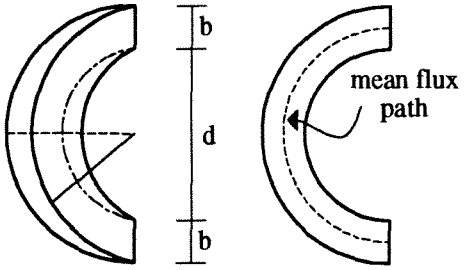

Figure C.8: Quadrant of spherical shell subregion and side view representing mean flux path.

Appendix D

Sufficient Stability Condition for Modified One Cycle Control

The following fact is proved in this appendix.

Fact: Any Ćuk converter is stabilized by control law

$$v_{C1}d - V_{ref} + K_1(i_1 - I_{1ref}) = 0$$

for K_1 sufficiently big.

Proof The Routh-Hurwitz criterion is applied to the linearized equations (16.2) of the controlled converter, which are repeated here for convenience

$$\begin{vmatrix} \frac{d\hat{i}_1}{dt} \\ \frac{d\hat{v}_{C1}}{dt} \\ \frac{d\hat{i}_2}{dt} \\ \frac{d\hat{v}_0}{dt} \end{vmatrix} = \underbrace{\begin{vmatrix} -\frac{K_1}{L_1} & -\frac{1}{L_1} & 0 & 0 \\ \frac{1}{C_1}\left(1 - D + \frac{D}{1-D}\frac{K_1}{R}\right) & \frac{1}{C_1}\frac{D^2}{(1-D)R} & -\frac{D}{C_1} & 0 \\ -\frac{K_1}{L_2} & 0 & 0 & -\frac{1}{L_2} \\ 0 & 0 & \frac{1}{C} & -\frac{1}{RC} \end{vmatrix}}_{A} \begin{vmatrix} \hat{i}_1 \\ \hat{v}_{C1} \\ \hat{i}_2 \\ \hat{v}_0 \end{vmatrix}$$

The A matrix has the form

$$A = \begin{vmatrix} a_{11} & a_{12} & 0 & 0 \\ a_{21} & a_{22} & a_{23} & 0 \\ a_{31} & 0 & 0 & a_{34} \\ 0 & 0 & a_{43} & a_{44} \end{vmatrix}$$

The eigenvalues are the roots of

$$\lambda^4 + \alpha\lambda^3 + \beta\lambda^2 + \gamma\lambda + \delta = 0 \tag{D.1}$$

where

$$\alpha = -a_{11} - a_{22} - a_{44} \tag{D.2}$$

$$\beta = -a_{34}a_{43} + (a_{11} + a_{22})\, a_{44} + a_{11}a_{22} - a_{12}a_{21} \tag{D.3}$$

$$\gamma = a_{34}a_{43}\,(a_{11} + a_{22}) - a_{11}a_{22}a_{44} + a_{12}a_{21}a_{44} - a_{12}a_{23}a_{31} \tag{D.4}$$

$$\delta = -a_{11}a_{22}a_{34}a_{43} + a_{12}a_{21}a_{34}a_{43} + a_{12}a_{23}a_{31}a_{44} \tag{D.5}$$

From Routh-Hurwitz criterion the stability conditions for (D.1) are

$$\alpha > 0 \tag{D.6}$$

$$\alpha\beta - \gamma > 0 \tag{D.7}$$

$$\alpha\beta\gamma - \gamma^2 - \alpha^2\delta > 0 \tag{D.8}$$

Now let us calculate approximate values of α, β, γ, δ under the condition that K_1 be big.

$$\alpha \approx \frac{K_1}{L_1} \tag{D.9}$$

$$\beta \approx K_1 \left(\frac{1}{L_1 C R} + \frac{D}{L_1 C_1 R}\right) \tag{D.10}$$

$$\gamma \approx K_1 \left(\frac{1}{L_1 L_2 C} + \frac{D}{L_1 C_1 C R^2} + \frac{D}{L_1 L_2 C_1}\right) \tag{D.11}$$

$$\delta \approx \frac{K_1}{L_1 L_2 C_1 C} \frac{2D}{R} \tag{D.12}$$

These equations are obtained neglecting all terms that do not contain K_1.

Condition (D.6) is trivially true. Condition (D.7) is true because $\alpha\beta$, which is a positive quantity, is proportional to K_1^2 and γ is proportional to K_1 only. Therefore, for K_1 big, the term proportional to K_1^2 dominates.

Condition (D.8) can be simplified because $\alpha\beta\gamma$ and $\alpha^2\delta$ are proportional to K_1^3 and γ^2 is proportional to K_1^2 only.

$$0 < \alpha\beta\gamma - \gamma^2 - \alpha^2\delta \approx \alpha\beta\gamma - \alpha^2\delta = \alpha(\beta\gamma - \alpha\delta) \tag{D.13}$$

This condition can be simplified to

$$\beta\gamma - \alpha\delta > 0 \tag{D.14}$$

Substituting (D.9), (D.10), (D.11), (D.12) into (D.14)

$$K_1^2\left[\left(\frac{1}{L_1CR}+\frac{D}{L_1C_1R}\right)\left(\frac{1}{L_1L_2C}+\frac{D}{L_1C_1CR^2}+\frac{D}{L_1L_2C_1}\right)-\frac{1}{L_1^2L_2C_1C}\,\frac{2D}{R}\right]>0 \tag{D.15}$$

This expression simplifies to

$$K_1^2\left[\frac{1}{L_1^2L_2C^2R}+\frac{D}{L_1^2C_1C^2R}+\frac{D^2}{L_1^2C_1^2CR^3}+\frac{D^2}{L_1^2L_2C_1^2R}\right]>0 \tag{D.16}$$

which is always positive. This proves the statement.

Appendix E

Sufficient Stability Condition for Modified One-Cycle Control Applied to Third Order Ćuk Converter

We want to find sufficient stability conditions for a third-order Ćuk converter (no output capacitor C) controlled by the law

$$v_{C1}d - V_{ref} + K_1(i_1 - I_{1ref}) = 0$$

The perturbed equations of the controlled system are

$$\begin{vmatrix} \frac{d\hat{i}_1}{dt} \\ \frac{d\hat{v}_{C1}}{dt} \\ \frac{d\hat{i}_2}{dt} \end{vmatrix} = \underbrace{\begin{vmatrix} -\frac{K_1}{L_1} & -\frac{1}{L_1} & 0 \\ \frac{1}{C_1}\left(1 - D + \frac{D}{1-D}\frac{K_1}{R}\right) & \frac{1}{C_1}\frac{D^2}{(1-D)R} & -\frac{D}{C_1} \\ -\frac{K_1}{L_2} & 0 & -\frac{R}{L_2} \end{vmatrix}}_{A} \begin{vmatrix} \hat{i}_1 \\ \hat{v}_{C1} \\ \hat{i}_2 \end{vmatrix}$$

The A matrix has the form

$$A = \begin{vmatrix} a_{11} & a_{12} & 0 \\ a_{21} & a_{22} & a_{23} \\ a_{31} & 0 & a_{33} \end{vmatrix}$$

The eigenvalues are the roots of

$$\lambda^3 + \alpha\lambda^2 + \beta\lambda + \gamma = 0 \tag{E.1}$$

where

$$\alpha = -a_{11} - a_{22} - a_{33} \tag{E.2}$$

$$\beta = a_{11}a_{22} - a_{12}a_{21} + a_{33}(a_{11} + a_{22}) \tag{E.3}$$

$$\gamma = a_{23}a_{12}a_{31} - a_{33}(a_{11}a_{22} - a_{12}a_{21}) \tag{E.4}$$

From Routh-Hurwitz criterion the stability conditions for (E.1) are

$$\alpha > 0 \tag{E.5}$$

$$\alpha\beta - \gamma > 0 \tag{E.6}$$

Condition (E.5) is

$$a_{11} + a_{22} + a_{33} < 0 \tag{E.7}$$

After simplification, condition (E.6) is

$$(a_{11} + a_{22})[-a_{11}a_{33} - a_{22}a_{33} - a_{33}^2 - a_{11}a_{22} + a_{12}a_{21}] - a_{23}a_{12}a_{31} > 0 \tag{E.8}$$

Notice that $-a_{23}a_{12}a_{31} > 0$. Therefore, a sufficient stability condition is

$$(a_{11} + a_{22})[-a_{11}a_{33} - a_{22}a_{33} - a_{33}^2 - a_{11}a_{22} + a_{12}a_{21}] > 0 \tag{E.9}$$

If it is

$$a_{11} + a_{22} < 0 \tag{E.10}$$

then (E.9) becomes

$$a_{11}a_{33} + a_{22}a_{33} + a_{33}^2 + a_{11}a_{22} - a_{12}a_{21} > 0 \tag{E.11}$$

which can be written as

$$[\underbrace{a_{33}}_{<0}(\underbrace{a_{11} + a_{22}}_{<0})] + \underbrace{a_{33}^2}_{>0} + (a_{11}a_{22} - a_{12}a_{21}) > 0$$

Therefore, a sufficient condition is

$$a_{11}a_{22} - a_{12}a_{21} > 0 \tag{E.12}$$

Substituting expressions for the a_{ij}, coefficients the first term of (E.12) becomes

$$a_{11}a_{22} - a_{12}a_{21} = \frac{1}{L_1C_1}\left[-\frac{K_1}{R}\frac{D^2}{1-D} + 1 - D + \frac{K_1}{R}\frac{D}{1-D}\right]$$

which simplifies to

$$a_{11}a_{22} - a_{12}a_{21} = \frac{1}{L_1C_1}\left[\frac{K_1}{R}D + 1 - D\right]$$

This last quantity is always positive and so (E.12) is always true. Therefore, (E.7) and (E.10) are sufficient stability conditions. Notice that (E.10) implies (E.7) since $a_{33} < 0$. Therefore, (E.10) by itself is a sufficient stability condition. It can be written as

$$K_1 > \frac{L_1}{C_1}\frac{D^2}{1-D}\frac{1}{R}$$

This is the desired sufficient stability condition.

References

[1] S. Ćuk, "Dc-Dc Switching Converter with Zero Input and Output Current Ripple and Integrated Magnetics," U.S. Patent No. 4,257,087, March 17, 1981.

[2] E. Santi and S. Ćuk, "Accurate Leakage Models of Gapped Magnetic Circuits," IEEE Applied Power Electronics Conference, 1993 Record, pp. 596–603 (IEEE Publication 0-7803-0982-0/93).

[3] S. Ćuk and Z. Zhang, "Coupled-Inductor Analysis and Design," IEEE Power Electronics Specialists Conference, 1986 Record, pp. 655–665 (IEEE Publication 0275-9306/86/0000-0655).

[4] S. Ćuk, "A New Zero-Ripple Switching Dc-to-Dc Converter and Integrated Magnetics," IEEE Power Electronics Specialists Conference, 1980 Record, pp. 12–32 (IEEE Publication 80CH1529-7).

[5] Z. Zhang, "Coupled-Inductor Magnetics in Power Electronics," Ph.D. thesis, California Institute of Technology, 1986.

[6] H. C. Roters, *Electromagnetic Devices*, John Wiley & Sons, 1941, pp. 116–150.

[7] W. B. Boast, *Vector Fields; a Vector Foundation of Electric and Magnetic Fields*, Harper & Row, pp. 524–537.

[8] M. Brković and S. Ćuk, "Input Current Shaper Using Ćuk Converter," Proc. Intelec '92, pp. 532–539 (IEEE Publication 0-78030779-8/92).

[9] A. A. Dauhajre, "Modelling and Estimation of Leakage Phenomena in Magnetic Circuits," Ph.D. thesis, California Institute of Technology, 1986.

[10] S. Ramo, J. R. Whinnery and T. Van Duzer, *Fields and Waves in Communication Electronics,* John Wiley & Sons, 1965.

[11] M. Zahn, *Electromagnetic Field Theory: a Problem Solving Approach,* R. Krieger Publishing Co., 1979.

[12] J. K. Watson, *Applications of Magnetism,* John Wiley & Sons, 1980.

[13] S. El-Hamamsy and E. I. Chang, "Magnetics Modeling for Computer-Aided Design of Power Electronics Circuits," IEEE Power Electronics Specialists Conference, 1989 Record, pp. 635–645 (IEEE Publication CH2721-9/89/0000-0635).

[14] A. Cocconi and S. Ćuk, "Design of a 2kW, 100kHz Switching Regulator for Space Shuttle," Proc. Fifth International PCI'82 Conference, pp. 72–85.

[15] S. Ćuk and D. Maksimovic, "Integrated-Magnetics, Quasi-Resonant Ćuk Converter," Proc. of the Third High Frequency Power Conversion Conference, 1988.

[16] S. Ćuk, L. Stevanovic and E. Santi, "Integrated Magnetics Design with Flat, Low Profile Cores," High Frequency Power Conversion Conference, 1990.

[17] E. Santi and S. Ćuk, "Modelling of One-Cycle Controlled Switching Converters," Proc. Intelec '92, pp. 131–138 (IEEE Publication 0-7803-0779-8/92).

[18] K. Ma Smedley and S. Ćuk, "One-Cycle Control of Switching Converters," IEEE Power Electronics Specialists Conference, 1991 Record, pp. 888–896 (IEEE Publication 0-7803-0090-4/91/0700-0888).

[19] K. Ma Smedley, "Control Art of Switching Converters," Ph.D. thesis, California Institute of Technology, 1991, pp. 105–195.

[20] R. D. Middlebrook and Slobodan Ćuk, "A General Unified Approach to Modelling Switching Converter Power Stages," IEEE Power Electronics Specialists Conference, 1976 Record, pp. 18–34 (IEEE Publication 76CH1084-3 AES); also International J. of Electronics, vol. 42, no. 6, pp. 521–550, June 1977.

[21] G. W. Wester and R. D. Middlebrook, "Low Frequency Characterization of Switched DC-DC Converters," IEEE Power Electronics Specialists Conference, 1972 Record, pp. 9–20.